Stony Brook University

"Thermal Spray Processing of Ceramic Oxide Coatings: An Integrated Approach"

A Dissertation Presented

by

Jose Rafael Colmenares Angulo

To

The Graduate School
In Partial Fulfillment of the
Requirements
For the Degree of

Doctor of Philosophy

in

Materials Science and Engineering

Stony Brook University

December 2010

Stony Brook University
The Graduate School

Jose Rafael Colmenares Angulo

We, the dissertation committee for the above candidate for the
Doctor of Philosophy degree, hereby recommend
Acceptance of this dissertation

Prof. Sanjay Sampath – Dissertation Advisor
Professor, Materials Science and Engineering Department

Prof. Herbert Herman
Distinguished Professor Emeritus
Materials Science and Engineering Department

Prof. David Welch
Adjunct Professor, Materials Science and Engineering Department

Dr. Seiji Kuroda
Managing Director, Hybrid Materials Center
National Institute of Materials Science of Japan

This Dissertation is accepted by the Graduate School

Lawrence Martin
Dean of the Graduate School

Abstract of Dissertation

Thermal Spray Processing of Ceramic Oxide Coatings: An Integrated Approach

by

Jose Rafael Colmenares Angulo

Doctor of Philosophy

in

Materials Science and Engineering

Stony Brook University

2010

Thermal spray represents a complex processing technology given the stochastic nature of rapid splat melting, impact and solidification. The present work represents a series of studies with the aim of improving the understanding of process-property relationships on ceramic oxides integrating recent work from the Center of Thermal Spray Research regarding particle and non-particle state issues intrinsic to thermal spray processing with material specific applications

Issues regarding reliability of two-wavelength pyrometry and time-of-flight methods for thermal spray sensing are analyzed using a simultaneous comparative approach for HVOF and APS techniques with 5 different commercial sensors. Injection visualization techniques are included to analyze particle-plume interactions and the limitations of commercial ensemble measurements for first order process maps and repeatability measurements are discussed.

Titanium dioxide coating formation mechanisms are examined with a wide range of process techniques and conditions applying an extended process map approach. Routes for coating formation from a microstructural, crystalline and stoichiometric perspective are correlated to issues of photocatalytical, electrical and thermal transport. The role of deposition rate as a key parameter in defining coating stress state is discussed, while particle state variations are found to be more significant in controlling phase content and transport properties. A key finding of this work is that the stochiometric distortions on TiO_2 induced by thermal spray processing have a higher effect on coating photocatalytical activity than the fraction of metastable anatase phase.

Novel techniques and applications are analyzed from a process oriented perspective including characterization of individual splats and ensemble coating properties. Precursor/Solution thermal spray coating and splat morphological characteristics are attributed mainly to atomization issues. 1^{st} and 2^{nd} order process maps of alumina-chromia coatings for fluorescent mapping of accelerated proton beams where constructed with the aim of increasing the fraction of the stable alpha phase and optimizing coating luminescence for the intended application

Dedication

To My Parents, Brother, Sister and Nephew

Table of contents

Chapter 1. Introduction and Statement of the Problem 1

1.1 Motivation: Process Maps for Thermal Spray, Integration of Materials Science with Process Science 1

1.2 Thermal Spray Processing of Materials 2

1.3 Defective Nature of Thermal Spray Coatings: Microstructural Effects 3

1.4 Processing Effects in Thermal Spray 4

1.5 Chemical and Crystallographic Issues on Ceramic Oxides of Interest 5

1.5.1 Titanium Dioxide 5

1.5.2 Aluminum Oxide + Chromium Oxide 8

1.5.3 Ytrtria Stabilized Zirconia 10

1.6 Statement of the problem 11

1.6.1 Expanded Processing Capabilities 12

1.6.2 Particle and Non-Particle State Parameters 12

1.6.3 Integration of Novel Techniques and Characterization Methods for Ceramic Oxides 12

Chapter 2. Experimental Techniques 13

2.1.1 Plasma Spray 13

2.1.2 Flame Spray 14

2.1.3 HVOF Spray 14

2.1.4 Thermal Spraying with Liquid Feedstock 15

2.2 Particle State Monitoring Techniques 17

2.2.1 Advanced Particle State Indicators based on commercial sensors particle state measurements 19

2.3 Residual Stress and Curvature Monitoring Techniques 21

2.3.1 Ex-situ highly controlled variant 24

2.4 Coating Characterization 25

2.4.1 XRD 25

2.4.2 Microscopy 25

2.4.3 RAMAN Spectroscopy 26

2.4.4 Photocatalytical Activity 27

2.4.5 Fluoresence 27

2.4.6 Thermal Conductivity 28

2.4.7 Electrical resistivity / Impedance Measurements 29

Chapter 3.Particle State monitoring by two-wavelength pyrometry, time of flight method and particle injection visualization, assessment of different diagnostic approaches 30

3.1 Process Map Development for Plasma Spraying 30

3.2 Responses of Different Sensors to Parameter Modification 33

3.3 Sensor Comparison for HVOF coatings 36

3.4 Validation of Individual Particle measurements by the assistance of computer simulations 37

3.5 Possible sources of temperature measurement inconsistencies 38

3.6 Process Map with a tighter window of parameter variation 39

3.7 Repeated Measurements with constant particle state 40

3.8 Response of different sensors to algorithms for constant particle state achievement 42

3.9 Particle injection visualization salient observations 43

3.9.1 Injection optimization-APS 43

3.9.2 Quality problems with particle feeding 45

3.9.3 HVOF shock-wave diamonds 46

3.9.4 Flame Spray particle interaction observation 47

3.10 Image Particle Velocimetry and the effect of capturing parameters on the sensor reading 49

3.11 Conclusion 51

Chapter 4. Process Mapping of Titanium Dioxide Coatings, implications of processing techniques on rapid solidification phenomena 52

4.1 Deliberate Manipulation of Particle State by change of process parameters and hardware 52

4.2 Effect of particle state on coating microstructure and porosity 55

4.3 Effect of particle state on coating phase evolution 57

4.4 Raman Microspectroscopy of Individual Splats, understanding paths for phase evolution mechanisms 60

4.5 Exploratory Studies of Liquid feedstock thermal spray of TiO_2 66

4.5.1 Experimental objectives and technical information 67
4.5.2 Experimental Design 68
4.5.3 Results 69
4.5.4 Precursor spray 77
4.5.5 Conclusions on liquid feedstock thermal spray 79
4.6 Interplay between phase stability issues and processing induced stoichiometric losses in titanium dioxide 81
4.6.1 Particle State Modification and its effect on transport properties through torch hardware modification 81
4.6.2 Analysis: Driving force for the creation of conductive pathways in TiO_2 thermal spray coatings 89
4.7 Photocatalytic Activity of TiO_2 coatings and the effect of post-spraying re-oxidation 90
4.7.1 Coating Processing Procedure 91
4.7.2 Spectroscopic Analysis 92
4.7.3 Photocatalytical Coating Response 94
4.8 Conclusions 96
Chapter 5. On the role of particle state and non-particle state parameters and their influence in evolving stress of TiO_2 coatings 97
5.1 Non-particle state parameters and their effect on coating evolving stress, modulus and microstructure 101
5.1.1 Parameter Selection 102
5.1.2 Influence of Deposition Rate on Evolving Stress, Microstructure and Modulus 103
5.1.3 Properties not affected by deposition rate 108
5.1.4 Deposition Rate Effects on electrical properties of TiO_2 coatings 109
5.1.5 Deposition Rate on compliant substrates 112
Chapter 6. Luminescence of Alumina-Chromia Flame Sprayed Coatings optimized by 115
6.1 Experimental Approach 115
6.2 Experimental Results and Discussion 118
6.2.1 Effects of Chromia Content and Spray Distance on Fluorescence 118
6.2.2 Effects of process parameter, substrate temperature and feedstock characteristics on coating fluorescence 119

6.2.3 Process Map and the relation with coating buildup and solidification mechanisms 120
6.3 Coating Characterization 122
6.4 Splat Analysis 123
6.5 Conclusions 124
Chapter 7. Conclusions 125
7.1 Future Work 126
Bibliography 128

List of Figures

Figure 1: Simplified principle of the thermal spray technique 2
Figure 2: Schematic of thermal spray processing stages. Red Arrows: First Order Process Map Stages Blue Arrows: Second Order Process Map Stages (taken from reference[5]) 3
Figure 3:Example of columnar grain grow in Yttria Stabilized Zirconia splats 4
Figure 4: The polymorphs of Titanium Dioxide, Crystallographic data taken from [37] 7
Figure 5: Single Crystals of Titanium Dioxide show different colors as a function of annealing temperature and surrounding atmosphere. Adapted from [43] 8
Figure 6: Common Polymorphs of Aluminum Oxide in Thermal Spray (a) stable α or corundum and (b) metastable γ. Adaped from [49] 9
Figure 7: The polymorphs of Zirconium Dioxide, Taken from [41] 10
Figure 8: Methodological approach and contribution to knowledge in thermal spray science of this dissertation 11
Figure 9: Plasma Spray Torch Principle of operation, adapted from[69] 13
Figure 10: TheroDyn Flame Spray Torch used for the work described in this manuscript 14
Figure 11: Schematic layout of a Diamond Jet HVOF torch, adapted from[71] 15
Figure 12: Schematic of differences between conventional and liquid thermal spray techniques 16
Figure 13: schematic of two-wavelength pyrometry and time of flight method, adapted from[82] 17
Figure 14.A: Typical set up of Hi-Watch Particle Injection System Figure 14.B: Example of visualization of particle injection into plasma stream 18
Figure 15:Principle of stress/curvature generation during spraying, adapted from [90] 22
Figure 16-a: the in-situ curvature sensor Figure 16-b: typical in mediate output of the sensor (before processing) 22
Figure 17-a: Ex-situ curvature sensor Figure 17-b: comparison between controlled oven and uncontrolled torch curvature-temperature measurements 24
Figure 18: key outputs of the ex-situ curvature-temperature and stress/strain analysis 25
Figure 19: (a) Original SEM cross section microstructure (b) processed binary image (taken from[97]) 26
Figure 20: principle of Photocatalytical Pollutant Decomposition (taken from[102]) 27
Figure 21: (a) layout of the National Spallation Source at Oakridge National Lab. (b) Liquid Mercury Target Container to be bombarded with H+ Ions for the emission of Neutrons (adapted from[104]) 28
Figure 22: Schematic of Xenon Flash Laser Thermal Conductivity Instrument (Taken from [107]) 29
Figure 23: parameters chosen for the sensor comparison experimental design 32
Figure 24: response of different sensors to variations in total flow of gasses. Arrows indicate increase of total gas flow keeping the rest of the parameters constant 33
Figure 25: response of different sensors to variations in torch current. Arrows indicate increase of torch current increases keeping the rest of the parameters constant 35
Figure 26: Response of different sensors to variations in Hydrogen Fraction in the stream.. 35
Figure 27: measured sensors responses to variations in HVOF combustion chemistry 36
Figure 28: results of the LAVA simulated process map. , arrows indicate increases on selected parameters 38

Figure 29: results of the reduced window of variation process map measured with accuraspray, with parameter effect indications 40
Figure 30: Mean and Range of Different Sensors for Repeated Particle State Measurements 41
Figure 31: State of Similar Temperature & Velocity algorithm experiment as measured with different sensors 43
Figure 32: Particle Temeprature Optimization and its relation with Spraywatch injection images 45
Figure 33: Visualization of Injection quality 46
Figure 34: HVOF flame stream at the exit of the spray nozzle for different combustion chemistries 47
Figure 35: first order process map of Al_2O_3 + 1%Cr_2O_3 for a Therodyn flame spray torch 48
Figure 36: observation of flame spray interaction with particles for different flame chemistries 49
Figure 37: Spraywatch measurement with different approaches to camera settings 50
Figure 38: Threshold of Plasma Emission Distortions on Ensemble Two-Wavelength Pyrometry 51
Figure 39: Expanded first order process map agglomerated and sintered TiO_2 54
Figure 40: Particle Temperature Distributions for Extended 1st order process map 55
Figure 41: Selected Microstructures of TiO_2 extended process map (low magnification) 56
Figure 42: Selected Microstructures of TiO_2 extended process map (high magnification) 56
Figure 43: second order process map of coating porosity 57
Figure 44: Second Order Process Map of TiO_2 Phase Content 58
Figure 45: Possible mechanisms for TiO2 splat phase evolution, all scenarios will be present in all conditions, but presented here indicate prevalence phase in particles for each condition 59
Figure 46: Optical micrographs of (A) Large, isolated, flattened splat (B) elongated and overlapped splat (C) small (probably, also imperfectly flattened) splat (D) and micro-Raman spectra of these splats indicating Anatase and Rutile Peaks 62
Figure 47: Optical micrographs of two small splats for the fine anatase APS sample and their micro-Raman spectra 63
Figure 48: Raman Spectra for fully molten splats 64
Figure 49: partially molten splats in HVOF sample for Microraman Spectroscopy 65
Figure 50: size dependency of particle melting state 65
Figure 51: reconciliation of proposed solidification pathways with individual splat raman spectroscopic analysis 66
Figure 52a: Injector holder for both APS and HVOF torches, Figure 52b: diagram of liquid injection setup into an atmospheric plasma spray torch 68
Figure 53: Process Conditions Cubic Experimental Design 68
Figure 54: x-ray diffraction patterns of plasma sprayed coatings 69
Figure 55: Anatase content and substrate temperature for plasma sprayed coatings 70
Figure 56: Suspension plasma spray splats 71
Figure 57: microstructures of suspension plasma spray coatings 71
Figure 58: "splat" one pass samples for precursor plasma spray 72
Figure 59: cross section of precursor plasma sprayed coating samples 73
Figure 60: Effect of raster speed on diffraction pattern for low current precursor sprayed coatings 74
Figure 61: x-ray diffraction patterns of high velocity oxy-fuel coatings 74

Figure 62: Figure 5: Anatase content and substrate temperature for HVOF coatings……75
Figure 63: Suspension HVOF splats....76
Figure 64: Cross section of suspension HVOF samples....77
Figure 65: Precursor HVOF splats....78
Figure 66: Cross section of precursor HVOF samples....78
Figure 67: Conventional Photographs of Liquid Interaction with Flame....79
Figure 68: reconciliation of liquid feedstock thermal spray solidification pathways with previously proposed mechanisms for conventional thermal spray....80
Figure 69: SEM micrographs of 4 different TiO_2 coatings sprayed with different hardware in low and high magnifications....82
Figure 70: processing particle state for transport property studies....83
Figure 71: Through Thickness Thermal Conductivity for TiO2 samples with different heat cycling times....83
Figure 72: Anisotropy in electrical resistivity of different TiO2 samples....84
Figure 73: Through Thickness Impedance Measurements for TiO_2 samples with and without heat treatment....85
Figure 74: Expanded second order process map of in-plane electrical resistivity for TiO_2....86
Figure 75: Relationship between electrical and thermal transport properties in the through-thickness direction....87
Figure 76: In- Plane Resistivity as a function of melting index and kinetic energy for the expanded 2^{nd} order process map samples....88
Figure 77: Through thickness electrical resistivity as a function of melting index and kinetic energy....88
Figure 78: Relationship between electrical and mechanical properties....89
Figure 79: Stability of titanium-oxygen system as a function of surrounding temperature and oxygen atmosphere....89
Figure 80: Different Mechanisms that define electrical transport properties for TiO_2 coatings in the process space....90
Figure 81: Example of coating color change after heat treatment for the HVOF samples....92
Figure 82: XRD patterns of the coatings: (A) HVOF - as sprayed; (B) APS - as sprayed; (C) HVOF - heat treated; (D) APS – heat treated;....93
Figure 83: Raman spectrographs of the 4 coatings: (A) HVOF - as sprayed; (B) APS - as sprayed; (C) HVOF - heat treated; (D) APS – heat treated;....94
Figure 84: Photocatalytic activity in degradation of methylene blue for various coatings. Insert shows Uv-vis spectra of APS-heat treated sample as a function of time....94
Figure 85: Rate constants of photocatalytic degradation for various coatings....95
Figure 86: Curvature Evolution of Plasma Sprayed TiO_2 coatings....97
Figure 87: detail of the first steps of the curvature evolution of the different TiO_2 APS conditions....98
Figure 88: Second Order Process Map of plasma sprayed TiO_2 evolving stress....99
Figure 89: Second order process map of coating elastic modulus calculated by ICP....100
Figure 90: Elastic modulus as a function of melting index and kinetic energy....100
Figure 91: experimental design for deposition rate process map....102
Figure 92: Particle State for deposition rate experiments (a) in context of extended process map (b) temperature histograms....103
Figure 93: response of deposition rate experiments....104
Figure 94: microstructures of deposition rate experiments coatings....104

Figure 95:curvature evolution for selected deposition rate experiments 105
Figure 96: ECP modulus of deposition rate experiments..... 106
Figure 97: Effect of thickness/pass on coating elastic modulus 107
Figure 98: Schematic of effect of thickness per pass changes; the thick line represents inter-pass interfaces, while thinner line represents inter-splat interfaces 107
Figure 99: Effect of Deposition rate on (a) Anatase content and (b) Thermal Conductivity..... 108
Figure 100: in plane sheet resistivity as a function of deposition rate 109
Figure 101: through thickness resistivity as a function of deposition rate..... 110
Figure 102: variations in through-thickness impedance after removing sample from de-humidifying oven 111
Figure 103: Photographs of samples sprayed with different deposition rates..... 112
Figure 104: Curvature evoltion of different deposition rate experiments for (a) ICP measurements and (b) ECP cooling 112
Figure 105: Computed Evolving Stress and Modulus Values for Compliant Substrate Experiments 113
Figure 106: microstructures of different deposition rate experiment..... 113
Figure 107: Reconciliation of evolving stress studies and deposition rate effects with other properties studied in this work and their influence by particle state. 114
Figure 108: Previous findings of the feasibility, optimum Cr_2O_3 concentration and best method for target coating. 115
Figure 109: experimental design for 3rd stage of the experimental series..... 117
Figure 110: fluoresecence measurement of the exploratory studes normalized to a standard ruby sample..... 118
Figure 111: Intensity of coatings as a function of substrate temperature 119
Figure 112: effect of feedstock characteristics on coating fluorescence..... 119
Figure 113: A) first order process maps of flame sprayed alumina-chromia coatings B) Second order map of normalized fluorescence C) Second order process map of thickness per robot pass during spraying..... 120
Figure 114: comparison of curvature evolution of the flame sprayed coatings studied in int this work with example APS and HVOF sprayed alumina coatings 121
Figure 115: Curvature/Evolving Stress for different process map samples..... 122
Figure 116: raman microspectroscopy mapping of flame sprayed alumina-chromia sample..... 122
Figure 117: normalized intensity of selected process map samples as a function of their alpha phase content..... 123
Figure 118: Raman analysis of individual splats of the Alumina-Chromia System 123

List of Tables

Table 1: Principle of Geometrical Description of Particle Stream by Different Commercial Sensors 20
Table 2: Parameters used for simultaneous measurement Process Map.....32
Table 3: Gas flow variations for HVOF sensor experiments.....36
Table 4: Torch parameters used in LAVA simulation.....37
Table 5: Parameters used for the reduced parameter window process map 39
Table 6: Torch Parameters for Extended TiO_2 First Order Process Map 53
Table 7: Description of Splat Samples for Microraman Spectroscopy.....61
Table 8: Process Parameters applied in this study *spray distances or raster speeds were modified in selected points of the experimental cube for coatings or splats only 69
Table 10: Process Parameters and Particle State for photocatalytic coating processing 92
Table 9: Parameters for Deposition Rate on Electrical Properties Study 111
Table 11: experimental variables modified in the exploratory stage of the fluorescence study.....116
Table 12: experimental design for the second stage of the study 116
Table 13: experimental design for feedstock influence of coating fluorescence, all coatings sprayed with 30 slpm of O_2 and 23 slpm of acetylene at 6" stand off distance 116
Table 14: parameters kept constant during the alumina-chromia fluorescence study.....118

Acknowledgements

I would like to thank my Advisor, Prof. Sampath for the countless hours of meetings and discussions and experimental and professional issues, for the opportunities that being a part of the CTSR team has given me and for the long work hours of meetings writing and traveling he spends so his students and postdocs have a better professional future. I would also like to thank the members of the committee, Prof. Welch, Prof. Herman and Kuroda-sensei for their advice and suggestions.

Prof. Orlov and his team were very helpful in the photocatalysis part of this work, Professors Andrew Gouldstone, Christopher Weyant and Richard Gambino provided time, advice and critics during my tenure as a graduate student. Glenn Bancke provided numerous tips on safety and equipment operation and technical advice on coating processing.

Three former graduate students, now doctors were especially helpful in mentoring my introduction to the world of thermal spray and ceramic oxides: Atin Sharma, Vasudevan Srinivasan and Alfredo Valarezo. Also Three postdoctoral fellows: Kentaro Shinoda, Yang Tan and Brian Choi where very helpful in making decisions regarding the course of this thesis

Other Stony Brook colleagues who have my appreciation include Gopal Diwedi (counless hours of ECP/ICP discussions), Christopher Young (Raman Microespectroscopy), Lorena Bejarano, Travis Wentz (sensor work), Dr. Qu (splats), Dr. Liang (electrical properties), Dr. Wu (splats), Ling Li (DTA/TGA), John Gutlemberg (HVOF), Eduardo Mari (HVOF), Vaishak Viswanathan (ECP), Junghan Kim (Dilatometry), Lysa Russo, Debby Michenzi, Lynn Allopenna, Eileen Zappia, Shen Zhao, Christopher Mork, Riston Rocchio-Heller, Antonio Torcia, Antonio Caccavale, Steve Bader, Mateo Mantovani, Radek Musalek, Nuria Cinca, Chris Jensen and Joseph Ortiz

Kuroda Sensei help was not limited to serving as a committee member; he was also a mentor during my 6 month stay in Japan working with his group in the National Institute of Materials Science. The NIMS team: Murakami-sensei, Komatu-san, Hiraoka-san, Watanabe-san, Kim-san, Kawakita-san, Yasui-san, Kaise-san, Yasuda-san, Yoshida-san, Take-san and Rosalie-san all were all helpful during my research and visit in Tsukuba. Funding for traveling and research was provided by NIMS international graduate school program.

Other international institutes and researchers were very helpful in this work: Professors Cannillo and Lushvarghi and their team in University of Modena & Reggio Emilia collaborated in the extended process maps of TiO_2 and Raman Microspectroscopy. Drs. Robert Vassen, Giorg Mauer and Ophelia Duenas-Jarligo added valuable comments to the sensors work. Forschungszentrum Jülich and the Deutscher Akademischer Austausch Dienst provided funds for traveling to perform research with Dr. Vassens Group.

Main source of funding for this work was provided by National Science Foundation through the GOALI-FRG program (award CMMI 0605704) and the Consortium of Thermal Spray Technology

Last but not least I would like to thank all my non materials scientist friends and family who provided support during my stay in Stony Brook and abroad, especially to my parents for all their advice.

Chapter 1. Introduction and Statement of the Problem

1.1 Motivation: Process Maps for Thermal Spray, Integration of Materials Science with Process Science

The field of modern material science and engineering, since its beginnings in steel metallurgy, has not been an isolated science, but a dynamic interdisciplinary field aimed to understand materials fundamental characteristics with the final goal of accelerating technological progress. The field of Thermal Spray Technology is no exception to this premise, slowly, since the first introduction of its fundamental principles [1] the field has progressed from being an art based on operator anecdotal experience, to highly sophisticated discipline to which scientist all over the planet strive to understand and fully control.

The present dissertation summarizes research work encompassing diverse areas of thermal spray research with the objective of furthering knowledge on areas related to control and applicability of ceramic oxide thermal spray coatings. This manuscript does not intend to be an isolated set of results and scientific premises, but intends to contribute in the basis of previous developments –with consequent open questions- in thermal spray science. Our work is grounded mainly in research performed by previous investigators at Stony Brook Center for Thermal Spray Research, but also tries to combine findings and theories from other leading laboratories in the world, many of them direct contributors to this work such as NIMS Japan, the University Modena & Reggio Emilia in Italy and Sulzer-Metco.

The reliability of particle state measurement sensors and the manipulation of particle state consume a significant part of this work. Material specific questions such as phase evolution during solidification of TiO_2 are addressed always sustained by a process map approach. Functional properties such as coating fluorescence, photocatalytical activity or coating transport properties are analyzed with a process oriented methodology that allows for clarification of explicit questions in thermally sprayed ceramic oxide materials systems. The experimental process manipulation is not limited to torch parameter variation as most literature on the field shows but also by the alteration of "non-particle state" parameters that have been recently shown to be key in coating formation mechanisms.

1.2 Thermal Spray Processing of Materials

Thermal Spray consists of a series of technologies which follow a major principle, increasing the heat content of a material in order to melt it, to then project it to a surface to create an even coating. This process is applicable for different purposes, such as wear, corrosion and/or high temperature protection[2]. There are different approaches to this principle, which are normally classified by the method of heat transfer to the material, such as Wire Arc, Flame Spray, High Velocity Oxygen fuel (HVOF) and Plasma Spray being the later two the main focus of this study. The material to be projected (i.e. feedstock) consists of wires or a powder with a controlled size distribution and more recently a liquid suspension or solution.

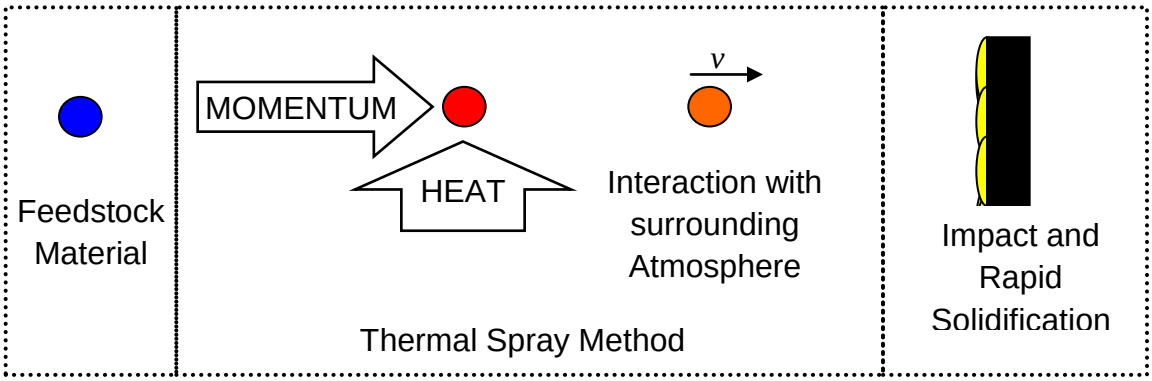

Figure 1: Simplified principle of the thermal spray technique

Physical properties of thermally sprayed materials usually differ from their bulk counterparts due to the high cooling rates of about 10^6 to 10^8 K/s[3] and the stochastic nature of coating formation which consists of the impact and accumulation of overlapping solidified particles called *splats*. Thermal spray is an exceptionally complex and dynamic process, were the long list of variables (carefully detailed in reference [4]) that define the coating formation mechanisms are interrelated in a way that is hard to experimentally isolate, a summary of the most important variables that define and depend of the coating formation process is shown in Figure 2

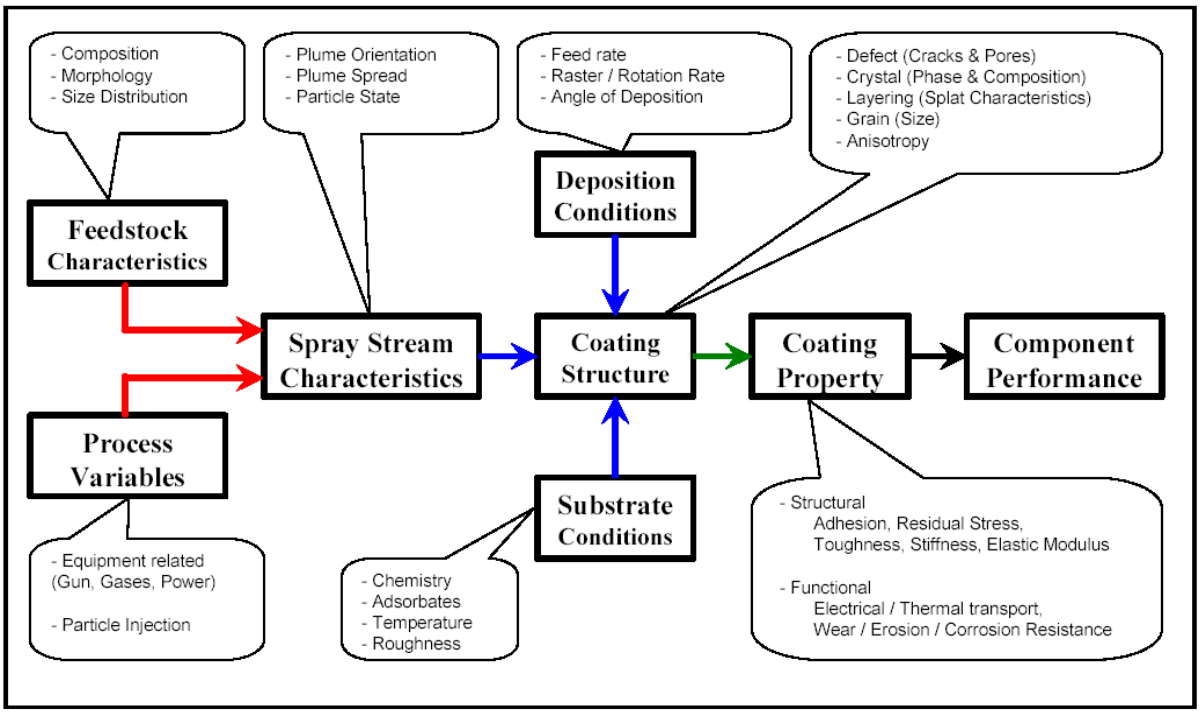

Figure 2: Schematic of thermal spray processing stages. Red Arrows: First Order Process Map Stages Blue Arrows: Second Order Process Map Stages (taken from reference[5])

1.3 Defective Nature of Thermal Spray Coatings: Microstructural Effects

It is a known premise that materials properties are governed by their defects, and thermal spray is a prime example of this principle. As particles are injected into the heat source, complex material-process interactions[6] controlled by convective heating and acceleration phenomena in combination with the size distribution of the particles results in different thermal histories for each of the millions of particles processed. At impact, this will translate into differences in splat temperature and kinetic energies with implications in molten liquid viscosity and wetting which will define the flattening of the splats and their solidification rates. The overlapping of morphologically distinctive splats will results a lamellar microstructure with a wide range of splat-splat true contact areas[7], voids and cracks[8] making the coatings highly anisotropic[9] in their mechanical and transport properties.

Rapid solidification usually results in submicron columnar grain sizes equiaxed towards the substrate[10] as observed Figure 3. Such crystallite sizes are dependent on particle state at impact[11] and feedstock[12] that will have a significant effect on coating mechanical properties[13]

The characterization of thermal spray coating intrinsic defects and properties has advanced in recent years from being based solely in microscopic techniques to advanced methods such as Small Angle Neutron Scattering[14], Acoustic Emission[15] and even instrumented indentation[16]

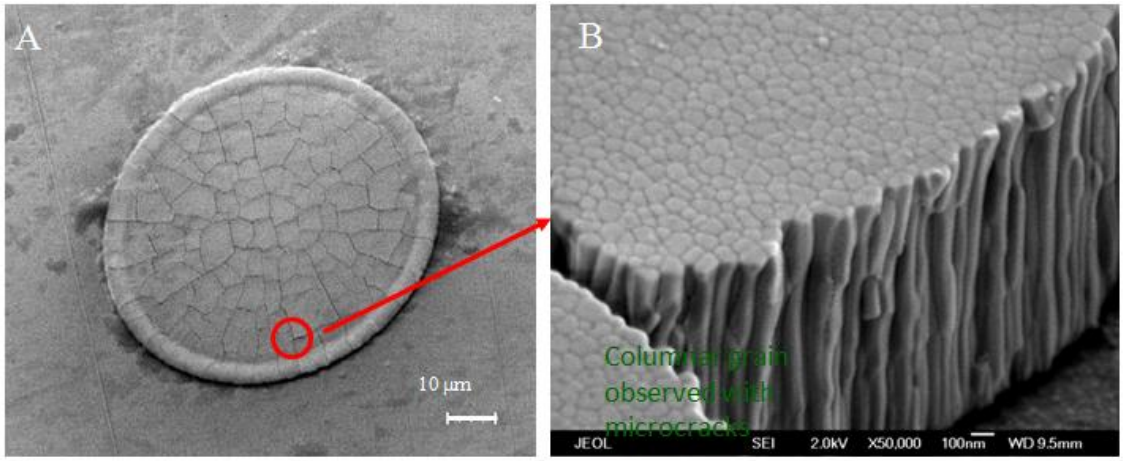

Figure 3:Example of columnar grain grow in Yttria Stabilized Zirconia splats

1.4 Processing Effects in Thermal Spray

In recent years, researchers at the Center for Thermal Spray Research at Stony Brook have advanced the understanding of the linkage between particle states and coating properties through the use of "process maps". Here the process map is defined as an integrated set of relationships that link processing to properties and ultimately to performance[17]. A key strategy is to develop relationships between the process parameters or feedstock with the spray stream characteristics (defined as a *first order process map*) followed by depicting the relationship between spray stream kinetic and thermal parameters with design relevant coating properties (*second order process maps*). These maps not only allow tailoring of properties via the process for design but enable assessment of coating reliability and process efficiency.

Past research at Stony Brook has demonstrated the importance of process maps in enabling integrated understanding of the thermal spray process. These studies have been conducted for metals and alloys such as Mo[18], NiCr [19] and NiAl[20] among others and ceramics such as YSZ[21]. The principle goal of these studies is the understanding of process effects on ensemble properties of coatings such as porosity, elastic modulus and thermal conductivity. In this work, other issues such as coating phase evolution and functional properties of the coating are addressed in different ceramic oxide systems, being Titanium Dioxide the most studied material given its flexibility for thermal spray being a relatively low melting point ceramic. This study addresses new avenues of

process-material-property connections, such as the effect of the so called “non particle state parameters” or novel applications such the fluorescence of alumina-chromia flame sprayed coatings, the effect of TiO_2 stoichiometry on photocatalytic activity and different pathways of TiO_2 processing for obtaining different electrical transport properties

1.5 Chemical and Crystallographic Issues on Ceramic Oxides of Interest

As mentioned earlier, thermal spray coating properties are defined by the rapid solidification implicit during the process. In a classical approach, nucleation is considered as a thermal activation process in which the solid-like clusters or embryos are formed in the undercooled melt due to thermal fluctuations. In the case of thermal spray, the solidification rates are always elevated due to the high undercooling, temperature gradient, and dimensional differences between the splats and the substrate[22]. Ceramic thermal spray coatings will typically present different polymorphs of the feedstock ceramic. Due to the stochastic nature of the process and depending on the coating material and technique, there can be a preferential growth of meta-stable phases due to kinetic limitations, but in some cases thermodynamically stable phase under atmospheric conditions are obtained. This will be further discussed in following sections.

The existence of pores, cracks and inclusions in the splat structure and its effect on thermal[23] and mechanical[24] properties of coatings has been thoroughly documented. However less importance has been given to the study of point defects such as vacancies of oxygen, in the case of ceramic oxides, or certain metallic interstitial or substitutional imperfections. The principles governing the creation of point defects of thermal spray coatings are believed to be fundamentally the same as bulk ceramics. The differences in oxygen pressure and temperature in the surrounding atmosphere create stochiometry changes in the crystalline structure of the flying particle. The differences of thermal input to the molten particle and the chemistry of the surrounding atmosphere are a function of the process and process parameters chosen for spraying. The effect of spraying conditions and particle state on the defect concentration of thermally sprayed coatings has not been documented thoroughly. Understanding the phase distribution behavior and point defect structure of thermally sprayed coatings is a key step in the coating design of novel applications such as sensors, photocatalytical coatings, and sputtering targets among others

1.5.1 Titanium Dioxide

TiO_2 is the most investigated crystalline system in the surface science of metallic oxides[25]. The two most common polymorphs of TiO_2 are Rutile and Anatase, others such as brookite or the reduced magneli phases are less common. Titanium Dioxide applications range from being an additive into most types of commercial paint,

substituting lead -as an opacifier because of its excellent reflective properties - to being a gate insulator in the next generation of MOSFETS[26]. Some of its novel applications include photocatalysis, solar cells, sensing and biocompatible coatings.

There has been an increasing interest to understand the mechanisms in which either the stable Rutile or the meta-stable Anatase phases are formed in the coatings. Since certain phases present better results for different applications. For example if the goal is to obtain coatings with enhance mechanical properties, dense HVOF 90%+ Rutile coatings have shown optimal results[27] In a different case, if the goal is to obtain coatings with higher photocatalytical activity for the decomposition of NO_x suspension plasma sprayed coatings with over 90% Anatase fraction presented the most favorable outcome [28]

There is ambiguity about the factors that control the phase distributions obtained with TiO_2 thermal spray. Lee[29] and Bertrand[30] suggested that Anatase is obtained by unmolten fractions of the original feedstock., Nevertheless, it does not explain why some Anatase is encountered even when the powder feedstock is purely Rutile[31]. In addition, other authors believe than increasing the fraction of secondary plasma gas –which usually increases enthalpy and/or thermal conductivity of the plasma-, will also increase the amount of Anatase obtained[32]. A theoretical model linking the undercooling levels with the phase distribution of the coatings has been proposed [33], this model suggest that completely molten particles will solidify faster, fostering the nucleation of Anatase during solidification. This hypothesis seems to contradict the experimental results of previous authors.

Differences of photocatalytical behavior between Anatase and Rutile are still motive for debate. For example some authors suggest that Anatase is more efficient in creating electron-hole pairs and absorbing Oxygen Ions, which will promote a reduction-oxidation reaction[34]. On the other hand, Bacsa[35] affirmed that mixed phases possessed a significantly higher catalytic activity due to the improved charge carrier separation in the mixed phase. Other authors even suggested that the crystallinity of the photocatalytical surface is as important or more than the phase distribution, since smaller crystallites will promote the abundance of hydroxyl groups providing more active sites for the degradation reaction[36].

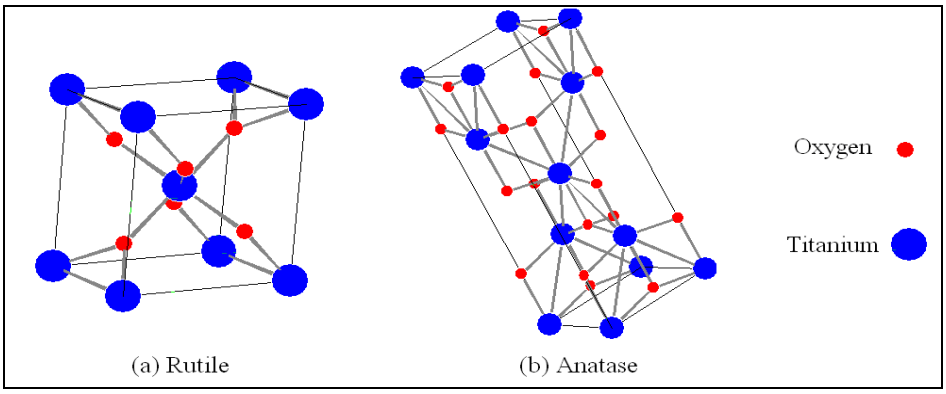

Figure 4: The polymorphs of Titanium Dioxide, Crystallographic data taken from [37]

The level of oxygen vacancies in APS TiO_2 was also studied by Wang et. al[32] using X-ray diffraction and Rietveld analysis; they calculated the vacancy level to be about 0.08 and 0.1 formula units of oxygen. However in their work no link was found between this non-stochiometry and the process parameters used. Brandland[38] found a relationship between the electrical resistivity, and particle temperature for plasma sprayed coatings, this relationship suggest a process to coating stoichiometry link, since reduced TiO_2 presents a higher electrical conductivity as the oxygen vacancies will act as charge carriers easing electric flow[39]. Most literature on Thermal Spray TiO_2 coatings has focused exclusively in coating characterization, An in depth study which integrates molten status analysis with characterization covering a wide range of process conditions has not been carried out so far. Although models about the vacancy entrapment on metallic thermal spray coatings have been proposed[40], the relationship between in-flight conditions and point defect concentration is an unanswered question. Titanium Dioxide presents non-stochiometry levels very sensitive to its surrounding conditions[41] which makes it an ideal material to study point defect kinetics on ceramic thermally sprayed coatings. The Point defect concentration will also have a noticeable effect on the optical properties of the coating since a highly reduced TiO_2 surface will present a dark blue tone in contrast with the white stoichiometric material[42]. Furthermore, questions on the effect of vacancy concentration on TiO_2 Photocatalytical activity are still unanswered and will be addressed in the functional properties chapter of this work.

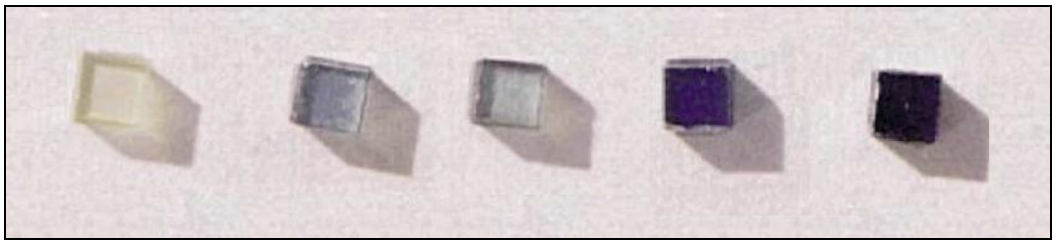

Figure 5: Single Crystals of Titanium Dioxide show different colors as a function of annealing temperature and surrounding atmosphere. Adapted from [43]

1.5.2 Aluminum Oxide + Chromium Oxide

Aluminum Oxide is a commercially produced ceramic with a wide range of applications, which range from abrasives to electrical insulators. Its diverse uses as a protective coating in surfaces range from hard-wood flooring to compact fluorescent lamps. A very common application is the electrolitically enhanced growth of an oxide layer in aluminum parts to improve surface properties. In Thermal Spray its applications include Wear, Corrosion and Thermal Protection.

Chromium Oxide, which has the same crystal structure as the stable alpha alumina can be mixed with Alumina to improve mechanical properties of thermally sprayed coatings[44]. Both have approximately hexagonal close-packed oxide ions with the Al^{3+} or Cr^{3+} ions occupying two thirds of the available octahedral interstitial sites. A technologically important application of the Al_2O_3+Cr_2O_3 system is the fabrication of scintillating screens for the imaging of accelerated Ion Beams. Such an example is the need to accurately measure beam density on the mercury target of the Spallation Neutron Source in Oak Ridge National Laboratory[45]. The adequacy of the Al_2O_3+Cr_2O_3 for this fluorescence application relies in photo stimulation and subsequent radiative decay of exited d^3 electrons in substitutional Cr^{3+}[46]. Such composition scintillating screen has been previously manufactured by other methods like sintering[47], and the novel application of the thermal spray method for such beam monitoring techniques presents unknowns due to the polymorphic nature of alumina thermal spray.

Pure Aluminum Oxide is widely applied material for thermal spray applications and its properties have been broadly reviewed in the existing literature. Two papers published by McPherson based on Aluminum Oxide Studies are considered classic in thermal spray science, where the first proposes a model for the solidification and growth of different phases of alumina [48] and the second relates the Young Modulus of a Ceramic Thermal Spray Coating to the microstructure of the coating[42].

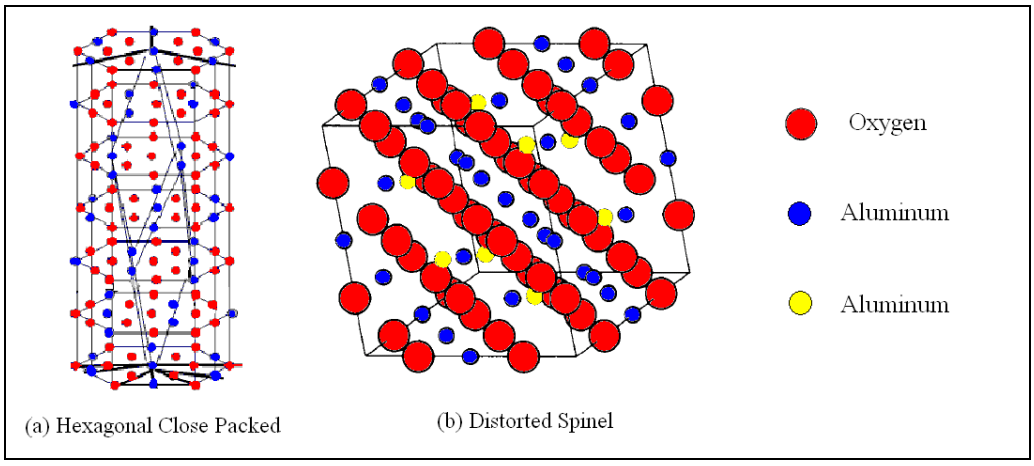

Figure 6: Common Polymorphs of Aluminum Oxide in Thermal Spray (a) stable α or corundum and (b) metastable γ. Adaped from [49]

The Two Most common polymorphs of Aluminum Oxide thermal spray coatings are the stable α and the meta-stable γ alumina . The first, also known as corundum, possesses the earlier described hexagonal close packed (HCP) lattice structure. The later one, meta-stable γ alumina, which in the thermal spray literature commonly referrers to a powder diffraction pattern consistent with the cubic spinel structure, but the definitive crystalline structure is still subject of discussion by many researchers[50]. Other polymorphs such as δ, θ, and η are also present. Glass alumina can also be obtained given the right deposition conditions[51]. According to McPherson's model, higher particle size will translate into a higher fraction of α phase present, usually nucleated from partially molten particles. Very high substrate temperatures will also stimulate the nucleation of α phase due to low undercooling. Gamma phase is usually not desired since it posses lower mechanical properties, and it can transform to α during high temperature service, increasing porosity due to a decrease in specific volume of the phase.

Previous work has indicated the feasibility of the Scintillating coating application with thermal spray and has also shown that flame spray is the technique with higher fluorescence intensity as compared with HVOF, APS or detonation gun spray[52], but an in-depth, process oriented study on the subject is first presented in this manuscript. Other applications of the Alumina-Chromia system include catalysis of pollutant removal of internal combustion engines[53] and strain determination on corroded scales of chromium containing alloys[54]. The coloration of alumina-chromia compounds is known to be an indicator of the crystalline structure due to the differences in the light absorption mechanisms of the Cr^{+3} ions present in the mixture[55]

1.5.3 Ytrtria Stabilized Zirconia

Zirconium Oxide in its pure form is commercially available for applications such as diamond substitutes or wide band gap high temperature semiconductors. ZrO_2 has 3 different polymorphs (shown in Figure 7) which are the high temperature cubic phase which is stable at temperatures higher than 2300 °C Tetragonal, stable from 1240 to 2300 °C and the lower temperature monoclinic phase. Pure Yttrium Oxide is present in diverse electronic applications. When a few percentages of Yttria are added to Zirconia the high temperature phases can be stabilized to atmospheric conditions, being the most common the T' phase, a variation of the tetragonal phase of technological implications for Thermal Barrier Coatings. TBC's are the most important application of thermal spray ceramic coatings. Substitutional Solution of Yttrium on the Tetragonal Zirconium Oxide and accompanying oxygen vacancies for charge balancing of the crystal foster the scattering of phonons, which translate into lower thermal conductivity of the coating. Point defect concentration increases ionic diffusivity of oxygen at high temperatures, this phenomenon has detrimental consequences in the service life of Thermal Barrier Coatings since the interface of the coating (commonly with a metallic alloy bond coat) is easily oxidized forming what is known as Thermally Grown Oxides[56]. This high temperature Ionic diffusivity is beneficial for some applications such as partial pressure of oxygen sensing in different combustion engine applications[57].

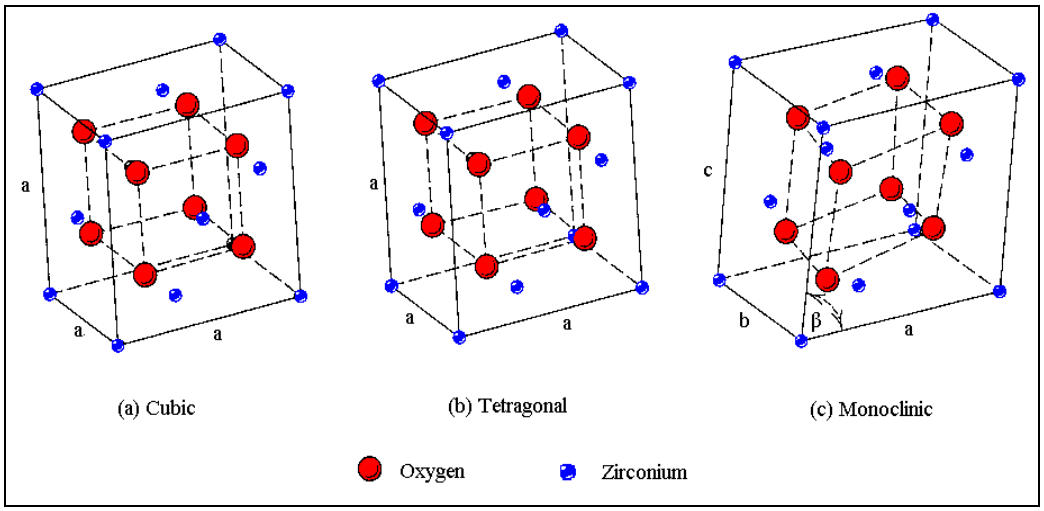

Figure 7: The polymorphs of Zirconium Dioxide, Taken from [41]

The life-time prediction of TBC-bond coat system life and understanding of the failure mechanisms is a task that has been incompletely accomplished by the materials scientific community. For this reason the turbine engine designers do not consider the thermal barrier coating as a permanent component of the turbine. If the coating delaminates the turbines are designed to support the high local temperature loads in the failed area of the

turbine until the next scheduled inspection is carried out. Improvements in process control and failure mechanism understanding would allow designers to consider TBC's as *prime reliant*[58], allowing for significant changes in design requirements and possible reduction of engine thrust-to-weight ratios among others.

Models to understand the TBC failure have been proposed[59-61] which include obvious factors as the growth of the TGO layer in the bond coat, coating thickness and operational temperature, and more intricate mechanisms such as the stress build up in the interfacial regions given the sintering of the YSZ layers. The deliberate growth of coating segmentation cracks (perpendicular to the interface) during spraying has been proven to increase coating life time and failure mechanisms[62], which leaves questions open on the relationship between coating compliance and cycle lifetime.

1.6 Statement of the problem

Recent studies regarding process control and manipulation have made progress in issues related to parameter optimization for functional properties such as of thermal barrier[63] or wear resistant[64] thermal spray coatings. Nevertheless several questions remain open regarding the integration of different technological and scientific improvements and their applicability to functional properties of different ceramic oxides, which this dissertation intends to address.

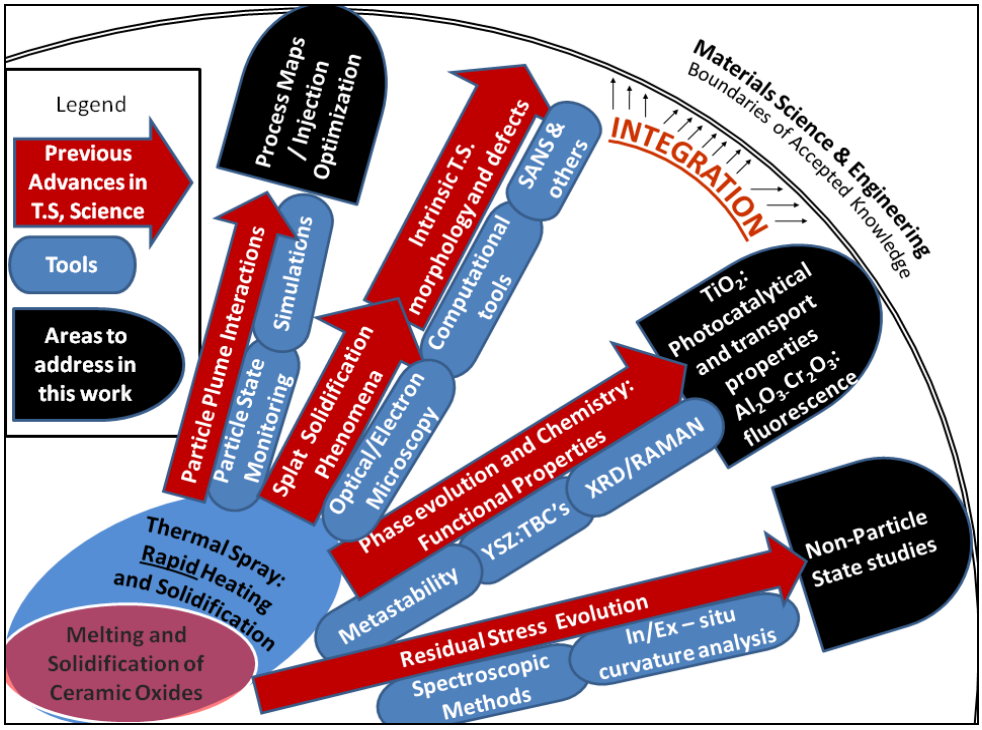

Figure 8: Methodological approach and contribution to knowledge in thermal spray science of this dissertation

Figure 8 summarizes the different areas on which this dissertation aims to advance the spectrum of knowledge in thermal spray processing science, delineating the previous research and tools where it sustains, some of the methodological improvements are explained as follows:

1.6.1 Expanded Processing Capabilities

In recent work, Vaydia[4], Srinivasan[5] and Valarezo[65] have highlighted the fact that thermal spray research focused on torch parameters is limited by unique hardware limitations, focusing process studies in particle state will ensure an objective point of reference comparing different processing conditions regardless of torch or process applied. Nevertheless their work was focused on unique processes (APS, High Velocity etc.) this dissertation will combine the use of a wide range of processing techniques to validate theories regarding to intrinsic coating behavior such as phase evolution or stoichiometry and functional properties such as photocatalysis, fluorescence and transport behavior. The consistency of particle state measurement techniques will also be addressed by means of cross-comparison between different systems. The use of visualization techniques will allow us to better understand previous findings regarding particle plume interactions

1.6.2 Particle and Non-Particle State Parameters

Both Valarezo and Srinivasan also addressed issues pertaining to particle state and non-particle state issues, this dissertation aims to further the understanding of issues regarding melting state and particle kinetic energy vs. deposition rate issue and their implications of functional properties since Valarezo and Srinivasan limited their work to explain evolving stress phenomena only and research by other laboratories have focused deposition rate studies uniquely on issues regarding life-time improvements in TBC's[66]

1.6.3 Integration of Novel Techniques and Characterization Methods for Ceramic Oxides

The inclusion of solution/precursor thermal spray in a combined process with other traditional techniques, and the correlation between stoichiometry, electrical, photocatalytical and crystalline structure of titanium dioxide for the first time addressed. Previous work no all these subjects have been carried out in an isolated manner. The study of alumina-chromia coatings is limited to the flame spray technique and fluorescence applications, given the recently discovered applicability of the system for thermal spray applications[52]. Special attention has been giving to the correlation of splats properties as the building blocks of thermal spray coatings to the ensemble characteristics of the coatings.

Chapter 2. Experimental Techniques

2.1.1 Plasma Spray

Plasma spray is one of the variants of the thermal spray technique; its main characteristic is that the heat source for the particle melting is provided by the enthalpy liberated during the recombination of ionized gases. Such ionic recombination can elevate the flowing gas temperature well over 8000 K [67].The high temperatures and elevated concentration of ionic species is what defines the thermal source as Plasma or the *forth state of matter*, given is entirely different properties as compared to the non-ionized original gas flows which are usually Ar, H_2, N_2, He or a combination of them.

The ionization method is a key factor in defining thermal plasma properties, for the thermal spray method direct current is the most frequently used power source although radio frequency (RF) plasmas are also common. It must be noted that for direct current plasmas, although the current source is "constant" the ionization process, caused by a capacitive break between the nozzle (anode) and the central cathode is not steady (see Figure 9) the Arc tends to lengthen given the influence of the flow momentum [68] de-attaching and attaching again at a shorter length, this phenomena causes instant variations in voltage in a rate of about 5 kHz depending on the parameters used.

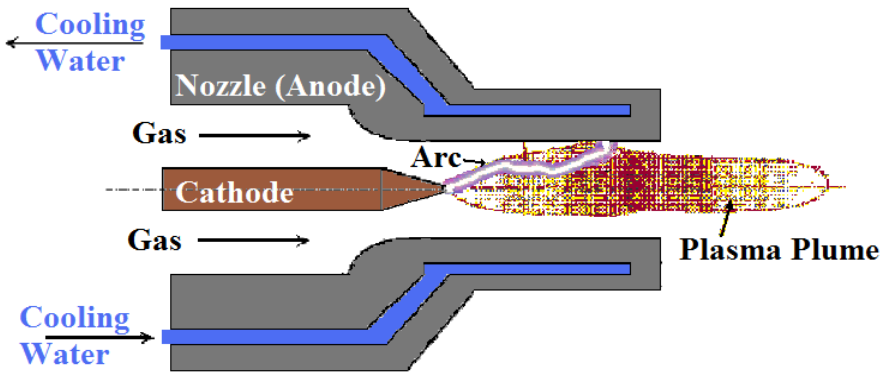

Figure 9: Plasma Spray Torch Principle of operation, adapted from[69]

Another aspect for classifying thermal plasmas is the operational pressure, which will be key in controlling the recombination phenomena, the length of the plasma flame or *plume length* and the interaction with the surrounding atmosphere. The later is a key phenomenon in defining plasma sprayed coating properties since the oxygen (or lack of such) in the surrounding will control the oxidation (or reduction) levels in resulting coating.

This work will mainly focus in the use of Ar-H_2 direct current atmospheric plasma spray, although Helium is also used in selected experiments through the manuscript.

2.1.2 Flame Spray

Also known as combustion Spray, Flame Spray is the variant of the thermal spray technique on which the heat for melting is provided from the flame resulting of combustion of a mixture of fuel and oxygen gas. Usually acetylene is used as the fuel. Given the lower flame temperatures relative to plasma the material feedstock is limited to metals or low melting point ceramic materials. Flame is pray is the technique with lower gas velocities also resulting in lower in-flight particle velocities, therefore the amount of time metal particles stay interacting with surrounding oxygen during deposition is significant enough to result in relatively high oxide contents in the coatings which are of detriment to coating quality. The low velocities also mean lower momentum at impact which results in porous fragile coatings, for this reason flame spray has been relegated to lower end technological applications, although novel applications for this older/basic technique are resurfacing to the scientific community, such as the previously mentioned spraying of coating targets for fluorescence mapping in radioactive beam sources.

Figure 10: TheroDyn Flame Spray Torch used for the work described in this manuscript

2.1.3 HVOF Spray

HVOF is in principle a modified flame spray method, the heat source is the same – a combustion flame – but the advanced torch design allows for the rapid acceleration of gases to velocities of 1000 m/s and higher. The fast flowing gases transmit their momentum to the feedstock particles which accelerate to velocities in the range of 500-800 m/s, compared with 100-300 m/s of APS and 50-100 m/s of flame spray. The high velocity/momentum of the particles reduces the interaction with the surrounding atmosphere limiting oxidation and results in a dense well adhered coating. Given the low flight time of the particle, the time span for melting is also reduced, which limits the particle size of HVOF materials compared to its slower counterpart techniques. Melting of ceramics is only possible in certain commercial torch types[70] and lower melting point feedstocks.

The type and flow of gases in HVOF spraying will define the coating characteristic, typical fuels include but are not limited to Propylene, Propane, Acetylene, Methane and Hydrogen. Some torches use a mixture of air and pure oxygen as oxidizing agent, while others are limited to pure oxygen (avoiding the heat absorption by nitrogen in the air). The fuel to oxygen ratio is a key variable in controlling heat transfer to the particles, while the total amount of gasses defines the amount of drag force imparted to the particles controlling their velocity.

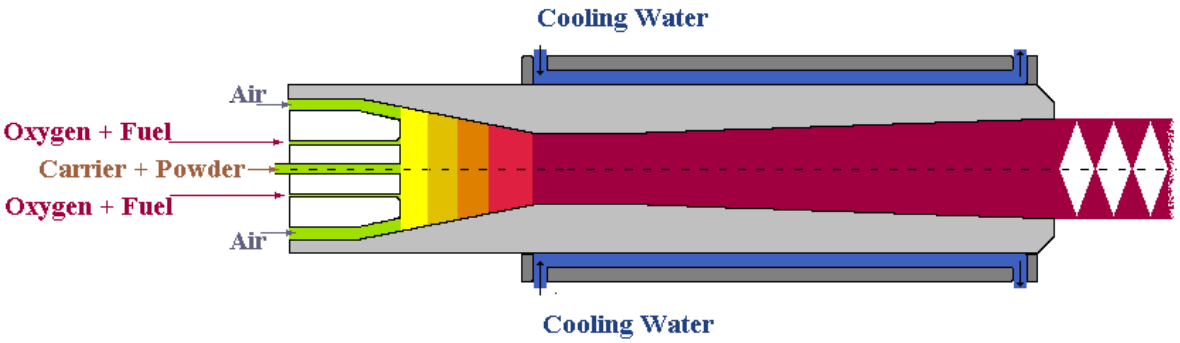

Figure 11: Schematic layout of a Diamond Jet HVOF torch, adapted from[71]

2.1.4 Thermal Spraying with Liquid Feedstock

It is widely accepted that conventional thermal spraying of powders have technical limitations on the particle size of the material to be applied, if the powder is too small (e.g. less than 5 µm), the flowability of the powders is severely compromised. The carrier transfer of momentum to the particles (by drag force) will be inefficient since the particles are easily affected by turbulence and do not accelerate on the desired direction, they will also easily attach to the tubing and metallic surfaces of the hardware creating clogs. For HVOF torches, too fine particles can melt on the exit of the injection orifice creating clogs and blocking the subsequent flow of powder. In radially injected APS torches, the momentum of the particles is never enough to penetrate the plasma plume and the feedstock is just blown away by the colder regions of gas stream, in general the low mass of nano-sized feedstock is a limitation for conventional thermal spray methods[72].

These limitations have restricted the application of nanosize powder materials with thermal spray technology. Alternative approaches consist of the agglomeration of nanosized powder into a nanostructured coarser material, but this approach is rather instable, given the high possibility that melting and re-solidification will destroy the original nano-sized microstructure or that resulting coating is not well adhered given the lack of melting [73], other approaches consist on spraying materials that recrystallize in

nanodimensioned grains or microstructures[74], but none of those approaches solve the question of how to inject nano-sized feedstock into the plume for spraying and exploring significant differences such as a considerable increase of the density of splat-splat interfaces in the coating and thermodynamic and kinetic changes due to size differences in surface energy .

A novel approach consist in injecting a liquid suspension of the feedstock material, since the liquid will have enough momentum to flow through the injection tubing and penetrate the plasma or flame the size range of particles to spray is considerably widened to include colloidal solutions in the order of tens of nanometers. The liquid injection approach includes its own technical challenges; heat input must not only melt the feedstock material but also evaporate the solute. The complex dynamics of fluid atomization difficult the understanding and controlling of the heating/evaporating/ melting process[75] but so far this technology has shown very promising results in obtaining nanodimensioned microstructures and coating with phase content that differs from conventional thermal spray coatings.

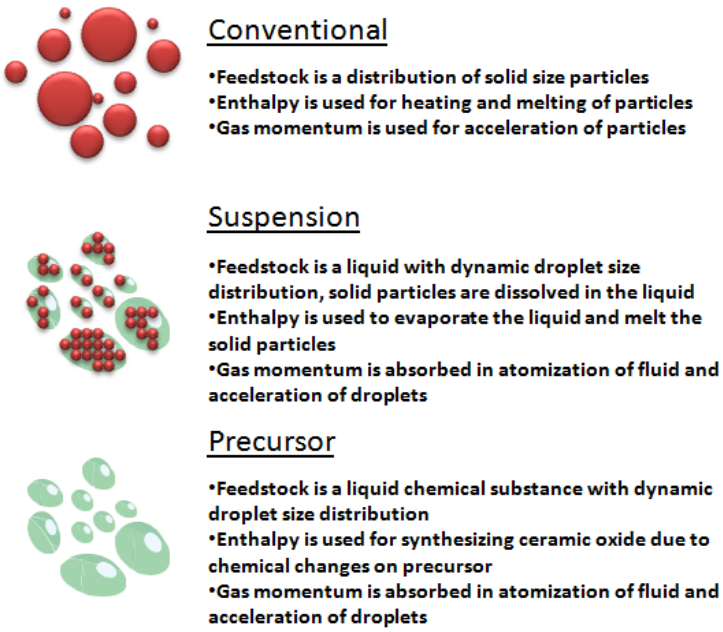

Figure 12: Schematic of differences between conventional and liquid thermal spray techniques

Another interesting application of liquid feedstock thermal spraying is the utilization of a precursor feedstock known to react with oxygen at high temperatures[76]. Thermal spray can be used as a mean to rapidly oxidize the precursor and project the resulting ceramic oxide to a surface. The fine size of the precursor droplets can result in novel nanostructured microstrucutures and the powder processing steps used for manufacturing conventional thermal spray powders could be avoided resulting in significant cost

reductions. The fundamental differences between conventional powder spraying and the novel liquid methods is summarized in Figure 12

2.2 Particle State Monitoring Techniques

Both scientific curiosity and market demand for high quality coatings have driven the thermal spray community to develop technologies that permit the in-flight monitoring of particle stream state. Several approaches have been utilized to develop instruments that measure the velocity and/or temperature, and in some cases size of the flying particles[5, 77-79]. Some sensors have also given basic geometric information of the plasma stream. So that by knowing the status of the particle stream, the formation mechanisms of the coating can also be controlled, and thus the properties of the coatings can somehow be predicted. These sensors have helped improve the repeatability of the thermal spray process[80, 81]; however there still serious challenges in dominating this process.

The different physical principles employed to determine particle velocity monitoring range from particle image velocimetry[22] (with Oseir's Spraywatch being a commercial example) to Phase Doppler Anemometry[23] A common method consists of measuring the radiation emitted by the particles with two CCD detectors of known geometry. If the time delay in the signals between the two detectors is known, then velocity can be determined (Figure 13); commercial examples of such sensors are Tecnar's DPV2000 and Accuraspray

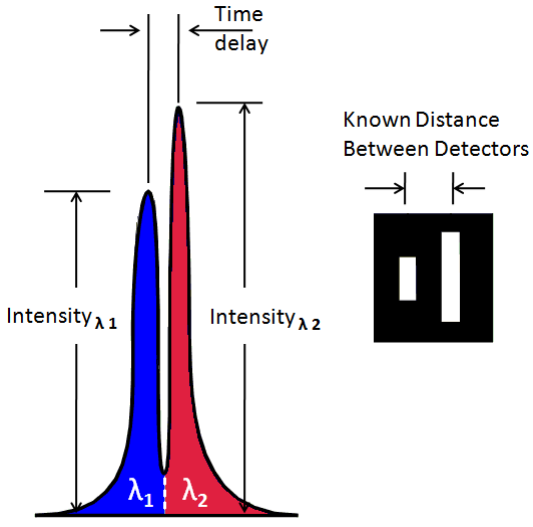

Figure 13: schematic of two-wavelength pyrometry and time of flight method, adapted from[82]

In-Flight particle temperature is measured by the two wave length pirometry method, which consists in quantifying the intensity of the surface radiation emissions at two different wavelengths of the electromagnetic spectra (usually infra red or near infrared).

As it will extensively discussed in this manuscript, for APS monitoring the injection of powder into the plasma stream has been proven a significant step in controlling and optimizing thermally sprayed coating[83]. There are different approaches for injection monitoring which include the use of a line intensity camera to monitor injection angle[84]. Most commercially available sensors can monitor plume geometry. Examples of sensors that were utilized in the experimental part of this manuscript are listed in Table 1

Another approach to monitor injection is real time imaging with a laser/camera set up[85]. Since the Plasma emissions are very bright, the camera must be filtered for most visible light wavelengths, and the small fraction of the spectra that the filter will allow the camera to sense is enhanced by the projection of a laser beam into the injection particle stream. This approach is also the fundamental principle of Spraywatch/Hi-Watch commercial thermal spray imaging system which is explained in Figure 14

Another key factor in understanding differences between different particle sensors is the distinction precision for particle stream monitoring. Some sensors will use the emissions from the overall particle stream, measuring *ensemble* particle states, while others have the capability of differentiating and measuring *individual* particles. Accuraspray and SPT are examples of ensemble measurements, DPV of individual. Spraywatch uses applies ensemble measuring for temperature but individual measurements for velocity.

It must be also noted that particle temperature and velocity measurements represent only a first order approximation of the in-flight particle state that could be rather limited. For example, previous work shows that spray conditions with different torch parameters can have the same mean particle temperature and velocity but significantly different particle temperature statistical distributions[86]. Diverse approaches have been developed in Stony Brook to better access particle stream characteristics to improve process/coating consistency and reliability[81]: Residual Stress, Coating Modulus and In-situ Curvature Measurement and advanced particle state indicators, these approaches are described as follows:

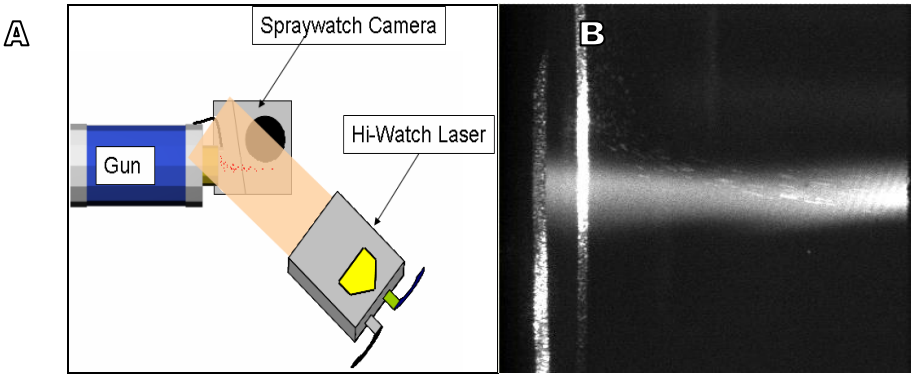

Figure 14.A: Typical set up of Hi-Watch Particle Injection System
Figure 14.B: Example of visualization of particle injection into plasma stream

2.2.1 Advanced Particle State Indicators based on commercial sensors particle state measurements

Melting Index

Defined as the ratio of the in-flight particle time, to the time required for a particle fully melted and is given by the equation:

$$M.I. = A\frac{12 \cdot k_l}{\rho L} \cdot \frac{1}{1 + 2/Bi} \cdot \frac{(T_s - T_m)S}{r_p^2 \cdot V_p}$$; where

A: is a non dimentional temperature that relates the flame (plasma, HVOF etc.) temperature with the surface temperature of the particle at impact
k_l: is the thermal conductivity of the molten particle
ρ: is the density of the particle
L: is the latent heat of fusion of the particle material
Bi: is the Biott number of the particle, which relates the convective heat transfer of the particle with its surrounding atmosphere with the internal heat conduction of the particle.
T_s: is the surface temperature of the particle at the time of impact (which is measured by commercial two wavelength sensors)
T_m: is the melting temperature of the particle
r_p: is the radius of the particle and,
V_p: is the particle velocity at the time of impact, also measurable by commercial sensors
S: is the particle distance from the gun at the time of measurement.

Kinetic Energy

Defined as: $E_k = \frac{1}{2} \times m \times v^2$ where

E_k *:* Kinetic energy of the particle
m: Mass of the particle. To calculate it the density of the powder must be known and the diameter must also be measured by a commercial sensor such as DPV2000 or SprayWatch.
v: velocity of the particle

These two parameters, Melting Index and Kinetic Energy, take into account the thermal phenomena involved in the processing of individual particles to quantify the level of molten content and how much inertia the particles will posses to drive the flattening at impact. Both indicators can be directly correlated to deposition efficiency and several morphological characteristics of the splats and coatings[5]

Commercial Sensor Name	Plume Geometry Measuring Principle	Explanatory Graph
DPV2000	Scanning of cross section of plasma stream and measurement of XY location point of highest particle flow	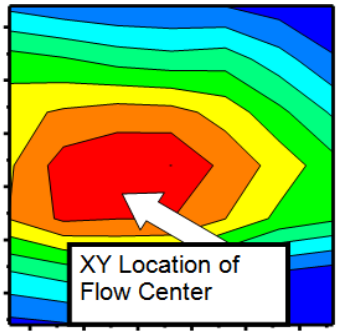
Accuraspray	Image analysis of video signal for calculation of injection direction/plume depth	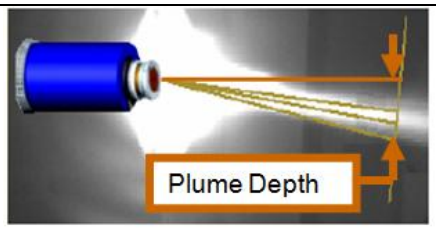
Spraywatch	Image analysis for determination of geometrical particle flow distributions	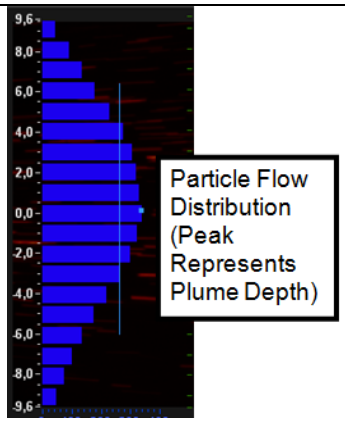
SPT	CCD camera for Line intensity measurement of particle flow geometrical distributions	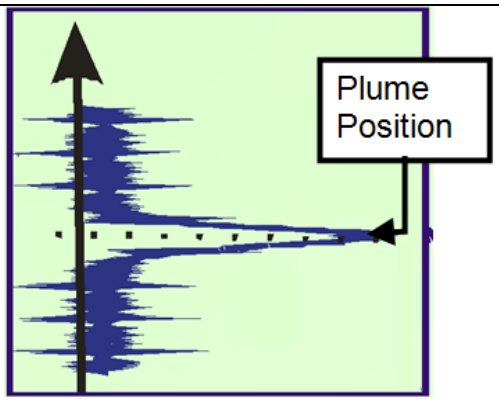

Table 1: Principle of Geometrical Description of Particle Stream by Different Commercial Sensors

2.3 Residual Stress and Curvature Monitoring Techniques

Residual stresses in thermal spray coatings are caused by the large temperature gradients inherent to the process. When the molten particles impact the substrate, a very dynamic process takes place involving the rapid quenching and solidification of the particle. Since solids will normally have a lower specific volume than molten materials the particle tends to contract, but the contraction is limited by the adherence to the substrate. This contraction restriction causes stresses known as the *quenching stress*[87]. The thermal spray plume does not only melt the feedstock material, but also convectively transfers heat to the substrate increasing its temperature. After deposition both the substrate/coating system cools down, but since the thermal expansion coefficients are different, a thermal *mismatch stress* is developed. Although this two mechanisms are the main contributors to coating residual stress in APS [88, 89] in high velocity processes the impact of unmolten or high kinetic energy molten particles can induce deformation with compressive stresses and strain hardening, this mechanism is known as *peening stresses*[65] Residual Stress levels are key for a coating structural integrity and its performance. If too high they can induce cracking and delamination and even substrate deformation. During part service the coating could be subject of additional stresses, either mechanically or thermally induced. If the stress levels are higher than the coating bonding stress catastrophic failure might occur or more commonly failure will be caused by cycling stress loading fomenting fatigue crack growth. In some cases compressive coating residual stresses can be beneficial for inhibiting crack growth, or by simply superposing an opposite operational stress, increasing fatigue life of the substrate/coating system.

Different methods exist for quantifying final residual stress levels in thick film coatings, most of them involving spectroscopic techniques such as X-ray diffraction, Stony Brook CTSR has developed in-situ and ex-situ curvature techniques which can dynamically monitor coating stress/strain levels during deposition and induced thermal mismatch[90]. This technique will be briefly described below. Another key property of the coating is its elastic modulus which is related to coating structural integrity and bonding quality[42]. The Young's Modulus is directly correlated with residual stress level, since a stiffer coating will be less capable of containing elevated stress levels. Stony Brook's curvature analysis methods also address elastic modulus quantification.

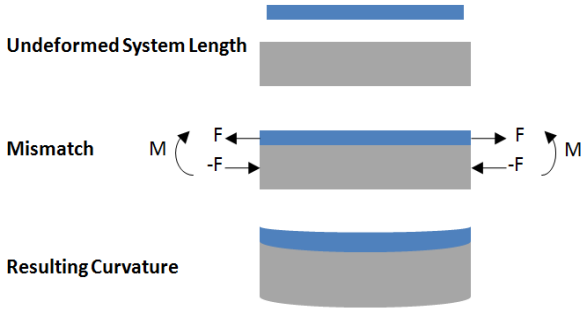

Figure 15:Principle of stress/curvature generation during spraying, adapted from [90]

The fundamental principles of Stony Brook's curvature method were originally introduced by Stoney in 1909[91] and later expanded by other authors [92]. The first applications of these theories in Thermal Spray were executed by Kuroda et al.[93]. The operational principle is the following: residual stresses, whether quenching or mismatch induced creates a force unbalance between the substrate and the coating. This force is transmitted to the substrate, which stresses and curves to balance the force disparity by creating a counterbalance force. If this curvature change is monitored continuously during deposition thickness growth the resulting stress levels can be estimated with the use of force balance equations and the known geometry of the system. A schematic of the basic principle of curvature monitoring is shown in Figure 15. The Young's modulus of the coatings is calculated from the curvature and temperature evolution during post-deposition cooling. Assuming the temperature mismatch force is known from the CTE and temperature changes, the strain can be calculated from the curvature evolution and a stress/strain plot is easily constructed. This stress/strain gradient during cooling is by definition the coating's elastic modulus.

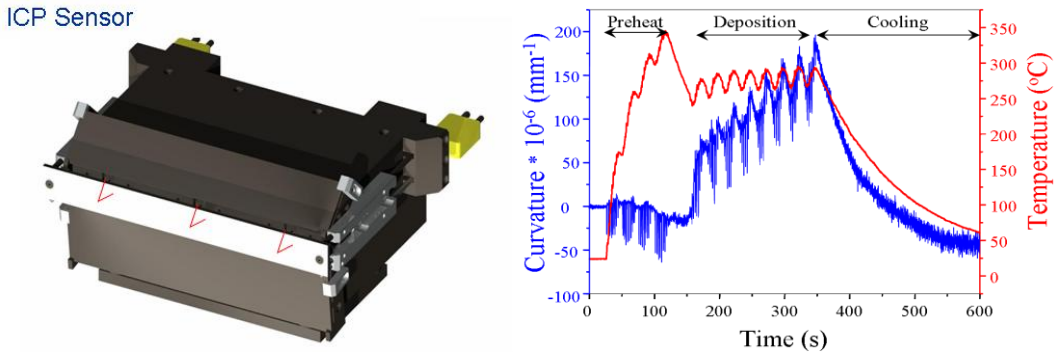

Figure 16-a: the in-situ curvature sensor
Figure 16-b: typical in mediate output of the sensor (before processing)

The curvature measurement instrument or ICP is shown in Figure 16-a. It employs laser displacement sensors in the back of the substrate. Assuming the curvature to be completely circular, knowing the position of 3 points of the surface allows for geometrical determination of the curvature radius. Contact thermocouples are also

included in the setup to allow for simultaneous measurement of curvature and temperature. A typical example of displacement and temperature measurements are shown in Figure 16-b

In the stress calculation procedure applied in this work a Bi-axial stress state is assumed in both axis of the coating plane, the in-plane Young's modulus is calculated by the equation

$$E_c' = \frac{E_c}{1-\nu_c} \quad ; \quad E_s' = \frac{E_s}{1-\nu_s}$$

Where the s and c subscripts indicate substrate and coating respectively, ν is the Poisson's ratio of the materials, E is the Young's Modulus and E' the in-plane Young's modulus.

The change of curvature in as a function of thickness $\delta_{curvature}/\delta_{thickness}$ (the slope of the curvature change) allows for the calculation of the deposition stress using the Stoney approach[91]

$$\sigma_d = \frac{E_s' t_s^{\,2}}{6} \frac{dk}{dt_c}$$

With σ_d represting the deposition stress when a d_κ curvature change is caused by a coating thickness deposition dt_c , and with t_s being the substrate thickness. d_κ/d_t is usually taken after the first or second deposited pass because these layers usually are affected by interaction with the substrate.

The calculation of post-deposition thermal mismatch stresses is based on the Brenner and Senderoff's equation[92], where σ_t is the thermal mismatch stress in the coating and the change of curvature $\Delta\kappa$ is specific to the cooling region of the curvature response:

$$\sigma_t = \frac{\Delta\kappa E_s' t_s}{6t_c}\left(t_s + \left(\frac{E_c'}{E_s'} \right)^{5/4} t_c \right)$$

The coating modulus (E_c) used for the mismatch stress calculation can be obtained from bulk values (less recommended), indentation stress/strain experiments or using the cooling region of the curvature where the difference in thermal expansion coefficients of the substrate and coating is known ($\Delta\alpha$) using the following equation:

$$\frac{\Delta\kappa}{\Delta T} = \frac{6E_c{}'E_s{}'t_c t_s\left(t_s + t_c\right)\Delta\alpha}{E_c{}'^2 t_c{}^4 + 4E_c{}'E_s{}'t_c{}^3 t_s + 6E_c{}'E_s{}'t_c{}^2 t_s{}^2 + 4E_c{}'E_s{}'t_c t_s{}^3 + E_s{}'^2 t_s{}^4}$$

E_c can be numerically calculated sing the linear cooling region of the curvature temperature plot to determine $\Delta\kappa/\Delta T$

2.3.1 Ex-situ highly controlled variant

The ex-situ curvature property measurement technique or ECP follows the same fundamental principles as ICP, with the difference that the heating and cooling rates of the sample are precisely controlled and vibration caused by the spray gases is avoided. The use of this technique allows for distinction of behavior not previously seen by the ECP technique give then high amount of noise present even when the torch was heated with a torch after deposition. In this method the heat is supplied to the sample by an oven and not a flow of combustion or plasma gases.

Three main mechanical responses are quantified by the use of the ECP technique, the fundamental considerations for the computation of these attributes was first introduced by Nakamura et al.[94]

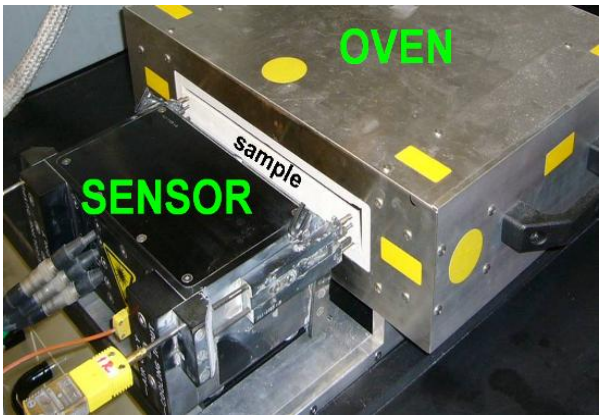

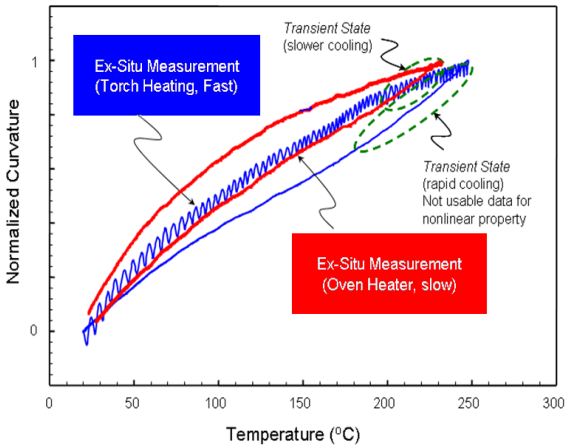

Figure 17-a: Ex-situ curvature sensor
Figure 17-b: comparison between controlled oven and uncontrolled torch curvature-temperature measurements

1) Young's Modulus: This is measured in the lower temperature region of the experiment where the response of the system is closer to a linear mechanism. The principles of calculation are the same as for the ICP

2) Non-Linearity: this represents the level of deviation from a linear elastic behavior and is found in the higher temperature regions of the experiment for some

materials, it is associated with crack/interface closure and opening during compressive and tensile loadings due to thermal mismatch

3) Hysteresis: this represents the difference in curvature paths during cooling and heating of the sample, it is associated with frictional sliding among interfaces.

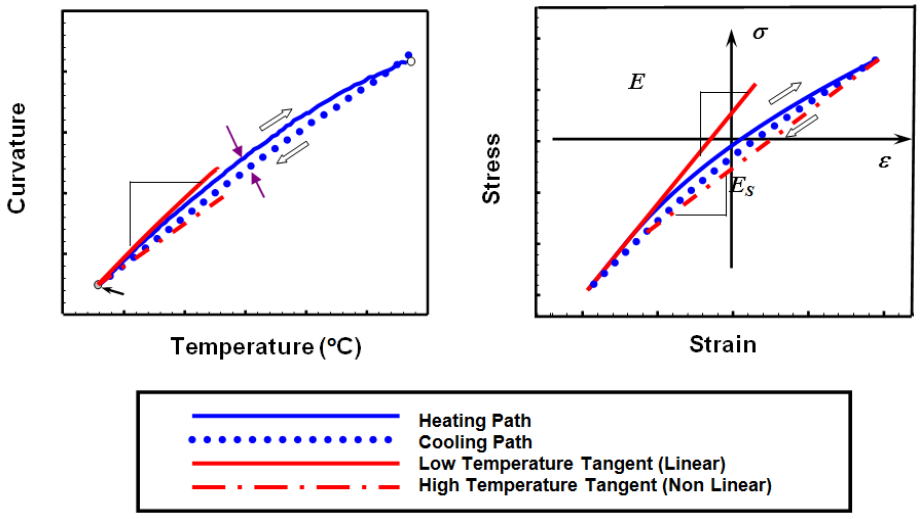

Figure 18: key outputs of the ex-situ curvature-temperature and stress/strain analysis

Figure 18 shows the different areas of interest in a typical curvature-temperature experiment on the ex-situ curvature sensor. The three key mechanical responses can be observed. First is the stress-strain slope at low temperatures (red solid line) which represents Young's modulus. The difference of behavior at low and high temperatures which is referred as the secant modulus represented by the red dotted line (explained in[94]) is a representation of the non-linearity of the system. The different trajectories of the heating and cooling paths of curvature represent the hysteresis of the system, in which the starting and ending point will not necessarily be the same.

2.4 Coating Characterization

2.4.1 XRD

X ray diffraction based on Bragg's law is probably after optical and electron microscopy the most common method of characterization in modern materials science. Since its application theories are widely understood by the scientific community and its use is considered conventional in both industrial and scientific settings we will not explain the operational principles of this technique in this manuscript as it is well explained in the literature[95]

2.4.2 Microscopy

A detailed description of both optical and electron microscopy principles can also be found in detail elsewhere, but it is worth mentioning that although extremely useful, both

these techniques have limitations on characterizing the microstructural features resulting from the complex formation dynamic of thermal spray coatings. The defects resulting from splat overlapping are morphologically different depending on their formation nature. For example, there is globular pores resulting from incomplete melting of particles and interlaminar pores due to imperfect splat contacts[96], some materials (typically ceramic) will present intra-splat microcracking due to stresses at solidification, while other materials will present inter-splat macrocracking also due to stress reliving mechanisms.

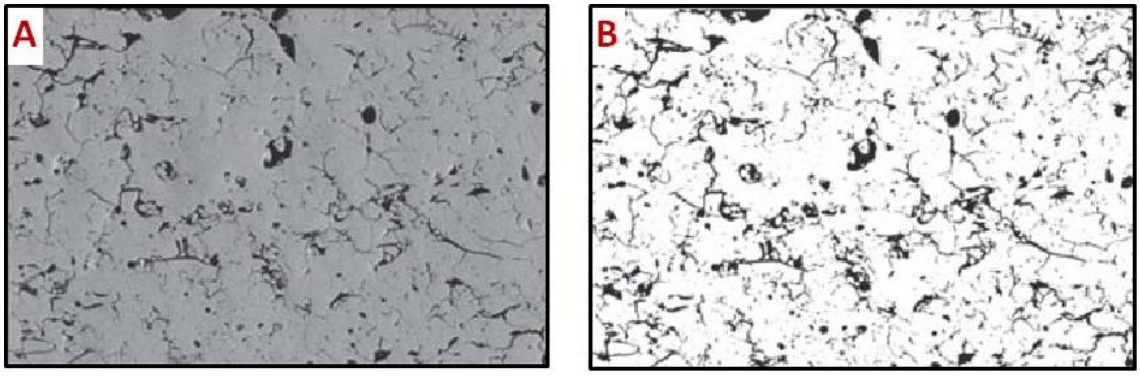

Figure 19: (a) Original SEM cross section microstructure (b) processed binary image (taken from[97])

Most industrial coating quality control procedures focus on the fraction of "empty" space of a cross section of the coating, calculated from a binary image of the original microscopic picture as shown in Figure 19, but this method fails to distinguish these differences and their implication on coating formation differences. Disparities in metallographic preparation parameters[98] and image analysis algorithms can yield differences in the results obtained for this methodology. More precise spectroscopic methods[99] have been applied to investigate in depth microstructural features of TS coatings, but these methods are not cost-effective for day to day industrial applications.

2.4.3 RAMAN Spectroscopy

Although less common than microscopy or x-ray diffraction, Raman Spectroscopy is also a well established technique in modern materials sciences. Used primarily for the analysis of chemical bonds is based on the spectroscopic analysis of inelastic scattering of phonons. When a coherent (laser) phonon source is projected into a sample the spectra of scattered light can be used as a fingerprint to identify bonds (and molecules) present. The main advantage of this technique for some parts of the work described here, as compared to x-ray diffraction is that a smaller beam size of down to ≈ 1μm can be applied with less technical complications required for precise aiming of an x-ray diffraction beam. A detailed explanation of the technique can also be found elsewhere[100].

2.4.4 Photocatalytical Activity

Photocatalysis is known to be a chemical reaction prompted by the presence of photons and a catalyst substance. The catalyst should be chemically structured in a way that fosters the creation of electron-hole pairs, which will interact with the free radicals of the surrounding compound. The ability of TiO_2 to create electron-hole pairs when illuminated with light of wavelength shorter than ≈415 nm was first discovered by Fujishima and Honda[101] in 1972. In this work, the photocatalytical activity of TiO_2 coatings is determined by measuring the degradation rate of methylene blue under UV light. The change of concentration of metylene blue is quantified by measuring the UV-vis spectra of the test solution over time.

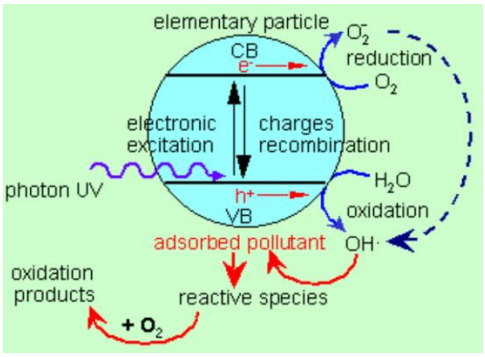

Figure 20: principle of Photocatalytical Pollutant Decomposition (taken from[102])

In this work 200 ml of Metylene Blue solution (with continous stirring) was illuminated by a long-wave ultraviolet lamp (UVP Model B-100A) providing radiation with a maximum intensity at 360 nm. Initially, the solutions were equilibrated with the catalysts in the dark for 30 min. To monitor the progress of the reaction the samples were periodically withdrawn from the solution, filtered through 0.45 µm membrane filters and transferred to a spectrophotometer cuvette for further analysis. The control experiments took into account the thermal effects related to solution evaporation and MB adsorption on the membrane

materials. The analysis was done in a double beam scanning UV-vis spectrometer (EVO-300). The reaction was assumed to be the first order with respect to MB concentration[103].

2.4.5 Fluoresence

The characterization of the fluorescence response of alumina-chromia coatings in this work was performed at the National Spallation Neutron Source in Oakridge TN (Figure 21-a). The intended application of this ceramic system is to manufacture coatings for a mercury target such as the one shown in Figure 21-b. The target emits neutrons when

bombarded by accelerated protons and the aim if the coating is to map the intensity and the shape of the incoming proton beam.

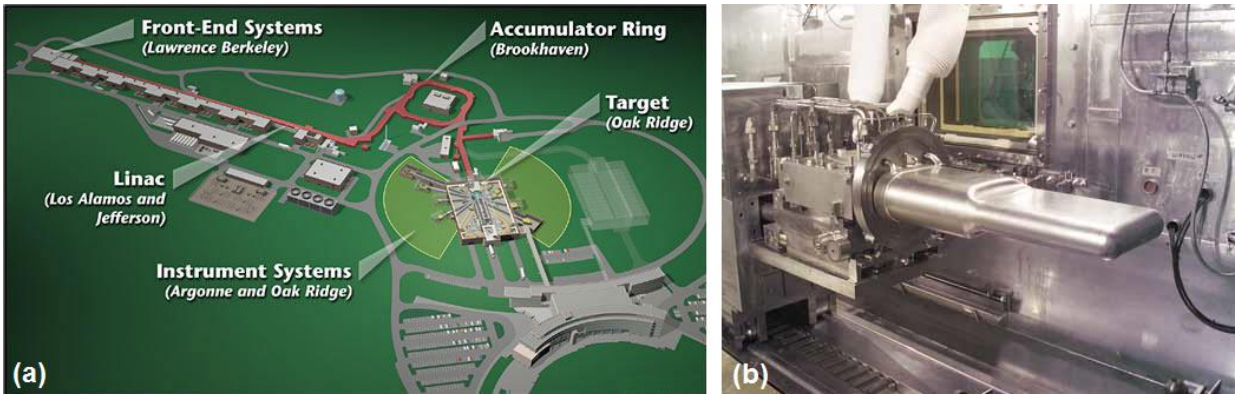

Figure 21: (a) layout of the National Spallation Source at Oakridge National Lab. (b) Liquid Mercury Target Container to be bombarded with H+ Ions for the emission of Neutrons (adapted from[104])

When the alumina-chromia coating is bombarded with accelerated protons, photons will be emitted given the correct composition and crystalline structure. The alumina-chromia coatings tested in this work were tested in a "beam dump" in Oakridge national lab that simulates the energy and pulsation of the ion beam to be applied to the target and the resulting fluorescence was measured and normalized to the intensity of a control ruby sample.

2.4.6 Thermal Conductivity

The ability to transmit heat through conduction (and to a certain extent internal radiation) is a key property in functional coatings for thermal barrier applications. Thermal conductivity is also an indication of microstructural characteristics of a coating and is defined by the lattice properties of the bulk material and the nature of intrinsic defects present in the coating. In this work this property was quantified by the use of a Holometrix laser flash thermal diffusivity instrument [105] (NETZSCH Instruments, Burlington, MA) Which measures the half time of the temperature increase of a material heated by a controlled laser pulse [106]. The temperature response of the side opposite to the laser beam is measured with an infrared detector, allowing the simultaneous measurement of thermal diffusivity and heat capacity of the sample, the thermal conductivity is then given by the equation:

$$K = \alpha \, . \, \rho . \, Cp$$

Where α is the measured thermal diffusivity, Cp the measured heat capacity and ρ the density of the sample.

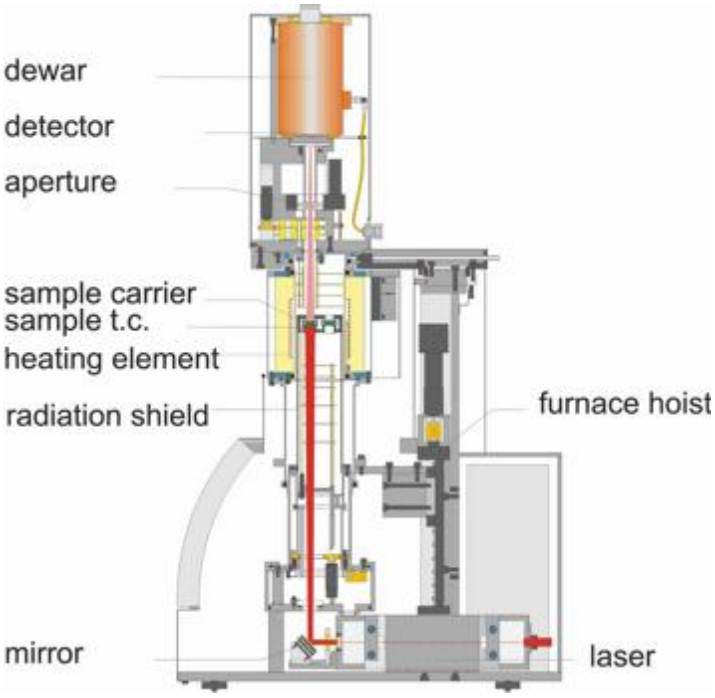

Figure 22: Schematic of Xenon Flash Laser Thermal Conductivity Instrument (Taken from [107])

2.4.7 Electrical resistivity / Impedance Measurements

Electrical transport properties are not only important from a functional point of view, as thermal spray coatings have enormous potential for application in mesoscale electronics, but also from a descriptive point of view to understand formation mechanisms and changes in coating stoichiometry and microstructure. In this work electrical measurements in the in-plane direction of the coatings were performed with the use of a Veeco FPP-5000 four point probe common in the industry for the measurement of resistive properties of semiconductor wafers and resistive films. The four point probe represents a repeatable and straight forward of measuring electrical properties, For an in-depth understanding of the microstructural implications of the system a more complex equipment: an Impedance Analyzer (HP 4294A) was utilized to observe the response of coating impedance to a wide frequency spectra[108].

Chapter 3. Particle State monitoring by two-wavelength pyrometry, time of flight method and particle injection visualization, assessment of different diagnostic approaches

3.1 Process Map Development for Plasma Spraying

The need to develop accurate process maps of particle state and coating properties for thermal spray has been studied in depth by the Stony Brook Center for Thermal Spray Research extensively [21], previous authors have analyzed the effects of torch parameters such as power [109]current [110]total flow of gasses [69] carrier gas flow and many others to conduct process-property relationship studies. Linking such relationships with particle state evolution is fundamental in constructing a solid description of specific material behavior.

Particle state monitoring and the construction of first order process maps -independently of the of base indicator selected such as Temperature or Velocity or more elaborated analysis such as melting index[111] or particle state distribution- is rooted in the assumption that the in-flight measured data is accurate, if this assumption is not correct and the particle state measurement is proven bias or subjective, the understanding of an specific material system and its application by thermal spray would be severely compromised

Several limitations are already known for the current method of in-flight particle temperature most used in industry: two-wavelength pyrometry. This method assumes that the surface emissivity of the measured particle is independent of the wavelengths of measurement[112](grey body assumption); this assumption is known to be incorrect and a cause of distortions in the measurement. When using the particle distribution analysis method, it has been found that the multi-modal peaks corresponding to the energy barrier at melting are located up to 200 °C from their theoretical location[86],a model to compensate for such errors has been developed for materials whose emissivity curves at high temperature is known has been developed but not applied industrially [113],also the possibility of plasma emissions scattering from the particle and distorting the measured temperatures has been suggested by some authors[24]. For this reason the wavelength of the detectors in the sensors are selected in order to avoid the wavelength of the plasma emissions, but this selection does not constitute a certain elimination of the possible measurement bias.

One difficulty for corroborating the accuracy of particle velocity and temperature velocity is that there is no direct physical technique to measure the temperature of the millions of particles in the stream and compare the data with the two-wavelength radiation measurements. One possible approach, to simulate the physics of the process by the use of powerful computational tools has been performed by researchers at Stony

Brook [114] and other research laboratories[115-117], this approach will be briefly applied in this work, but simulation work has the limitation of being based on theoretical calculations. Typically the results are later cross-compared with experimental results of the two-wavelength pyrometry measurements, which creates an outcome substantiation paradox "if we don't know if the simulation results are accurate, we compare them with the two-wavelength pyrometry results, if we don't know the two wavelength results are accurate we compare them with the simulation result"

The approach in this work was to perform measurements of deliberate particle state variations simultaneously with different commercial two wavelength sensors and cross-compare the result to check for inconsistencies and analyze the response of the different systems. This approach is by no means a silver bullet for resolving all the questions surrounding the two-wavelength pyrometry or time-of-flight methods, but observing the responses of systems that employs different detectors of different wavelengths, different electronic time-signal responses, filtering algorithms, optics and measurement volumes is a key step in expanding the knowledge of this intricate technology. Previous work addressing cross-sensor comparison was executed by Mauer et al.[118], who already gave valuable insight in operational limits and applicability of Accuraspray and DPV sensors, this work seeks to expand the knowledge base on the subject by including other sensors, processes and process parameter modifications.

The first step in performing comparative analysis of sensors is a solid experimental design to explore different regimes of torch operation and particle state variation, a DOE of process parameters was constructed with the assistant of the JMP 7 scientific analysis software, the parameters applied can be seen in Table 2 and Figure 23. Such parameters were based on a 8+1 experimental cube design. The levels of variation were set by taken into consideration (a) the safety operational levels of the torch and (b) known low energy parameters on which particle melting is difficult at best. It must be noted that this experimental design is intended to cover only torch operation related parameters and their relationship with particle state, there is a significant wider range of parameters key in defining thermal spray coating formation mechanisms, but since those are not directly related to particle state measurement (i.e. Substrate temperature, substrate roughness, robot raster speed) they were precluded for this part of the work.

The feedstock powder utilized was Saint Gobain fused & crushed HW 1623 Yttria Stabilized Zirconia powder. To avoid errors caused by inconsistencies in injection, the plume penetration depth was kept constant in all spraying conditions, which results in different carrier gas flows but a similar interaction if the powder stream with the hot zone of the plasma.

Table 2: Parameters used for simultaneous measurement Process Map

Condition #	Independent DOE variables			dependent variables	
	Ar Flow [slpm]	H_2 Flow [slpm]	Current [amps]	Carrier Gas [slpm]	Voltage [V]
1	47.5	6.0	550	3.6	65.3
2	35	6.5	450	2.5	63.9
3	60.1	4.4	650	4.8	63.9
4	47.5	6.0	550	3.6	63.9
5	59.7	11.1	450	3.9	73.9
6	59.7	11.1	650	4.7	75
7	35.2	2.6	450	2.8	53.5
8	47.5	6.0	550	3.8	64.3
9	35.2	2.6	650	2.8	55.2
10	60.1	4.4	450	4.31	61.5
11	35	6.5	650	2.7	63
12	47.5	6.0	550	3.7	64.3

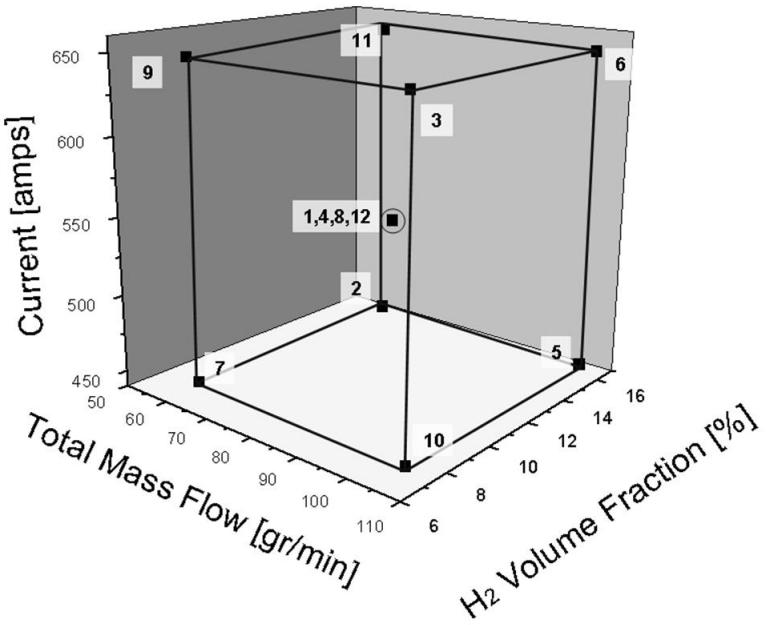

Figure 23: parameters chosen for the sensor comparison experimental design

3.2 Responses of Different Sensors to Parameter Modification

Simultaneous measurements of particle state where performed during the execution of the process map different process conditions, in the following section the results of these measurements will be summarized from an individual process parameter point of view.

From Figure 24 it can be observed that for the 3 sensors the increase in total flow of gases (Ar + H_2) results in an increase of the particle velocity. This increase of velocity is consistent in the remaining two sensors, and it is expected given the increase of drag force in the particles given the higher gas velocities.

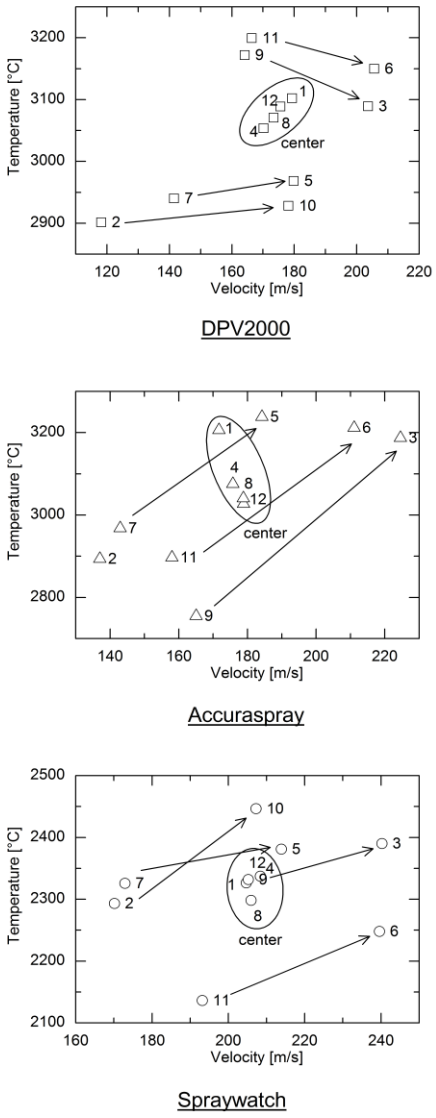

Figure 24: response of different sensors to variations in total flow of gasses. Arrows indicate increase of total gas flow keeping the rest of the parameters constant

The effect of total gas flow in particle temperature is not as clearly discerned, in theory a higher particle velocity should reduce the time-of-flight and the residence time of the particles in the hot zone of the plasma[119] although the possibility that a higher Reynolds number of the gas stream could improve the convective coefficients and improve heat transfer is not completely ruled out, such effect has not been observed by any previous researcher. For DPV, the higher current conditions experience a decrease of temperature, while the lower current conditions experience a slight increase of temperature, in the other two sensors, there is a marked increase of temperature with the increase of total flow of gases, which contradicts the DPV results. It must also be noted that for Accuraspray the spray condition 10 is not even present on the graph, since it was detected as a much hotter particle state T≈4000 °C which is clearly incorrect, being this particle with the parameters that should result in lowest particle temperature (low current, low hydrogen, high total gas flow)

From Figure 25 we can observe that in DPV the increase of torch current creates a slight increase of velocity and temperature for all conditions, this is expected since a higher level of electronic/ionic conduction should mean a higher level of ionization in the stream, thus a higher release in energy during the ionic recombination process[120] . This increase in temperature will also affect the expansion of the gasses in the nozzle, therefore a velocity increase is also expected. This increase in velocity trend is consistent between all 3 sensors but more marked in the ensemble sensors (Accuraspray and Spraywatch). The response of temperature between the ensemble sensors and DPV is contradicting, with the ensemble sensors showing a decrease in temperature with the increase of current.

In Figure 26 the response of the sensors measurement to hydrogen fraction in the stream is shown. For DPV an increase of hydrogen results in a measured increase of velocity- for 3 out of 4 cases- and almost no variation in particle velocity. Hydrogen is known to have a higher enthalpy of recombination than Argon [121] therefore the expected response would be an increase of temperature as shown by DPV, given the lesser density of hydrogen, a slight decrease of drag force/acceleration would be expected in theory when the fraction of hydrogen is increased in the flow.

For Accuraspray the response to hydrogen changes does not result in any clear behavior, for Spraywatch, the increase of hydrogen results in a decrease of particle temperature and almost no variation in particle velocity, which contradicts the notion of enthalpic increase on the stream.

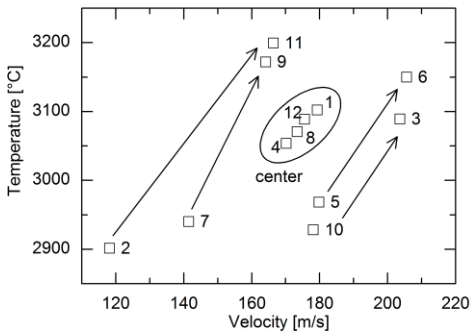

DPV2000

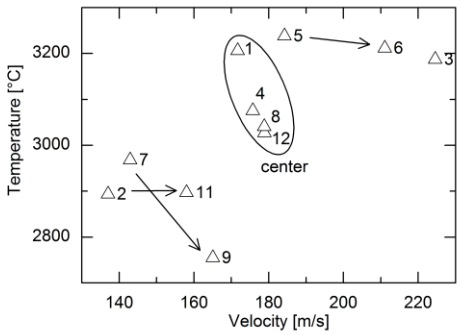

Accuraspray

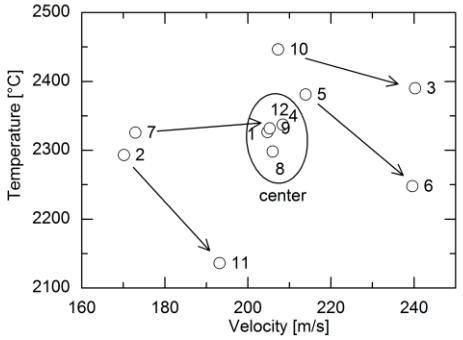

Spraywatch

Figure 25: response of different sensors to variations in torch current. Arrows indicate increase of torch current increases keeping the rest of the parameters constant

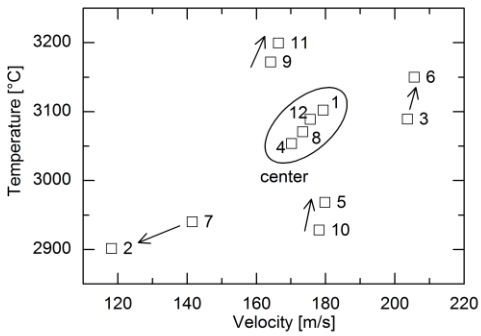

DPV2000

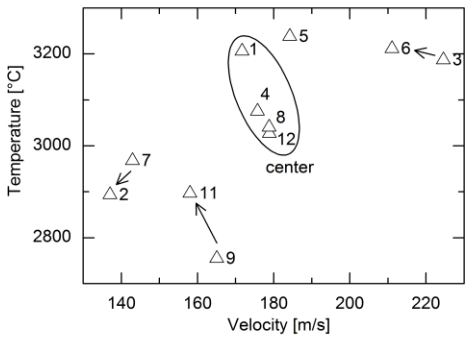

Accuraspray

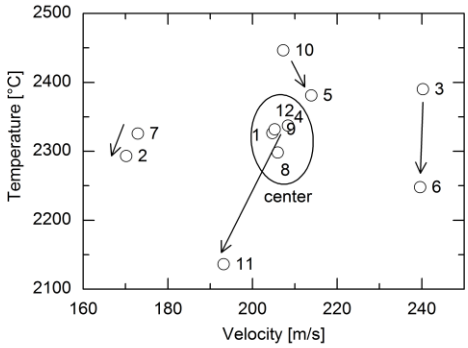

Spraywatch

Figure 26: Response of different sensors to variations in Hydrogen Fraction in the stream. Arrows indicate increase of hydrogen fraction in the stream keeping the rest of the parameters constant

3.3 Sensor Comparison for HVOF coatings

A similar approach of simultaneously measuring particle state during spraying was executed with an HVOF torch. Given the reduced amount of parameters to be controlled by this torch compared to APS, only the combustion chemistry was modified for this set of experiments, as seen in Table 3. Other parameters such as the powder carrier gas and the total flow of gases were kept constant. Since zirconium oxide has not been able to be deposited with commercial HVOF technology given its high melting point, for this series of experiments Titanium Oxide was used as the feedstock powder for spraying.

Condition	Oxygen Flow [std ft^3/hr]	Propylene Flow [std ft^3/hr]
Standard	560	124
Oxidizing	600	90
Reducing	510	180

Table 3: Gas flow variations for HVOF sensor experiments

It can be observed in Figure 27 that although the magnitudes of the measured values are significantly distinct between the sensors, the observed trends in responses are almost identical with one exception. For the temperature measurements the 3 sensors agree that the reducing flame chemistry is the hottest, the oxidizing chemistry results in the coldest particles and the standard condition produces the middle temperature levels. For velocity, all sensors agree that the oxidizing condition is the slowest. The only discrepancy is that DPV measures reducing as fastest and the ensemble sensors measure the standard condition as the one with higher particle velocity

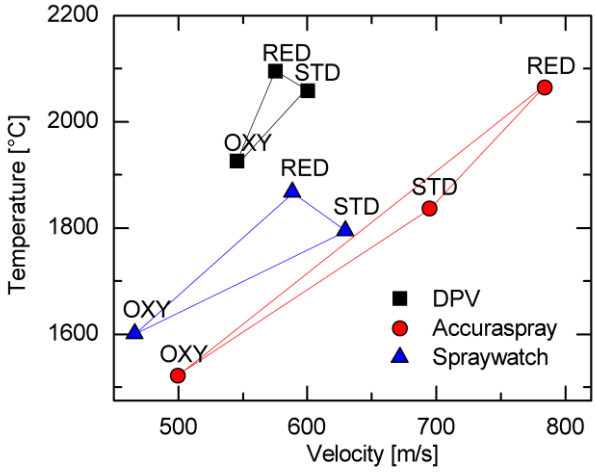

Figure 27: measured sensors responses to variations in HVOF combustion chemistry

3.4 Validation of Individual Particle measurements by the assistance of computer simulations

As a reference tool, computer simulations of selected operational conditions were also performed for the case of plasma spray with the aim of substantiating previous results assumed to be correct by the DPV2000 sensor. The simulations where performed using a Computational Fluid Dynamics code, *LAVA-3D-P*, which consists of well-verified modeling tools for plasma gas flow and particle chemistry. The model, described with detail elsewhere [114] considers the plasma jet as a compressible multi-component, turbulent and reacting flow[122]. The equations governing the simulation transport phenomena include mass continuity, momentum (Navier-Stokes), chemical species, Turbulent energy dissipation and kinetics.

Given the amount of computational time required perform the simulations, 5 selected conditions of the previous process map where chosen to be analyzed with the LAVA code. The simulated torch parameters (Table 4) keep the same numbering as the parameters used for the experimental process map of section for reference purposes. Figure 28 shows the averaged particle state resulting from the simulation, and it can be observed that the response of the system to increases in total gas flow or current is similar to the DPV measurement values shown in section 3.2. This similitude is limited to particle state trends, since the absolute values of temperature and velocity variation are wider for the case of the simulated results.

Processing parameters	Operating Conditions				
Condition Number	**2**	**3**	**4**	**10**	**11**
Argon Flow [slpm]	35	60.1	47.5	60.1	35
Hydrogen Flow [slpm]	6.5	4.4	6.0	4.4	6.5
Current [A]	450	650	550	450	650
Voltage [V]	65.3	65.3	64.3	61.8	65.7
Carrier gas (Ar) [slpm]	2.9	4.9	4.0	4.9	3.4

Table 4: Torch parameters used in LAVA simulation

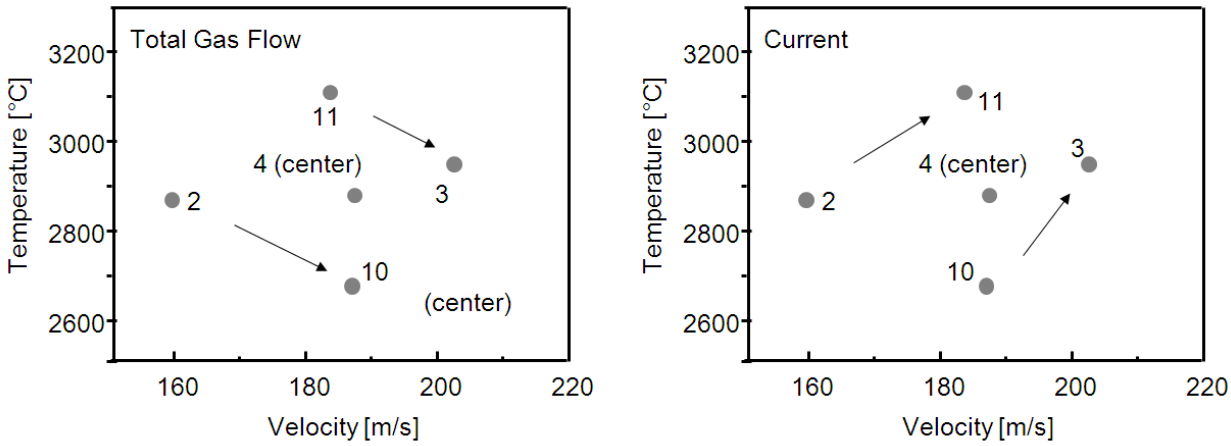

Figure 28: results of the LAVA simulated process map. , arrows indicate increases on selected parameters

3.5 Possible sources of temperature measurement inconsistencies

Two different possible causes for the particle state measurement inconsistencies between sensors are hypothesized in this manuscript, which are:

(a) The high total gas flow rate conditions, which have a lower residence time on the plasma stream and therefore should result in lower particle measurements, are too cold to be accurately detected by the sensor, giving an incorrect signal
(b) Plasma emissions are scattered from the particles to the radiation detectors, causing incorrect readings of particle temperature

Hypothesis **(a)** would mean that for HVOF case, with faster/colder particles than plasma, the inconsistencies would be even more present, which was proven wrong since the HVOF measurements show consistency among sensors

Hypothesis **(b)** would mean that for plasma spraying, the measurements are completely inaccurate and depending only on plasma emission conditions, which still doesn't explain the different trends evidenced on the sensors

Given this two contradictions a combined hypothesis is proposed combining the previous two:

(c) When the particles have a residence time in the hot zone of the plasma that is too short, thus having achieved temperatures too cold to be accurately detected by the sensors. the scattered emissions from the plasma stream start playing a role in the measurement, causing the distortions

This hypothesis is also supported by the fact that DPV is the sensor that seems to agree with the known behavior of the plasma/particles known interactions. DPV's measurement is based on individual particle measurements and has a strict data rejection algorithm to

ensure the filtering of noise during the measurement, while the other two ensemble measurement systems are measuring the whole emissions from the stream, making easier the scattering of plasma radiation into the temperature computations of the sensor.

3.6 Process Map with a tighter window of parameter variation

To support our hypothesis a different process map, with a tighter window of parameter variations was constructed, the parameters of this "smaller" process map are listed in Table 5. Note that for as an example, the current variation range is smaller, from 500 to 600 amps, while the previous process map in section 3.1 ranges from 450 to 650 amps of plasma ionization current. Similar reductions in process window apply for the rest of the parameters in this smaller DOE

Condition #	Independent DOE variables			dependent variables	
	Ar Flow [slpm]	H_2 Flow [slpm]	Current [amps]	Carrier Gas [slpm]	Voltage [V]
1	37.8	9.9	550	3.5	71.6
2	32	12.0	600	3	73.8
3	43.6	7.8	600	3.7	68.2
4	37.8	9.9	550	3.3	70.1
5	32	12.0	500	2.8	73.6
6	32	7.8	600	3	65.8
7	43.6	12.0	600	2.8	65.6
8	37.8	9.9	550	3.5	70.6
9	43.6	7.8	500	3.6	67.9
10	32	7.8	500	3	66.7
11	43.6	12.0	500	3.6	74.1
12	37.8	9.9	550	3.4	70.5

Table 5: Parameters used for the reduced parameter window process map

The results of the measurement of such a process map are shown in Figure 29 for the case of the Accuraspray ensemble sensor. It can be seen that:

- The effect of increasing the total flow is an increase on the particle velocity and a slight decrease on particle temperature
- The effect of current increase is an increase of particle temperature and a slight increase in particle velocity
- The effect of increasing hydrogen flow results in an increase of particle temperature

All this results agree with the responses of the DPV individual particle sensor shown in section 3.2 of this chapter and follow the accepted behavior of a AC plasma spray system

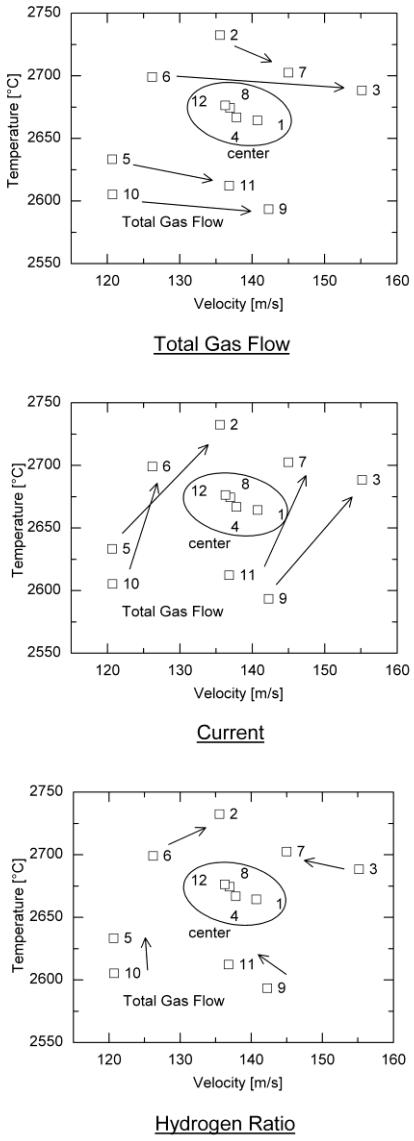

Figure 29: results of the reduced window of variation process map measured with accuraspray, with parameter effect indications

3.7 Repeated Measurements with constant particle state

In the earlier sections of this chapter we analyzed the response of particle state sensors to process parameter modifications, in this section we will concentrate in analyzing the response of the systems to a constant torch state and measure the overall variability of the sensor measurements.

The approach for reaching "constant" plume conditions was to perform multiple measurements with different sensors in the same run. This should have avoided plume conditions associated with an arc attachment location change that are known to be enhanced by the re-starting of the torch. The length of the current run was of 2 hours approximately with some cathode/anode wear is expected to have occurred but not in a rate significantly enough to compromise the experiments.

10 measurements were performed with each sensor (DPV, Accuraspray, Spraywatch) constantly alternating between them, without changing the plasma torch parameters. The parameters used correspond to the center condition of the first order process map, or condition 1 of Table 2. All measurements were also performed without changes on the sensor settings.

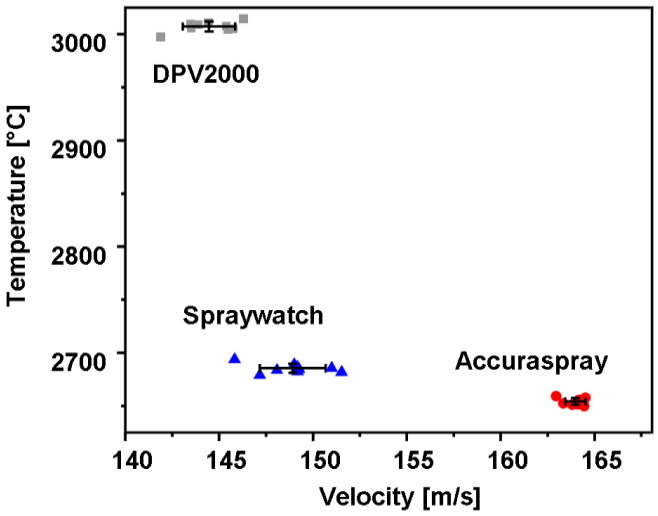

Figure 30: Mean and Range of Different Sensors for Repeated Particle State Measurements

Resulting particle states are represented in Figure 30, with the center of the standard deviation error bars for each sensor being the average value of the 10 measurements and the different measurements depicted in combination with the error bards. From this graph it can be observed that the absolute value of the different sensors is completely different as expected from previous experiments, but it can also be noticed that the sensors are fairly consistent with DPV having the largest standard deviation of temperature (≈5 °C) and Spraywatch the largest standard deviation for velocity (≈2 m/s). The range of measurement s is about 3 times the standard deviation for all the sensors. This experiment suggest that although the responses to process variations in the sensors might not be necessarily accurate, they still can be a useful tool for measuring levels of variation from a pre-set range, these measurements could be accurately used for making go/no-go decisions before performing a spray run. In the following section an approach for achieving similar particle states is executed to compare the different sensors responses.

3.8 Response of different sensors to algorithms for constant particle state achievement

This series of experiments was aimed and comparing the response of the sensors to supposedly similar temperature and velocities achieved with different torch parameters. Three APS different runs were performed with three different hydrogen flow rates. Argon flow and current flows were sequentially adjusted by the use of an algorithm first introduced by Srinivasan et al.[123] and described elsewhere[124]. The algorithm uses the data from the first order process map (such as the one described in section 3.1 of this manuscript) to approximate the responses of the particle to process parameters change, re-adjusting the parameters until the temperature and velocity converge to desired range. For these experiments all the calculations required were performed with particle data provided by DPV, Simultaneous measurements were performed with Accuraspray and Spraywatch.

It must be noted that such algorithm is a preliminary method based in linearization of particle states to process parameter variations, and given the stochastic nature of the thermal spray process does not always result in a convergent pathway for particle T&V tuning. The number of steps to converge in the desired temperature and velocity range varies widely, for this series of experiments it ranged from 3 to 5 steps. The different parameters for the different run conditions are summarized in Table 5. It should also be noted that the carrier gas flow rate was adjusted to achieve a constant plume depth.

Figure 31 shows the results of the particle state algorithm experiment with different sensors, for DPV it can be seen that results follow a series of steps, with some times contradicting responses until reaching a same T-V area depicted with an ellipse. For the remaining two sensors, although the directions of the temperature and velocity vectors were different and the magnitude of the measured values the same behavior is observed: the particle state converged into a narrower limit than the spread of the complete steps T-V area. In different words, although the vectors and values were different, all three sensors agree that the final steps had closer temperature and velocities. This conclusion evidences the applicability of particle state sensors assess the repeatability of particle state before performing a coating run.

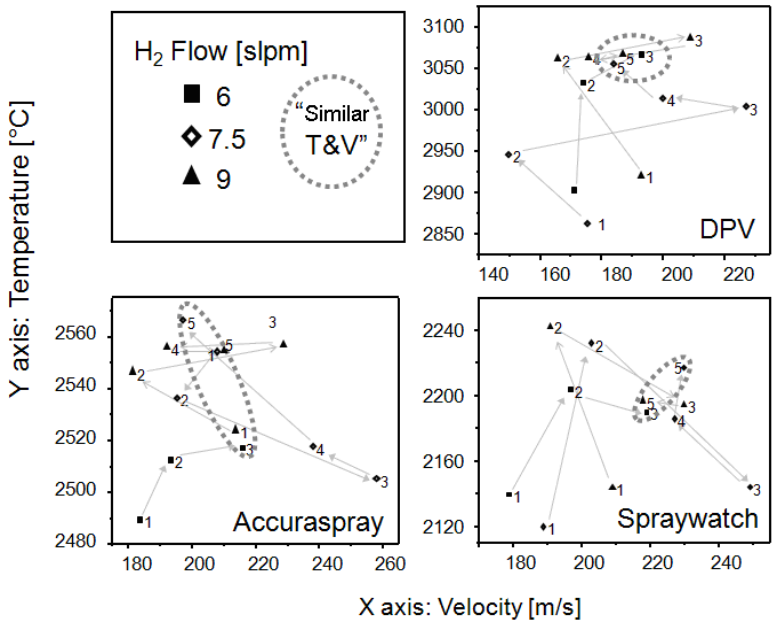

Figure 31: State of Similar Temperature &Velocity algorithm experiment as measured with different sensors

3.9 Particle injection visualization salient observations

3.9.1 Injection optimization-APS

The existence of a optimum injection penetration depth for APS external radial injection was first suggested by [125] and proven by researchers at Stony Brook [83] who developed a systematic procedure for finding the optimum plume depth or *sweetspot* of injection. Subsequently, each time the torch is initiated to produce coatings the carrier gas should be adjusted to match the sweetspot, instead of keeping the carrier gas constant amongst runs, which is the industrial practice for carrier selection.

Srinivasan et al [83] also indicated that such plume position or *sweetspot* is independent from process parameters, that is, the plume depth should be kept constant independently of the gas flows applied or the torch current/voltage settings. This premise was followed in the previous section regarding process map development, where the same plume depth was kept constant for all sprayed conditions and the carrier gas was considered a dependent variable.

Srinivasan et al [83] analyzed the *sweetspot* relation to other variables, such as feedrate, spray distance, even injector position and it was found that the *sweetspot* is independent of them. Their work does not explain whatsoever which is the exact explanation for the existence of this optimal depth other than being the location of "effective thermal and momentum transport"

In order to understand better the interaction between the particles and the plasma stream the highwatch/spraywatch sensor setup (explained in detail in the the experimental techniques section) was used for injection monitoring, while accuraspray was used for monitoring plume depth and ensemble particle temperature. A standard injection optimization run was performed as described by Srinivasan[83] where the carrier gas flow was varied between 3 and 5 slpm in intervals of 0.5 slpm. All the other conditions of the experiment where kept constant.

From Figure 32 it can be observed that the particle temperature followed a parabolic response to plume penetration depth, with a peak in around 9.5 mm depth (4 slpm carrier for this particular run). The spraywatch collected images show the different particle trajectories interacting with the plasma stream that can be summarized as follows:

- Image A: with a low carrier gas (3 slpm) resulting in the lowest particle temperature shows the particles penetration path to be cross the hot/brightest zone of the plasma more than halfway of the picture downstream from the plasma nozzle
- Image B: with 4 slpm of carrier gas and the optimum particle temperature, shows the particles penetrating the plasma upstream in comparison with image a, and the particles flowing almost in parallel to the hot zone of the plasma
- Image C: with 5 slpm of carrier and a decreased particle temperature, indicates particles penetrating the plasma similarly to figure A, with the exception that some of the particle flow crosses the plasma hot zone completely, while for Image B the particles stay in the plasma hot zone path

From this observations we can infer that the existence of the injection sweetspot is actually dependant on the trajectory of interaction of the particles with the plasma stream, if the injection momentum –given by the carrier gas flow- is too weak, the particles will not penetrate the plasma in its hottest zone (by the nozzle exit). In the opposite case, if the particle's momentum is too high, some particles might cross the plasma, not residing in the hot zone for the optimum time period.

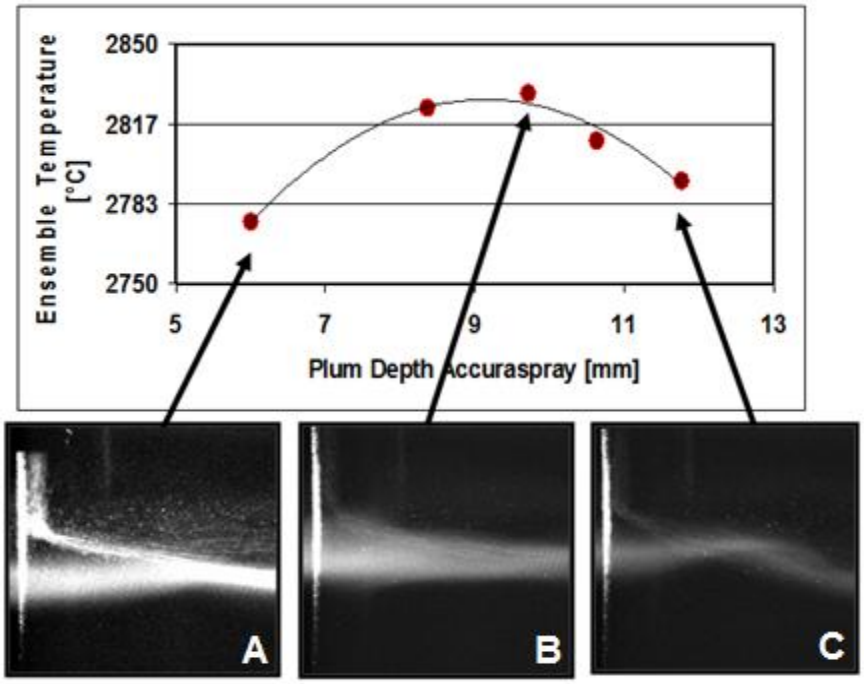

Figure 32: Particle Temeprature Optimization and its relation with Spraywatch injection images

This conclusion also explains the independence of this geometric variations to other plasma parameters such as gas flow or current/voltage variations. The hot zone location will always be the same, at the exit of the nozzle. The amount of carrier/momentum needed to penetrate the plasma without crossing it might change given other torch parameters, but the geometric location of this interaction is invariable, that is why Srinivasan et al found the same optimum plume depth penetration in spite of having to select "different carrier gas flow rates for different primary gas flows" during optimization

3.9.2 Quality problems with particle feeding

Another interesting application for particle image visualization found during the application of process maps for different material systems is the ability to access problems in particle/plume interaction, such as powders that are too fine to penetrate the plume, accumulation of material in the injector or torch nozzle. Figure 33 shows the injection of two different powders: Image A, a commercial grade YSZ powder flowing normally into the plasma plume and Image B, an experimental cut of cobalt-ferrite powder that was too fine for the particles momentum to counteract the plasma stream and penetrate the plume. From Figure 33-B it can be observed that the poorly injected powder formed a "cloud" of powder that did not penetrate the spray plume.

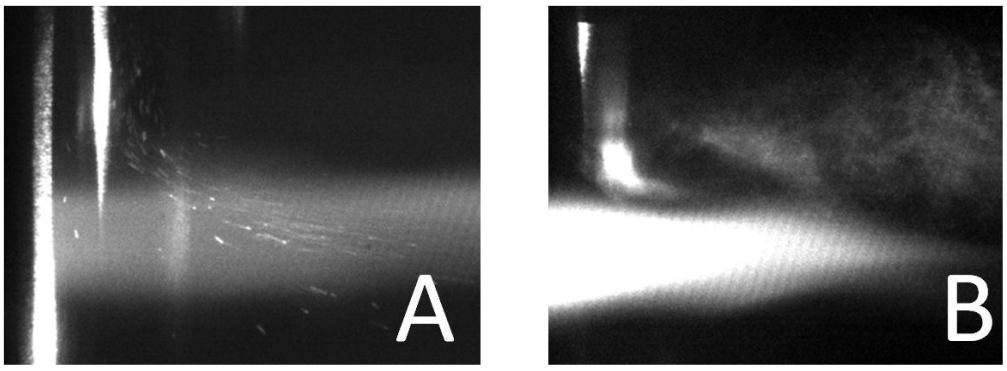

Figure 33: Visualization of Injection quality

3.9.3 HVOF shock-wave diamonds

One of High Velocity Oxygen Fuel's thermal spray methods intrinsic characteristic is that the gas flow Mach number is higher than 1. With the gas stream flowing so fast, the pressure of the gas is considerable lower than atmospheric, and after exiting the converging-diverging nozzle of the torch the pressure progressively stabilizes to the atmospheric pressure by a series of adjustment oblique shock and expansion waves called *shock diamonds*[126].The presence of these shock diamonds and their characteristic is related to energy losses in the stream, to the point that some authors suggest that a lengthened transonic region in the flame might result in faster particle states [127]

For this part of the study, the combustion chemistry of the HV2000 HVOF torch was modified with the same parameters shown in Table 3 of this manuscript, and the spray watch camera was used to take pictures of the stream at the exit of the nozzle. The shock diamonds can be visualized in Figure 34. The images were edited to indicate the center of the diamonds (red marker). With a detailed look it can be observed that the distance between diamonds is variable between the different combustion chemistries, the distance between diamonds for the stoichiometric flame is marked -d- on the image and placed for reference in the other two flames. It can be observed that for the reducing flame the distance between diamonds is actually longer than for the stoichiometric flame, and for the oxidizing case the distance between diamonds is closer.

This observation agrees with the measurements performed by accuraspray in section 3.3, on which the fastest/hottest condition corresponds to the reducing flame, this could be explained by the lesser loss of kinetic energy in the diamonds and a longer flame distance (the lack of oxygen extends the combustion longer in the stream, increasing the dwell time of the particle in the burning zone) a corollary to this observation could be that measuring the distance between diamonds could be applied as a technique to access the repeatability of the flame in industry. Making sure the interaction among gasses is the same before each spray run.

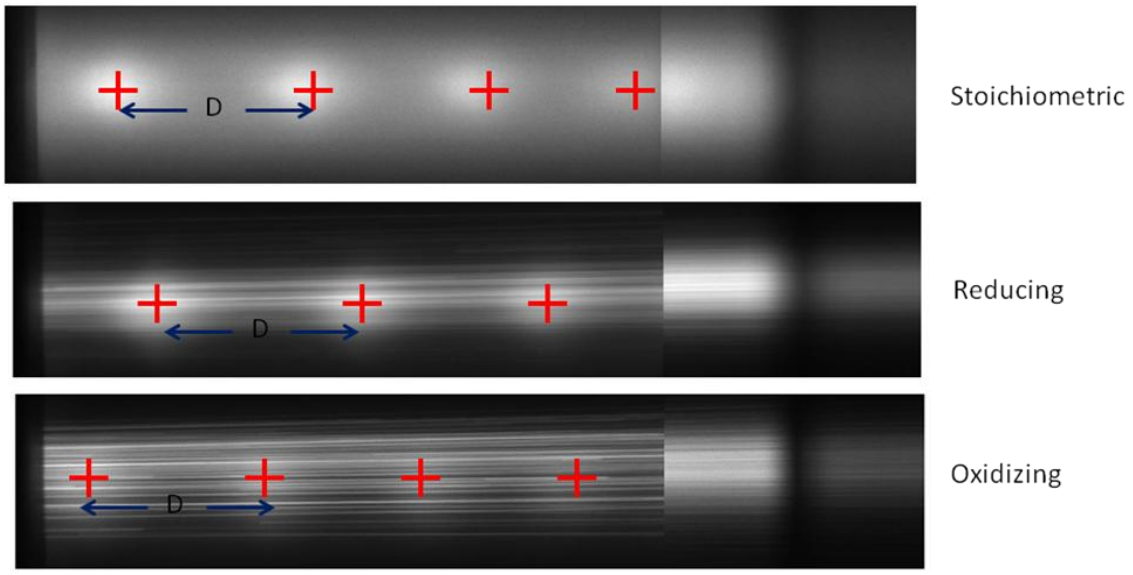

Figure 34: HVOF flame stream at the exit of the spray nozzle for different combustion chemistries. (Note: no particles were flowing in the Stoichiometric flame)

3.9.4 Flame Spray particle interaction observation

Low Velocity Combustion Spray is the oldest of the thermal spray methods, given its simplicity and its "low tech" approach to melt and deposit particles it has been relegated by most researchers who consider the quality of the coatings poor and too porous. Nevertheless, flame spray is still a technologically important thermal spray technique since it has low investment and operating costs. It lacks the need for extra safety precautions for high noise levels or ultra-violet radiation, so in applications where a high density coating is not needed flame spray can achieve the coating needs with a much lower cost than its advanced APS or HVOF counterparts.

Most of the work on flame sprayed coating has been focused in coating properties such phase formation and microstructure[48] etc. Since the advent of the particle state sensors research has only been performed to compare flame spray to other coating process[128] but no literature detailing process-property relationship study has been published to compare particle state with process parameters, this section aims contribute in this knowledge gap by performing a first order process map of alumina 1% chromia coatings and observing the particle/flame interactions at the nozzle exit with the use of the spraywatch camera.

For this first order process map the flow of carrier gas (9 slpm) and the federate of powder (15 gr/min) were kept constant and the only two parameters modified where the flow of oxygen and fuel (Acetylene). The result of the DPV measured first order process map can be observed in Figure 35 , it can be seen that the two conditions with equal flows of oxygen and fuel result in the highest particle temperature, while the two conditions with offset of gas flows result in a lower particle temperature. The velocity

seems to be a function of total flow of gasses, as the particles velocity order follows the same trend as the sum of oxygen+fuel flows.

It must be noted that a relationship of 1 slpm of oxygen flow to 1 slpm of fuel flow does not mean a stoichiometric flame but a reducing chemistry, given that the equation of the combustion of acetylene; $2C_2H_2 + 5O_2 => 4CO_2 + 2H_2O$; a ratio of 2.5 slpm of oxygen per slpm of acetylene would be needed for a stoichiometric flame. Still is inferred that an equal flow of gasses ensures an evenly mixed stream resulting in the most energy liberated.

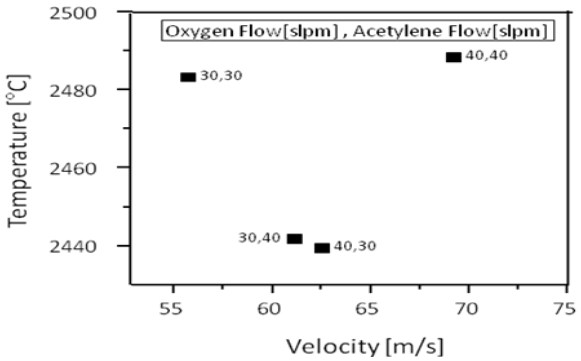

Figure 35: first order process map of Al_2O_3 + 1%Cr_2O_3 for a Therodyn flame spray torch

The spraywatch captured images (Figure 36) can provide some insight into the interaction of the Al_2O_3 + 1%Cr_2O_3 particles with the oxy-acetylene flame. The lowest total gas flow condition (30/30) with stoichiometric flame and the excess oxygen condition result in a wider flame. While the high total gas flow (40/40) stoichiometric flame and excess fuel conditions result in a narrower particle/flame stream. The width of the flame does not seem to have a direct correlation with particle temperature or velocity since the wider flame images cannot be separated in any particular particle state category from their narrower counterparts, this shows that particle state is more dependent on flame input parameters that the visible interaction of the particles with the flame at the nozzle exit.

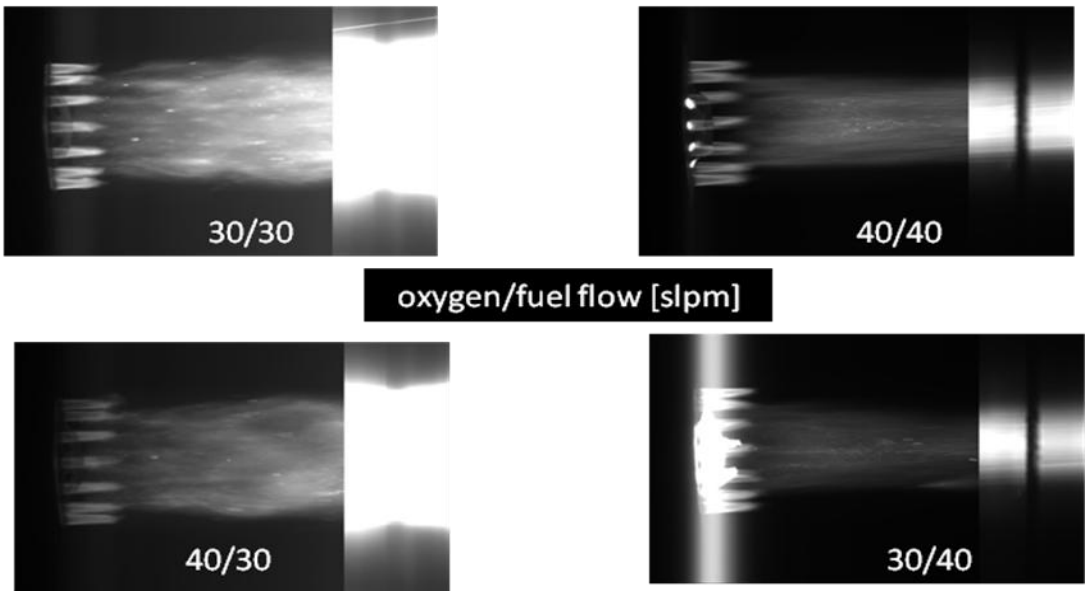

Figure 36: observation of flame spray interaction with particles for different flame chemistries

3.10 Image Particle Velocimetry and the effect of capturing parameters on the sensor reading

Particle state sensing techniques fundamental principles where described in section 2.2 experimental methods description. Nevertheless each sensor has individual capturing parameters with the aim of optimizing the detection process, filtering unwanted noise and increasing the precision of the measurements

For the case of DPV, there are 13 "rejection"[129] criteria for the two wavelength detector signal to be filtered, but the level of sensitivity to which this rejection criteria is applied can be modified, this level of sensitivity or "trigger level" is kept constant during measurements and during the collection of a complete process map data.

For the case of Accuraspray, the sensor capturing parameters are related to the signal amplification of the detector and the shutter speed parameters, these parameters will also affect the sensitivity or precision of the sensor. Accuraspray , additional to the stream characteristics outputs an statistical parameter denominated "correlation" which is an indicator of how similar the signals of the two CCD detectors are as a function of time. This correlation indicator is an useful tool to access the precision level of the measurements performed, in the process map of section 3.2 where accuraspray was shown to output the wrong temperature trends at high gas flow conditions the correlation indicator was relatively low: 0.7, with 1 meaning a completely identical two wavelength detector signals and 0 being completely different. Another important parameter for accuraspray sensor is the *intensity* of the plume. This intensity should not be confused with the two-wavelenght pyrometry radiation intensity; the *plume intensity* is a measure

of the image analysis of the video signal of the sensor that follows plume penetration geometry. Plume intensity is controlled by the brightness of such video signal.

For Spraywatch, the parameters are related to the operation of the camera, given its approach of using particle image velocimetry and two wavelength pyrometry in the same CCD camera detector. Exposure time for both the velocity and the temperature measurement can be modified independently, also signal gain and camera aperture. Spraywatch is different from Accuraspray and DPV in the sense that these parameters can be set in an "automatic" mode, to which the sensor constantly changes the parameters using an algorithm to optimize the quality of the sensor output.

If these settings are left in auto, particle state monitoring would be done with different parameters for different process conditions. A process map with the same parameters as the one in section 3.1 was performed using spraywatch before the results shown in Figure 24 were measured. In the first trial the camera's parameters where left fluctuating in automatic setting mode with the results show in Figure 37, subsequently the same process map was repeated, but with parameters such as exposure time, gain and camera aperture kept constant through the whole experiment, the results –which are the same as Figure 24- are also shown in Figure 37 for comparison

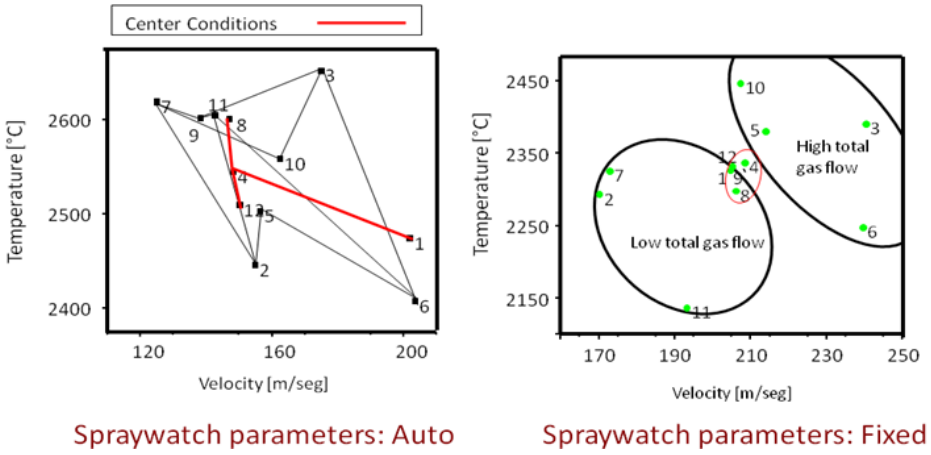

Figure 37: Spraywatch measurement with different approaches to camera settings

It can be observed that for Spraywatch, if the parameters are left in the self adjusting or "auto" mode, the measurements are non consistent and not showing any particular trend or behavior. Even conditions 1, 4, 8 and 10, which are the same parameters (center condition of the DOE) the measurements are significantly different. In the second case, if the parameters are left fixed during the whole experiment a trend is observed and the center condition remains in similar T-V locations. This experiment indicates that although the equations governing two-wavelength pyrometry are based in the ratio of intensity of emissions in two different wavelengths [130], theoretically independent of the

exposure time or the detector's intensity amplification, changing such parameters will have a detrimental effect on the consistency of the measurements.

3.11 Conclusion

Particle state sensors based on two-wavelength pyrometry are an insightful tool for assessing in-flight melting state and kinetic energy of the particles but their data should always be interpreted with care cross-comparing with the understood behavior of thermal spray systems as inconsistencies in measurements were found for certain conditions an sensors. When measuring process that have high emissions from the torch flame such as plasma spray with high particle speed and lower particle temperatures caution must be exercised when interpreting data from ensemble two-wavelength sensors as depicted in Figure 38

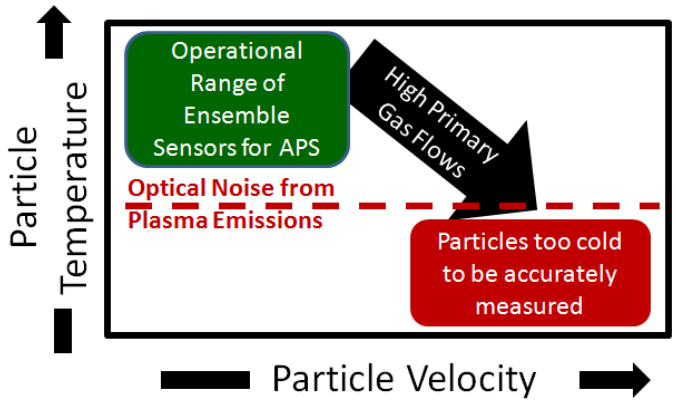

Figure 38: Threshold of Plasma Emission Distortions on Ensemble Two-Wavelength Pyrometry

Diverse applications of injection visualization techniques demonstrated the potential for process monitoring and optimization in both axial and radial injection settings for combustion and plasma equipment.

Chapter 4. Process Mapping of Titanium Dioxide Coatings, implications of processing techniques on rapid solidification phenomena

The mechanisms that control the rapid solidification and coating buildup have been extensively studied by numerous researchers to access the factors controlling microstructural formation, phase evolution, mechanical properties and a wide range of functional characteristics of thermally coatings. These studies usually focused either on individual splat studies or standard coating processing and are typically developed with the use of one specific spray system. Usually parameter manipulation experimental designs are applied to observe the effect of specific process changes on the characteristic of interest.

The present chapter aims to clarify mechanisms on rapid solidification phenomena related to microstructure, phase content, stoichiometry and functional properties of Titanium Dioxide integrating different thermal spray techniques and property evaluation procedures. Focusing in different hardware and parameter variations allowed us to explore an unusually wide range of processing conditions and particle states that allowed us to make solid observations that not only apply to the Titanium Dioxide system but also to the field of thermal spray process science.

All coatings in this study were produced by using a commercially available powder, *Neoxid* 1028 IS40 (*Millidyne Oy*, Tampere, Finland), an agglomerated and sintered powder with a purity grade of 99.8% with a mean particle size of 16 micrometers (data reported by the manufacturer) The impurities present consist mainly of Iron Oxide of less than 30 ppm, Aluminum Oxide and Silicon Oxide are also present in less than 0.1% weight. According to X-ray diffraction studies, the phase composition of the feedstock powder was mainly anatase, with the rutile content being less than 4% by volume. The powder was sintered at a temperature close to 900 °C with a short holding time to prevent the anatase to rutile transformation.

4.1 Deliberate Manipulation of Particle State by change of process parameters and hardware

Two industrial thermal spray techniques where considered for this study, APS and HVOF since they operate in different regimes, significantly differentiating the characteristics of the obtained coatings . Different combinations of gas flows where considered for both processes (and current for APS) with the powder injection geometry maintained constant for APS spray as explained in section 3.9.1 of this manuscript.

Hardware effects where manipulated in APS by changing nozzle diameter of the *Plasma Technik F4* commercial plasma spray torch (*Sulzer Metco, Westbury, NY*) since the nozzle diameter will have a direct influence on effluent gas velocities, affecting the particle velocity and its residence time in the hottest zones of the plasma[132]. Hardware manipulation for the HVOF process was achieved by the operation of two types of commercial HVOF torches. The first, *Diamond Jet* (*Sulzer Metco*), with a mixture of hydrogen fuel, oxygen and air as flow gases. The second, *HV2000* (Thermach, Appleton WI), employs a mixture of propylene and oxygen as fuel gases, eliminating the heat absorption by the nitrogen in the air, thus resulting in higher particle temperatures. The torch parameters applied for this section of the study can be observed in . It is important to emphasize again (as in section 3.1) that the parameters modified in this study are far from being the only parameters that control the coating rapid formation mechanisms. Instead, the aforementioned torch parameters are key in defining in-flight particle state, the central focus of study of this chapter of the dissertation.

Condition	Torch Hardware	Argon Flow [slpm	Hydrogen Flow [slpm]	Current [amps]	Powder Feed Rate [g/min]	Carrier gas [slpm]	Fuel Type and Flow [slpm]	Oxygen Flow [slpm]	Air Flow [slpm]
1	APS – F4 8mm Nozzle	47.5	6	550	21	3.9	-	-	-
2	APS – F4 8mm Nozzle	35	1	450	21	3.3	-	-	-
3	APS – F4 8mm Nozzle	60	2	450	21	4.2	-	-	-
4	APS – F4 5mm Nozzle	47.5	6	550	21	6	-	-	-
5	APS – F4 5mm Nozzle	35	1	450	21	4.5	-	-	-
6	APS – F4 5mm Nozzle	60	2	450	21	7	-	-	-
7	HVOF – HV2000	-	-	-	15	10	C_3H_6: 83	240	-
8	HVOF – HV2000	-	-	-	15	10	C_3H_6: 42	283	-
9	HVOF – Diamond Jet	-	-	-	15	15	H_2: 563	222	341

Table 6: Torch Parameters for Extended TiO_2 First Order Process Map

Figure 39 shows the response of the particle state (represented as average temperatures and velocities) as a function of process type, torch, torch geometry and spray parameters. This expanded *first order process map* indicates known responses of process variations, such as the 5 mm nozzle resulting in higher velocities than the 8 mm for the case of APS, although the decreases in temperature were not very significant. It is clear that the higher current conditions (1 and 4) resulted in higher particle temperatures. In the remaining low current conditions the higher argon total gas flow conditions (6 and 3) yielded higher velocities than for the low gas flow conditions (2 and 5) but not necessarily lower temperatures.

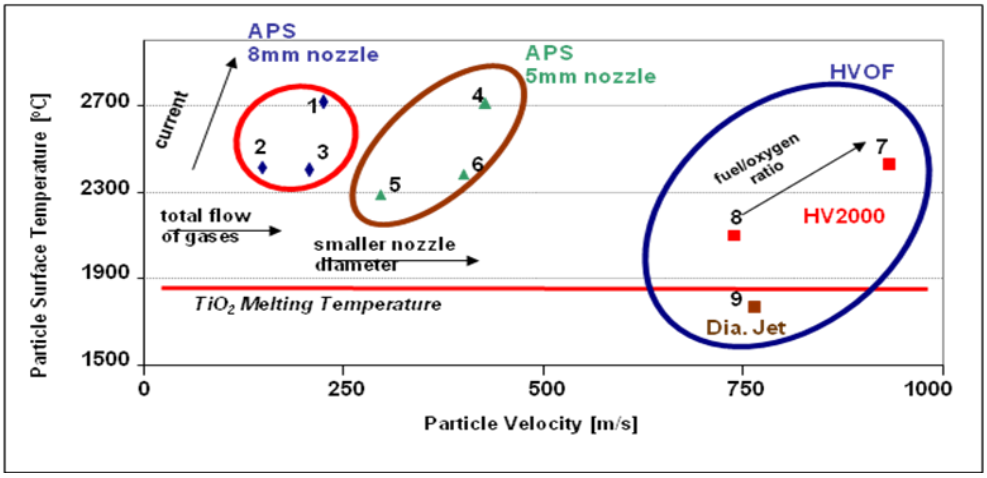

Figure 39: Expanded first order process map agglomerated and sintered TiO_2

In the case of HVOF spraying, the HV2000 torch resulted in a significantly higher melting particle state, being the condition 7 (reducing gas mixture), the condition with higher particle temperature and velocity. The Diamond Jet spray, even with the use of a higher enthalpy fuel (H_2) proved unsuitable for the spraying of ceramic materials. It must be mentioned that even though the particle temperature is below the melting point of TiO_2 the reported values constitute averages of a distribution of particle temperatures. As a result a portion of the Diamond Jet sprayed particles will be molten or partially molten enabling formation of a coating. Particle Temperature Histograms for conditions 1-8 constructed from individual particle data provided by the DPV2000 sensor in Figure 40 are a clear indicator that although the mean values of particle temperature are easily distinguishable in Figure 39, there is a significant overlapping of individual particle states between the different process conditions.

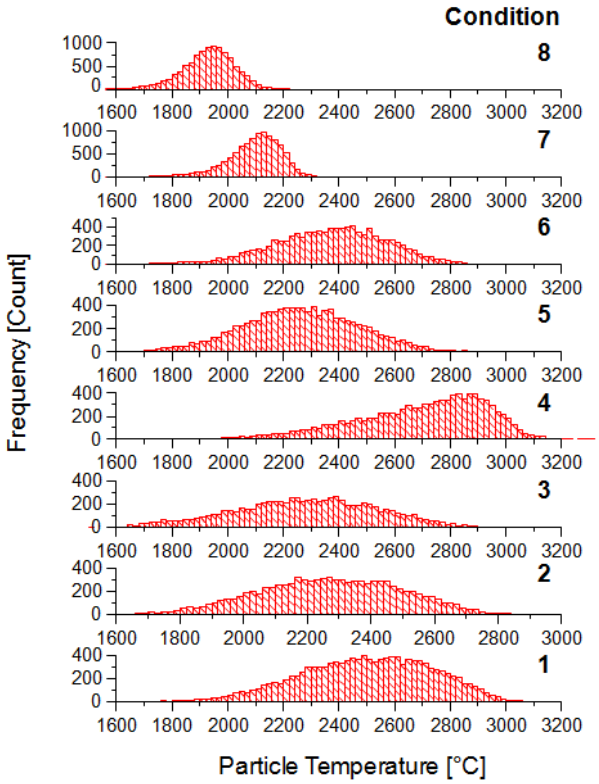

Figure 40: Particle Temperature Distributions for Extended 1st order process map

4.2 Effect of particle state on coating microstructure and porosity

Microstructural characterization is the most common method applied in the industry to asses coating quality and characteristics. Although its application can be limited since it does not consider the quality of the intersplat boding and other non-visualizable characteristics, it is still a powerful tool to analyze differences in coating formation[133]. Observable characteristics such as porosity (ratio of the coating volume not filled by the feedstock material) have been previously linked to mechanical properties such as young modulus[134] or transport properties such as thermal conductivity[105] of thermally sprayed materials.

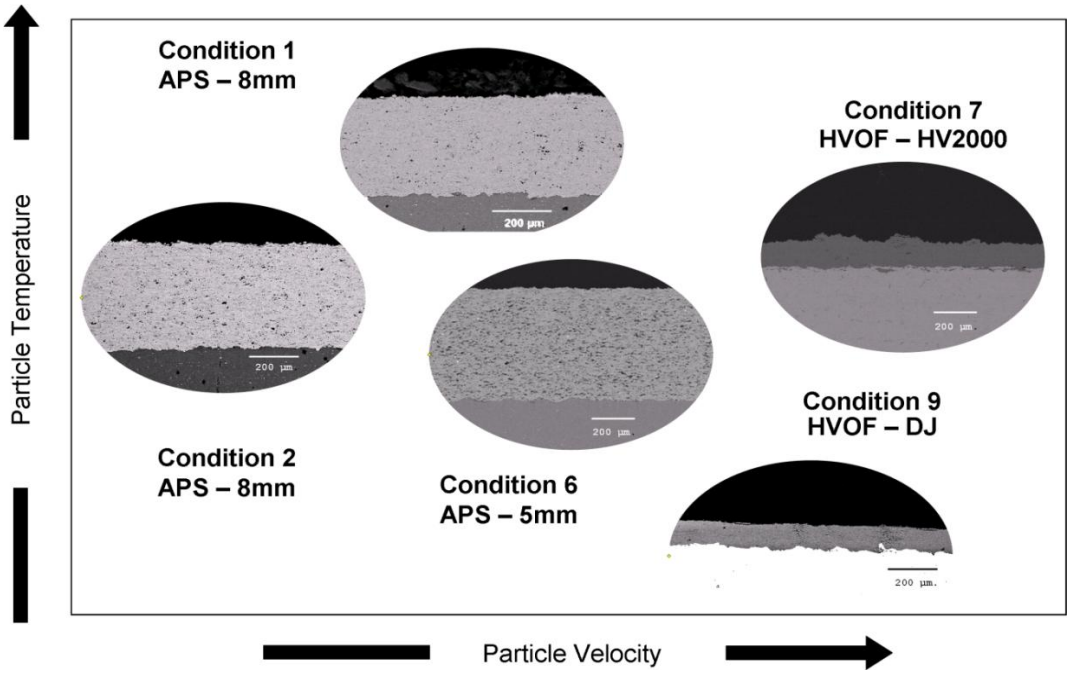

Figure 41: Selected Microstructures of TiO_2 extended process map (low magnification)

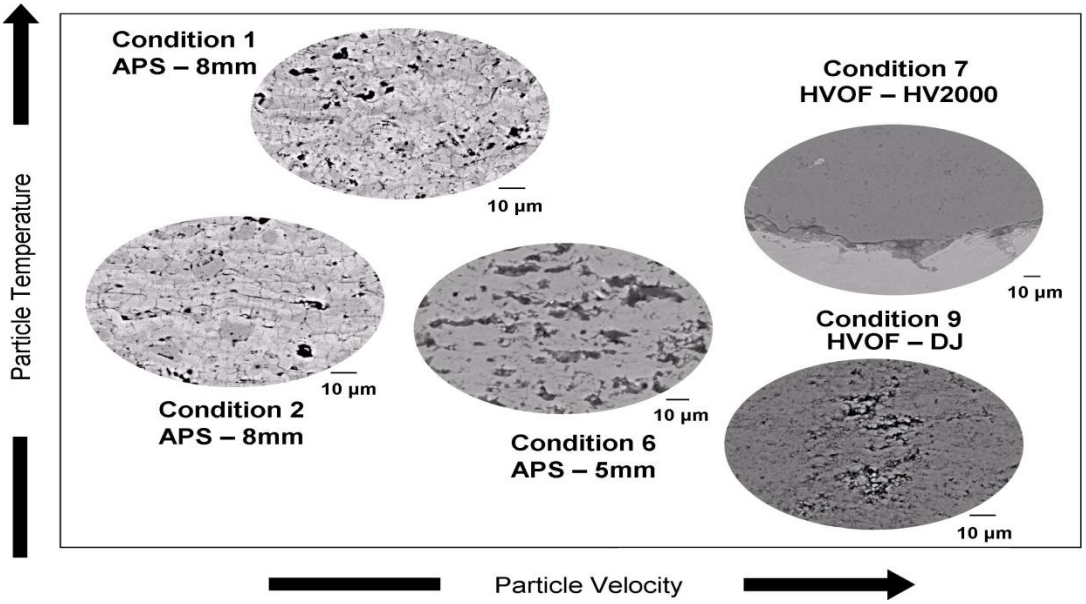

Figure 42: Selected Microstructures of TiO_2 extended process map (high magnification)

Figure 41 and Figure 42 present cross-section microstructures of coatings deposited under different conditions. For clarity, the images are relatively overlaid on the 1st order process map. Figure 43 presents quantitative values of porosity obtained by image analysis of the SEM micrographs in a second order process map. Several important observations can be made from looking at any of the 3 images:

- For the case of plasma spray, as the velocity increases and temperature decreases, the coating shows an increased porosity content, as shown through the comparison between condition 1 and condition 6. With an Increase of both Velocity and Temperature the opposite effect is found.

- The *HV2000* sprayed coatings of significantly higher velocities show excellent density despite somewhat lower particle temperatures than APS. This is not surprising since the operative mechanisms of deposit formation are different for the plasma and HVOF spray processes including ceramic materials[70].

- The *Diamond Jet* HVOF sprayed coating resulted in lower porosity levels than most APS coatings by image analysis, but it is clear from the micrographs (Figure 41, Figure 42) that the microstructure is highly defective and results in poorly bonded splats. As seen from the 1st order map (Figure 39) the average particle temperature was below the melting point of the TiO_2.

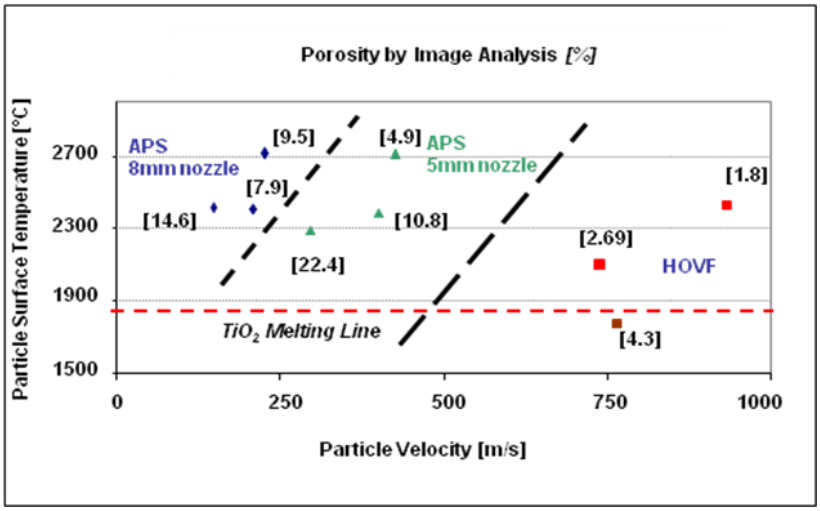

Figure 43: second order process map of coating porosity

4.3 Effect of particle state on coating phase evolution

Figure 44 overlays the quantitative phase distribution of the TiO_2 coatings with respect to the 1st order process map location (second order process map). In general, the results indicate that the coating contained somewhere between 17 to 40% anatase. Furthermore it is clear that in general, the anatase content increases as the particle velocity increases suggesting that higher impact velocities can result in generating anatase phase. Moving up along the temperature axis also appears to result in higher anatase content as is seen for all three operational regimes (8 mm nozzle, 5 mm nozzle and HVOF). The diamond

jet coating with lowest temperature and melt content resulted in very little anatase in the coating.

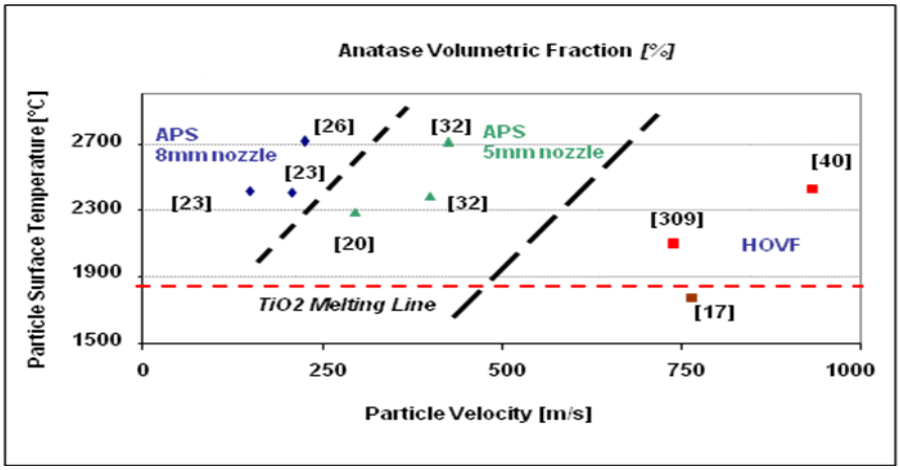

Figure 44: Second Order Process Map of TiO_2 Phase Content

It can be observed that for HVOF, a higher anatase fraction was found for condition 7, with the higher particle velocity and the higher particle temperature. The lowest anatase fraction was found in the highly defective DJ sprayed condition 9. This result contradicts the assumption of anatase being the result of unmolten particles. It can also be seen that for the two processes, the condition with the highest particle temperature and velocity results in the most anatase content- condition 1 for APS-8mm, 4 for APS-5mm and 7 for HVOF -This results agrees with the theory that the higher solidification rates will promote anatase content[33]. This can be explained by the fact that high temperatures will promote the complete melting of the feedstock and particle velocity at impact is expected to influence the thickness of the splats, which also is known to have an effect on the cooling rates of the particles[135] . In fact, particles with higher Reynolds numbers at impact (i.e. higher velocities and temperatures) will spread wider resulting in lower splat thicknesses[136] which in turn will translate into higher splat cooling rates[3]. This is in agreement with a higher content of metastable phase in the high velocity and temperature droplets. It is also observed that the conditions with the lowest temperature and velocity combinations for each process resulted in the lowest anatase content (3 for APS-8mm, 5 for APS-5mm and 9 for HVOF)

The phase evolution in the TiO_2 system has been a subject of intense investigation in recent years([25, 28-30, 137-139] among many others). The literature in thermal sprayed TiO_2 situations is much more ambiguous in terms of the observed phases. A number of competing aspects play a role in the preferential emergence of the phases. In our study, the starting feedstock powder was all anatase but the resultant coatings were both anatase

and rutile. Several scenarios can be considered in explaining these phase evolution mechanisms .

- Particles that are melted and deposited can exhibit either rutile or anatase depending the extent of undercooling during solidification. Li and Ishigaki [33] have rationalized that TiO_2 resulting from equilibrium solidification will favor rutile, while anatase nucleation may be favored in enhanced undercooling scenarios. However, it has also been reported that flame or plasma synthesized TiO_2 powders can result in mixtures of anatase and rutile due to partial solidification events and possible recalescence effects.

- During thermal spray TiO_2 splat quenching, the extent of undercooling is perhaps large and as such should favor anatase retention. This is, to a certain extent, validated in Figure 8 which indicates that as the impact velocities are increased, the anatase content is increased, resulting from enhanced flattening/solidification rates and thus increased propensity for high undercooling.

- A secondary effect perhaps prevalent in thermal sprayed coatings is the entrapment of unmelted or resolidified powders which can produce either rutile or anatase. The possibility of latent heat of solidification emitted by subsequent splat impact in promoting anatase to rutile transformation cannot be discarded, as it has been observed in other ceramics systems for thermal spray that subsequent impact of splats can result in phase transformation.

- Another possible effect would be on individual particle sizes influencing the phase evolution of the splat, this effect has been suggested by Jung et al.[140] in work related to solidification of thermally sprayed particles on water, where the cooling rates are significally different from the impact on surface mechanisms of this work.

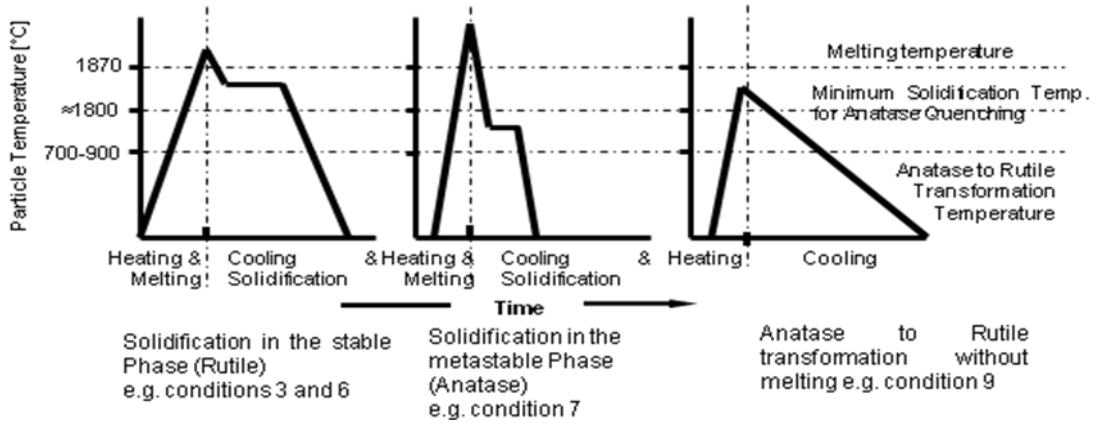

Figure 45: Possible mechanisms for TiO2 splat phase evolution, all scenarios will be present in all conditions, but presented here indicate prevalence phase in particles for each condition

We have proposed herewith a preliminary illustration of a temperature – time transformation diagram that can support the formation of either rutile or anatase formation in the thermal sprayed case. Figure 9 is an illustrative event diagram based on the transformation scenarios proposed by Li and Ishigaki[33]. These results provide a framework for consideration in thermal spray where the coating phase is highly sensitive to spray parameters and deposition conditions. Ultimately, both the thermodynamic drivers and kinetic aspects have to be considered in these high cooling rate situations. One clear strategy to assess the role of undercooling is to isolate single splats of sprayed droplets and conduct microfocus spectroscopic experiments, results of this strategy are presented in section 4.4 of this manuscript

4.4 Raman Microspectroscopy of Individual Splats, understanding paths for phase evolution mechanisms

Splats are the fundamental building blocks of thermal spray coatings, the individual mechanisms of melting, solidification, impact, flattening and bonding will define the characteristics of the system. By understanding the mechanisms that control the phase content of individual splats we can validate or void conclusions made in earlier stages of this work. To analyze phase content of individual splats, and even phase content variations amongst a single TiO_2 splats a spectroscopic technique with a very a small enough beam size ($\approx$ 1 μm^2) was required. For this size limitations both x-ray Microdiffraction and Raman Microspectroscopy would be suitable, but Raman presents a much faster rendering time and ease of beam focus, although the data presented will not be able to detail additional information on residual stress of splats available from x-ray microdiffraction .

In this series of experiments a series of individual splat samples were collected on stainless steel substrates, and in one TiO_2 polished substrate by swiping the gun with low feed rate (1 gr/min) at a very high raster speed (1 m/s), the differences between spray conditions are summarized in Table 7. 12 individual splats for eath sample were analyzed by the university of Modena team using a URaman Horiba Jobin-Yvon (Longjumeau, France) spectrometer equipped with a Nd:YAG laser (632.81 nm wavelength) and a 100x objective giving a lateral resolution of 1 – 2 μm. Different powders were sprayed for APS with the same torch parameters to assess the influence that the initial feedstock morphology and/or phase content might have on the resulting quenched droplet characteristics. The use of one TiO_2 polished substrate was implemented with the goal of determining if the wetting differences or heat transfer between the molten TiO_2 and the substrate material would make a significant difference on the resulting splat.

Spray Method	Substrate	Powder	Mean Particle Velocity [m/s]	Mean Particle Temperature [°C]
Plasma Spray	Stainless Steel & TiO2	Agglomerated and Sintered Anatase, Coarse	221	2695
Plasma Spray	Stainless Steel	Agglomerated and Sintered Anatase, Fine	213	2702
Plasma Spray	Stainless Steel	Fused & Crushed Rutile, Fine	219	2574
HVOF	Stainless Steel	Agglomerated and Sintered Anatase, Fine	575	2095

Table 7: Description of Splat Samples for Microraman Spectroscopy

The analysis of the Microraman spectra detailed below indicated that the size of the splats plays a bigger role than the original feedstock characteristics or the substrate in question, for example, in the case of the coarse anatase powder shown in Figure 46, three different basic splat morphologies are observed. Large splats (Figure 46-A), clearly originate from the impact and flattening of fully-molten droplets. They exhibit broadened and very weak Raman peaks, not coincident with those of rutile or anatase. These features suggest that the splats are poorly crystallized and that significant oxygen loss occurred, with the subsequent formation of Ti_nO_{2n-1} phases; indeed, the positions of those weak peaks, located at about 450 cm^{-1} and 550 cm^{-1}, resemble those reported in the literature for Ti_nO_{2n-1} phases $(4\leq n\leq 6)$[141]. This behaviour is consistant amongst the entire large well-flattened individual APS splats analyzed in this study independent of substrate or feedstock characteristics. This indicates that the de-oxidation experienced in the plasma is not reversed for a single splat after impact, and the high quench rates do not allow for complete crystallization of the splat resulting in highly defective and/or amorphous structures

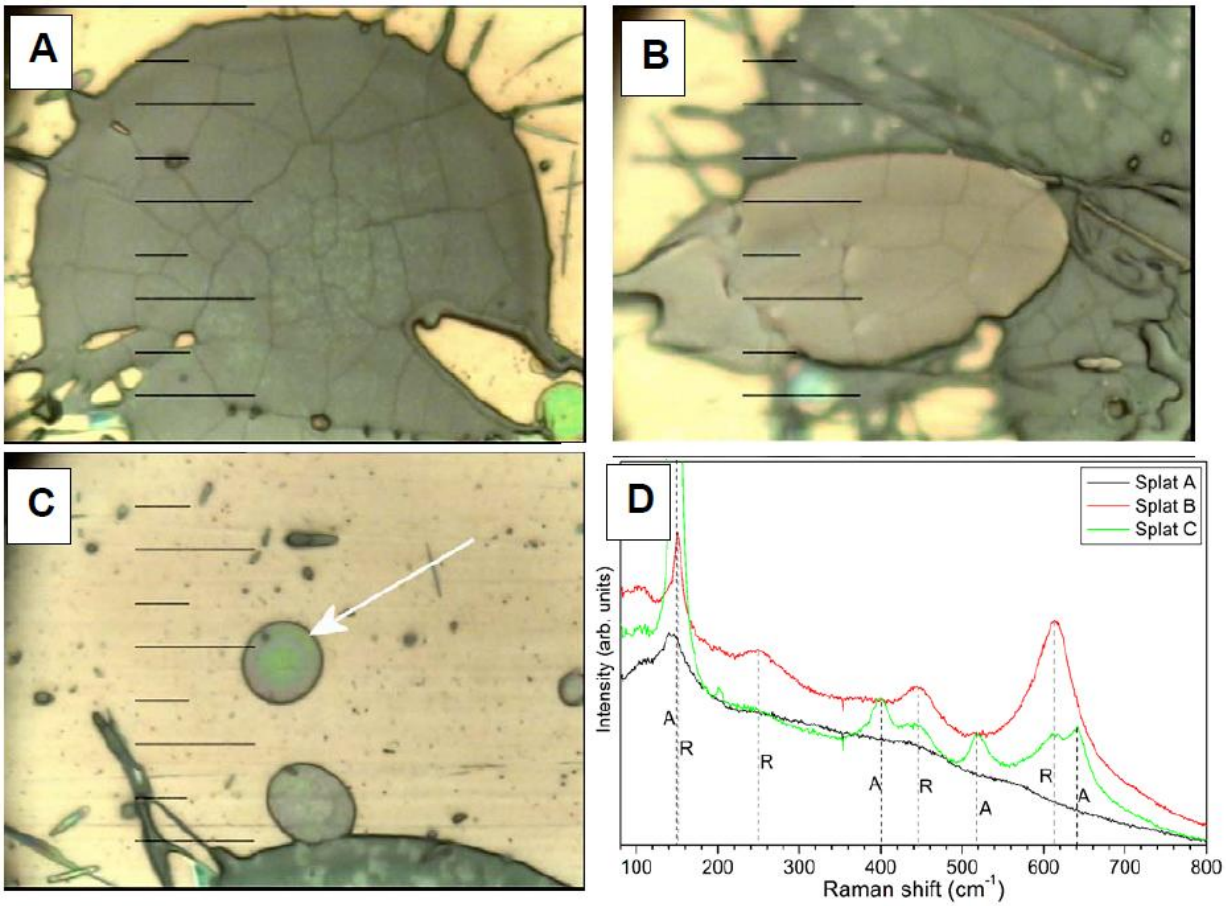

Figure 46: Optical micrographs of (A) Large, isolated, flattened splat (B) elongated and overlapped splat (C) small (probably, also imperfectly flattened) splat (D) and micro-Raman spectra of these splats indicating Anatase and Rutile Peaks

In the presence of overlapping splats (Figure 46-B) rutile peaks are more prevalent, but not always occurring. This could be due to the heat imparted from the previous splat on the poorly crystallized underlying splat, or, because the quench rates during subsequent splat flattening and solidification are lower allowing for more time for a crystalline organization. The fact that the occurrence of these rutile peaks in overlapping splats was not consistent reflects the stochastic nature of the thermal spray process on which a single solidification route is difficult to find.

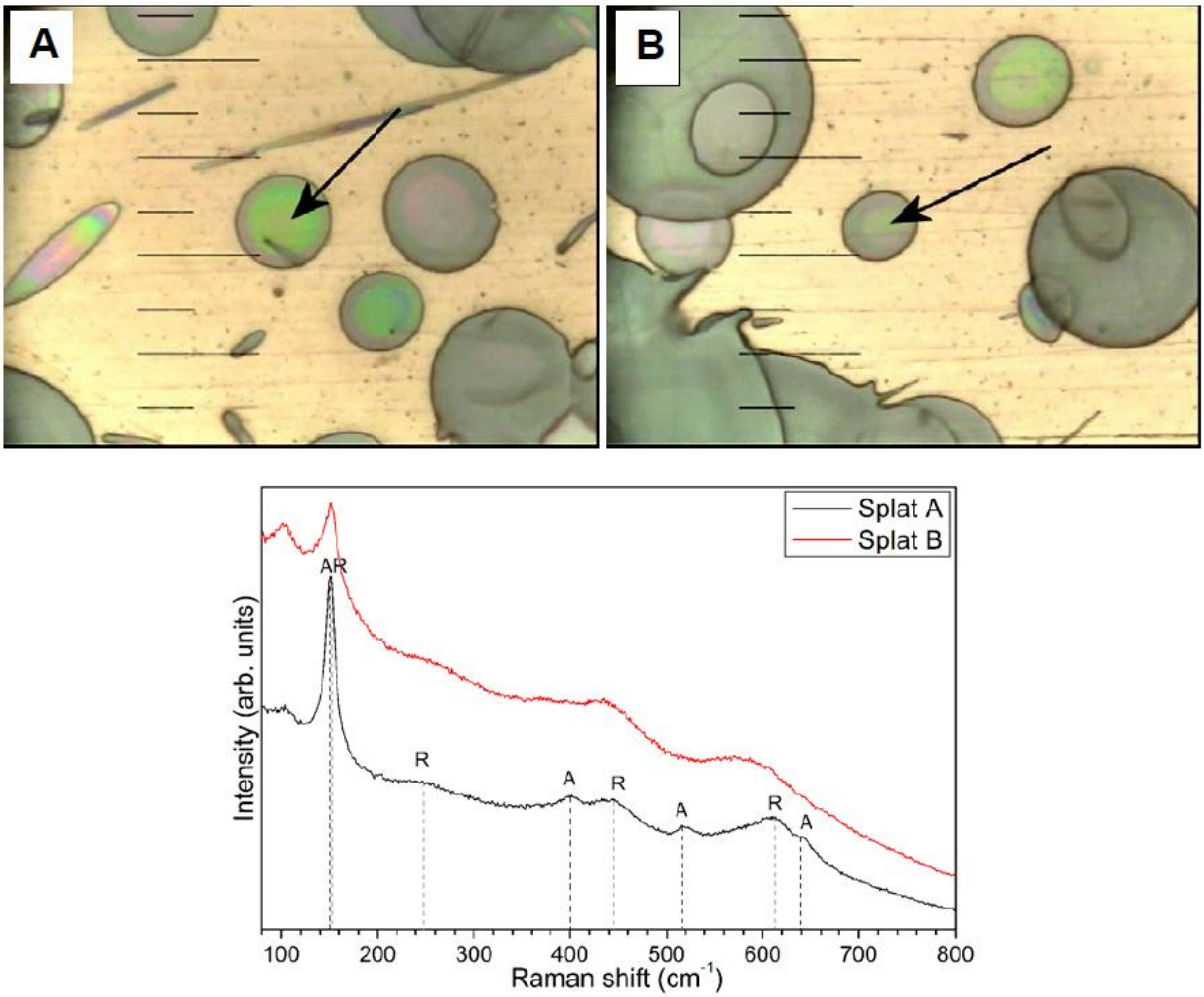

Figure 47: Optical micrographs of two small splats for the fine anatase APS sample and their micro-Raman spectra

The smallest splats such as the one of Figure 46-C, exhibit both rutile and anatase peaks. Given the less kinetic energy at impact and lower reynolds number due to their small diameter these smaller exhibit less flattening and therefore less solidification rates. Although fully cristalized the presence of both Rutile and Anatase structures still raises questions on the exact solidification mechanisms. The presence of Anatase for different smaller splats varies from a strong presence to almost non-existant, as shown in Figure 47, relating this differences with particle history is experimentally very difficult, but such differences are probably related to the presence of re-solidification before impact (not uncommon on the smallest particles) or the relative location of the particle on the gas stream, as finer particles are easily drifted by the turbulence of the flow in contrast with the heavier particles.

Although substrate or feedstock characteristics did not seem to play an important effect on the studied splats Raman spectra, there are observable differences with the larger

splats on the HVOF sample. In general the HVOF fully molten splats resulted in more defined Raman peaks, both of anatase and rutile. These higher levels of crystallization although more prevalent were not always the case, as it can be observed in Figure 48 for fully molten larger splats sprayed with both APS and HVOF methods. The higher level of crystallization of the HVOF splats at first seems counter intuitive, given the known higher quench rates for such a high kinetic energy process, but it should also be noted that HVOF results in lower particle temperatures and lower oxygen loss. This observation allows us to infer that the oxygen loss in APS and the presence of Magneli phases is the main driver for the poor definition of crystalline peaks in the fully molten APS samples. In the case of smaller HVOF splats the resulting spectra does not differ from the APS results, with contents raging from almost complete anatase peaks to a mixture of both.

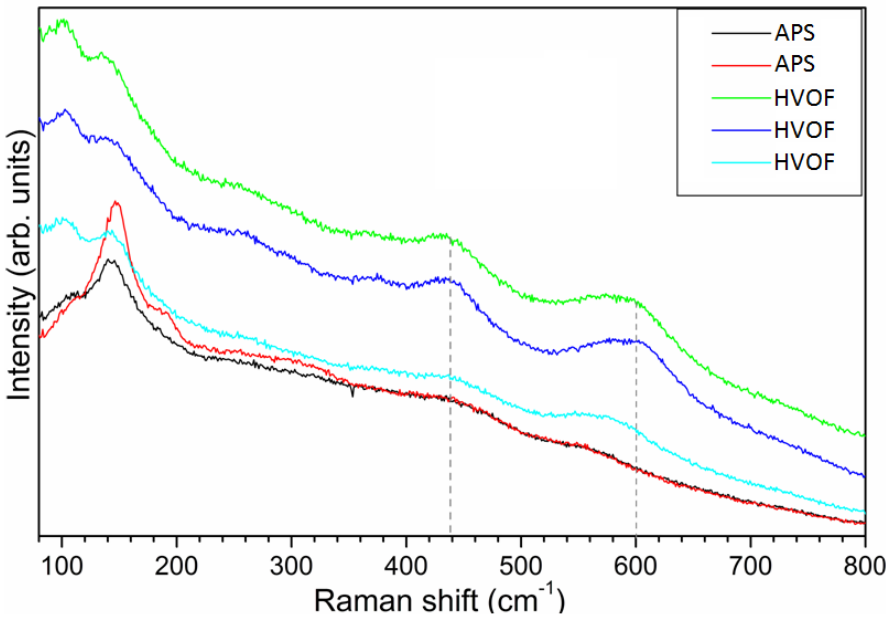

Figure 48: Raman Spectra for fully molten splats

The majority of splats for HVOF samples did not constitute either the “small” or “large fully molten” morphologies but partially molten or “friend egg” splats that were not present in the APS samples as shown in Figure 49. For this type of splats the phase of the unmolten core cannot detected by the Raman spectrometer as they are covered with a layer of molten and re-solidified material, but it the analysis of the re-solidified layer indicates also a defined crystalline structure closer to the rutile spectrum.

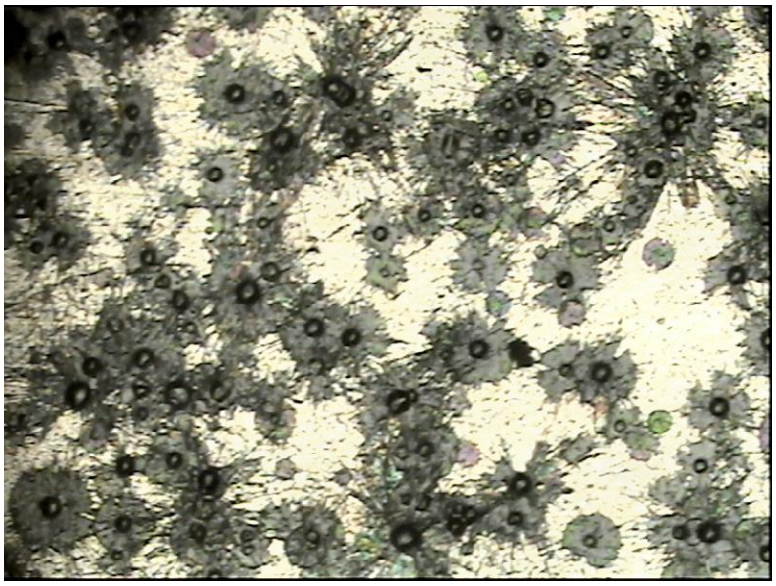

Figure 49: partially molten splats in HVOF sample for Microraman Spectroscopy

In order to confirm aforementioned assumptions on the size dependency of molten state of the particle stream a DPV measurement of 10,000 particles was performed for both HVOF and APS process conditions applied in this work. The individual particle data was separated in two tiers of particle sizes below and above 20 µm. From Figure 50 it can be observed that although the mean particle temperatures and velocities for the two size tiers are quite similar, the smallest particles result in a much higher melting state given their lesser mass and thermal inertia. Similar results were also obtained for HVOF spray.

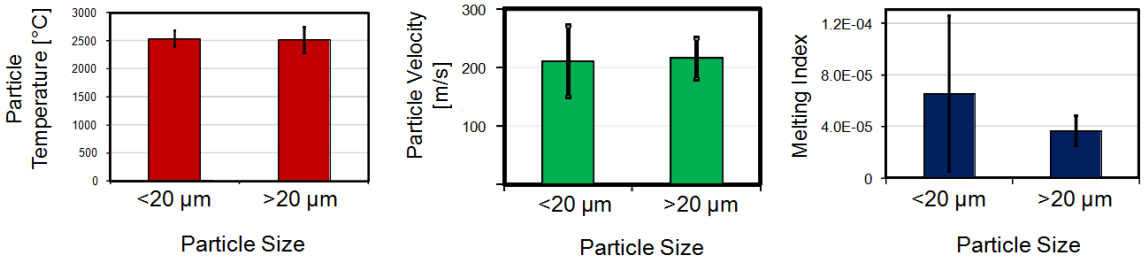

Figure 50: size dependency of particle melting state

To summarize, the differences in individual splat phase selection routes and their dependency on solidification rates explained in Figure 45 are further influenced by sizing effects. The findings of individual splat characterization using micro raman spectroscopy

can be outlined in Figure 51, where the spectral responses in individual splats where found to be defined by the following mechanisms:

- Smaller splats tend to present more defined peaks more likely with anatase spectra, this would be consistent with the previous quench rate dependency observations since smaller particles tend to fully melt given their lower mass and accelerate faster given their lesser inertia

- The introduction of disorder with processing induced stoichiometric losses resulting in magneli phases lacking oxygen atoms in specific locations of the rutile crystalline structure can explain the lesser definition of the Raman peaks for APS splats than their HVOF counterparts, given than HVOF particles do not reach the higher temperature levels of a plasma plume that foster oxygen vacancies, more detail on these mechanisms will be detailed further on the next section analyzing the interplay between phase stability and stoichiometric issues

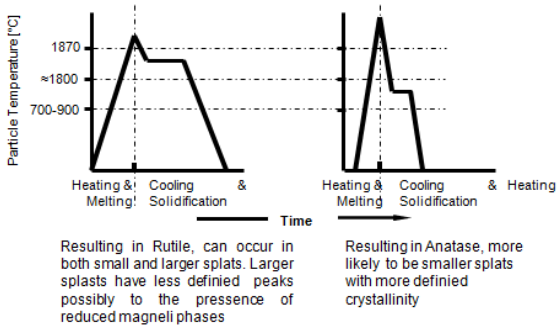

Figure 51: reconciliation of proposed solidification pathways with individual splat raman spectroscopic analysis

4.5 Exploratory Studies of Liquid feedstock thermal spray of TiO_2

Since the introduction of the liquid precursor thermal spray technique [76] several important advances in the understanding and control of the liquid TS method have been achieved, hereby we summarize the most significant:

Injection Visualization has shown that the penetration in of the liquid into the plasma plume will have a defining effect on the feedstock plasma interaction, not only controlling the molten content and particle temperature as in conventional thermal spray, but also defining the level of atomization and fluid evaporation or thermolysis [142]

Different pathways to microstructural formation are known to occur during the spray process for suspension feedstock material, these include the complete evaporation of the solvent and melting of the particle resulting in a splat with same morphology as conventional TS but with a smaller size[143] given the finer suspension powder size distribution, another possibility is the evaporation of the solvent after the impact, this

mechanisms are defined by the level of atomization of feedstock stream resulting in an stochastic dynamic liquid-flame interaction. The agglomeration of fine suspension particles during flight is also a common phenomena [144]. The choice of solvent and heat source (torch) are key in defining coating microstructure[145] and phase content[146] which is a defining characteristic in the development of photocatalytic titania coatings. For example, since water has a higher enthalpy of evaporation, viscosity and surface tension than alcohol, aqueous solutions will result in lesser atomization with larger droplet size, which also results in higher drag force and acceleration. All this translates into denser coatings. Alcoholic suspensions could result in over-atomization if the fluid properties are not correctly tailored. Suspension or Precursor droplets that are too fine drift too easily due to turbulence and flame/atmosphere interaction resulting in poor kinetic energy at impact

Previous studies analyzing process-structure relationships conducted in the National Institute for Material Science of Japan have concluded the need for higher power conditions and elevated substrate temperatures to achieve fully molten status with the use of ceramic inks as feedstock[147]

4.5.1 Experimental objectives and technical information

The aim of this series of experiments was to introduce the liquid feedstock method to the HVOF and APS hardware present at the National Institute for Material Science of Japan (NIMS), this required the design of an external injection mount for both the SG-100 plasma torch and the JP-5000 HVOF shown in Figure 52-a. the method for liquid injection was chosen as mechanical injection given its simplicity and lack of special atomizing dynamics, the implications of this decision will be discussed later in this manuscript. The size of the injector orifice was controlled by the use of different medical syringe needles and based on injection diameters used by previous researchers, the two internal needle diameters choosen where 300 µm for APS injection and 450 µm for HVOF. Pressure for the liquid flow was supplied by the use of compressed air and solution homogeneity was maintained with the use of a magnetic stirrer and the use of organic dispersant agents. An schematic of the liquid feedstock injection set up is show in Figure 52-b

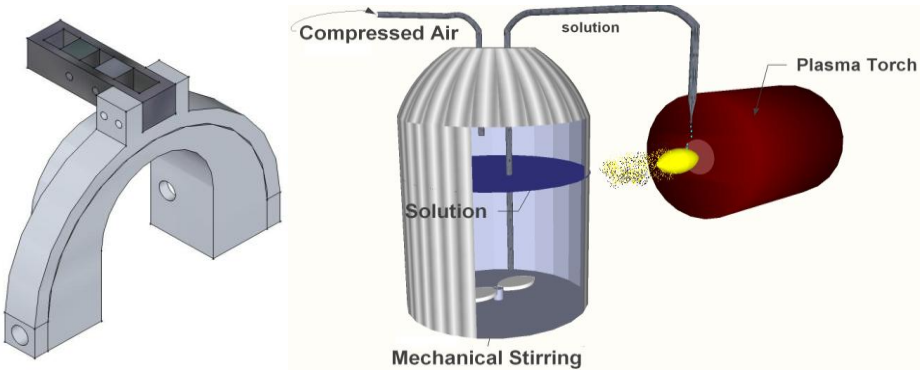

Figure 52a: Injector holder for both APS and HVOF torches, Figure 52b: diagram of liquid injection setup into an atmospheric plasma spray torch

4.5.2 Experimental Design

Experimental conditions were chosen to provide different levels of heat input to the feedstock without overextending the reach of the experimental matrix. Since the process presented some technical challenges, especially in the continuous feeding of the liquid material only two levels of enthalpy variation where implemented by means of current change in APS and combustion chemistry in HVOF, a summary of the experimental design is shown on Figure 53 indicating the different processes, torches and energy levels experimented. Other parameters where also studied without including them in the complete experimental matrix such as the raster speed of the robot and the introduction of cooling air for APS coatings (air cooling was always present for HVOF coatings) Table 8 shows the parameters used for all conditions applied

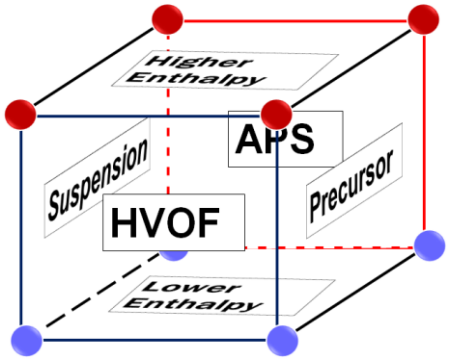

Figure 53: Process Conditions Cubic Experimental Design

APS

Changed

Current
1100
750

Fixed

Raster Speed	Argon Flow	Helium Flow	Injector Diameter	Spray Distance
60*mm/s	105 SCFH	18 SCFH	300µm	100 mm

HVOF

Changed

	Oxygen [scfh]	Fuel [gph]
Oxidizing	1900	5
Reducing	1700	7

Fixed

Raster Speed	Argon Flow	Helium Flow	Injector Diameter	Spray Distance
700 mm/s	105 SCFH	18 SCFH	450 µm	200*

Table 8: Process Parameters applied in this study
***spray distances or raster speeds were modified in selected points of the experimental cube for coatings or splats only**

The feedstock solutions applied consisted in a water based suspension with 15% (mass) of 200 nm mean size TiO_2 powder (ST-01, Ishihara Sangyo Kaisha JP) and ammonium salt of polycarboxylate added as a dispersant in a 5% mass of TiO_2 ratio (Seruna D-305, Chuukyou JP). The precursor solution applied was ethanol based with 30% mass of titanium tetra-n-butoxide as a precursor with diethanoleamide in a 5% mass of precursor ratio added as a dispersant (both from Wako Chemical)

4.5.3 Results

4.5.3.1 APS

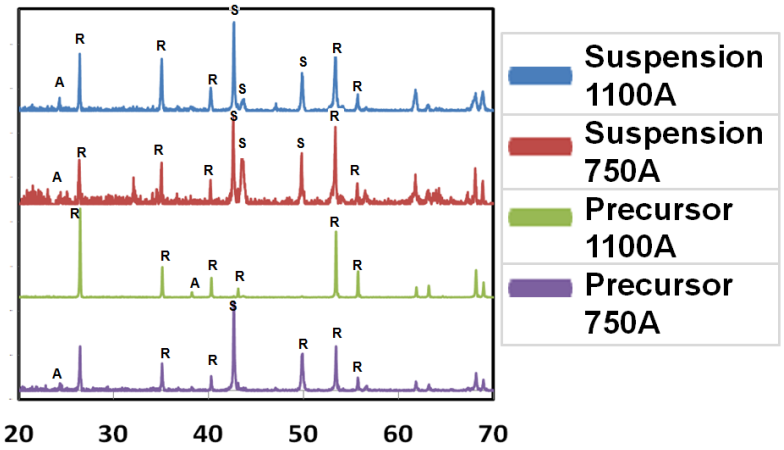

Figure 54: x-ray diffraction patterns of plasma sprayed coatings

Figure 54 shows the different x-ray diffraction patterns for APS coatings, it can be observed that the coatings are mainly rutile phase with the suspension coatings presenting some anatase content. The substrate peaks are also present which agrees with the low

thickness and uniformity of the coatings with the exception of the 1100 amps suspension sample, which was also proven to be the most uniform of the coatings as it is shown Figure 59 below. The anatase content and the approximate substrate temperatures during spraying are listed in Figure 55, from this figure it can be observed that the suspension coatings have a slightly higher anatase content than the precursor sprayed ones. The precursor sprayed condition with high energy (the most uniform) resulted in less than 1% anatase content. Substrate temperature seems to play no effect on anatase fraction and all samples were sprayed at temperatures above 500 °C which is the starting temperature for the anatase to rutile transformation.

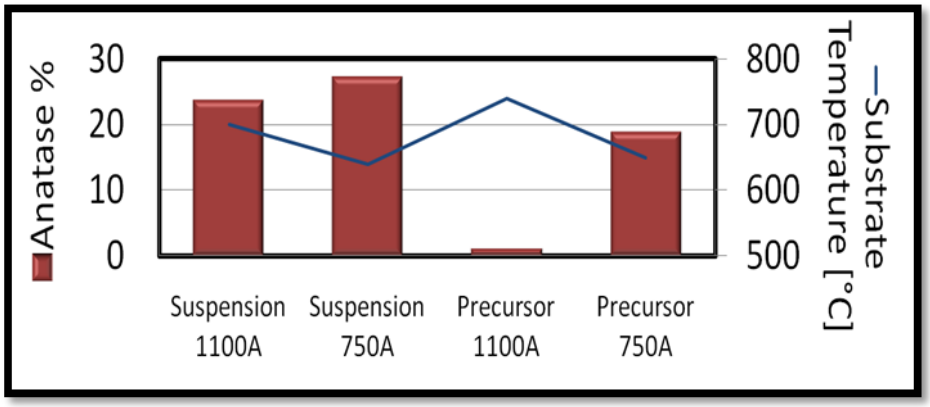

Figure 55: Anatase content and substrate temperature for plasma sprayed coatings

The electron microscope of one torch spray pass over a polished substrate with the aim of collecting individual splats are shown in Figure 56 for suspension feedstock. It can be observed that for the low energy condition -750 amps- the deposited material resembles more the form of an evaporated solution that of a conventional thermally sprayed molten material. The presence of agglomerated and clearly unmolten particles is also noticeable but the most distinct feature is what seems to be the shape of the spread solution droplets that presumably evaporated after the impact. For the high energy -1100 amps- condition there is also a significant presence of unmolten agglomerates but no evidence of evaporated solution, instead disc-shaped splats typicall of thermal spray coatings are present indicating full evaporation of the solvent and melting for part of the feedstock material. These splats do not present stress induced cracking possibily due to their small size as concluded by Blazdell et. al. in 2000[148]

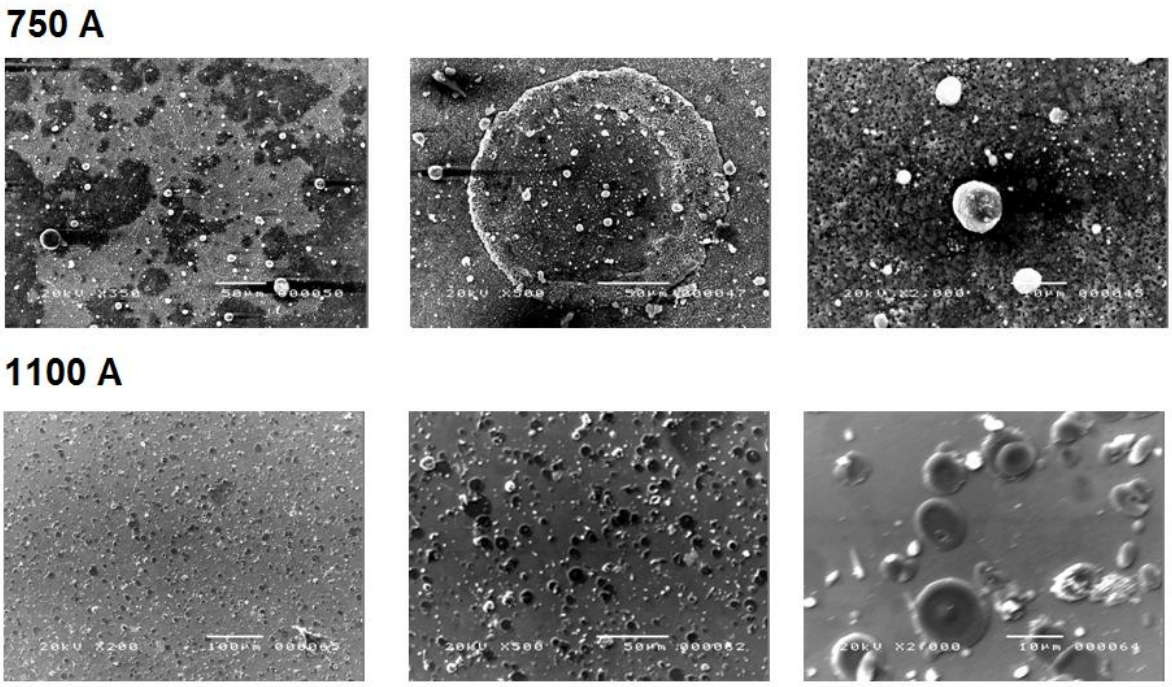

Figure 56: Suspension plasma spray splats

Coatings for both conditions seem rather irregular in microstructure and thickness, the coatings for the 750 amps conditions resulted in extremely low thickness (even for the 47 passes applied), although the coverage for the 1100 amps condition was slightly more consistent, the deposition efficiency is extremely low for the 80 passes used for the experiment. The fact that most of the deposition material was washed away after cutting and mounting in the SEM epoxy sample indicates the low or rather inexistent adhesion of the unmolten agglomerates, leaving behind the small fraction of molten or semi molten coating material shown in Figure 57 which exhibits porous and irregular microstructures.

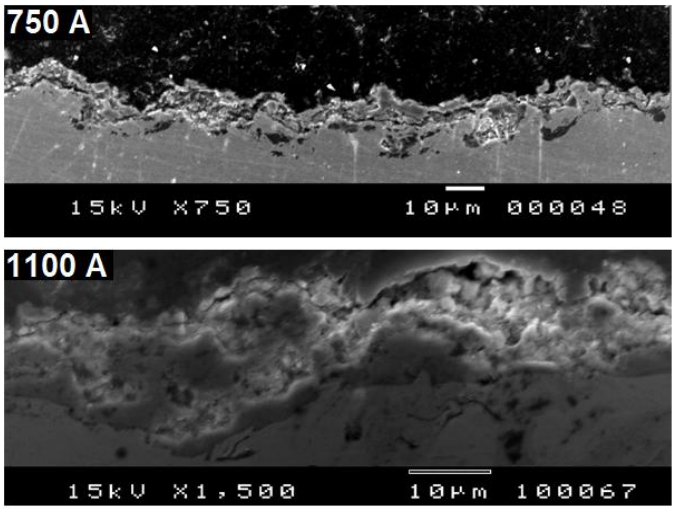

Figure 57: microstructures of suspension plasma spray coatings

In the case of precursor sprayed samples, the one-pass “splat” samples do not show significant difference when the low and high current conditions are compared as shown in Figure 58, in both samples the morphology consists of agglomerates of TiO_2 resulting of the thermolysis of the precursor. This outcome evidences that the heat transfer into the particles although efficient enough to oxidize the organic titanium compound it was clearly not enough to melt it or keep it molten until impact for both energy levels with the only possible difference being the level of agglomeration or atomization.

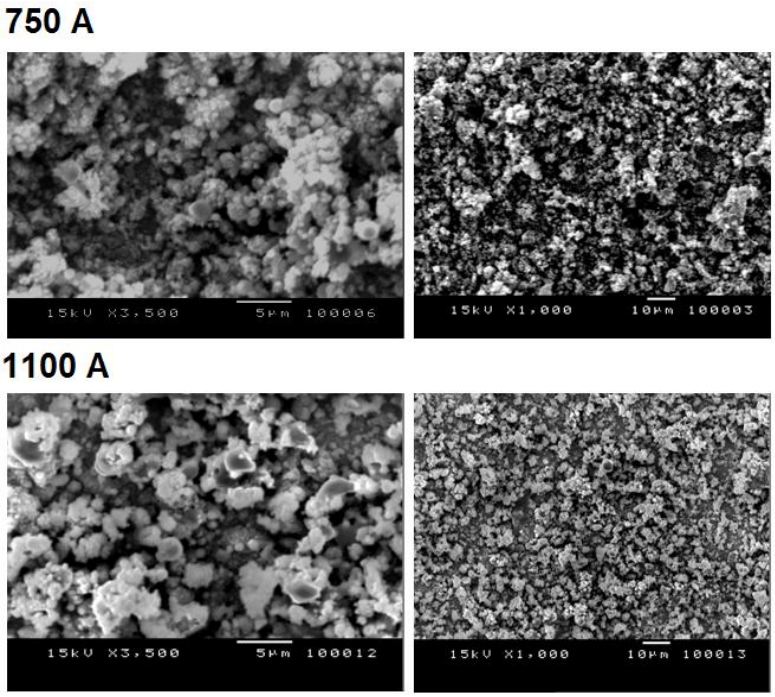

Figure 58: "splat" one pass samples for precursor plasma spray

The multi-pass coating cross sections do show completely opposite outcomes as evidenced by micrographs of Figure 59. The low energy condition barely remained in the sample and the few traces of material left had to be confirmed with EDX (showing mainly Ti peaks in contrasts of the Fe peaks of the substrate). The high current condition in contrast retained a highly porous but rather uniform layer of titanium oxide. The microstructure of this coating is not the characteristic lamellar structure of a thermal spray coating or even the irregular poorly molten and bonded outcome of the precursor plasma spray samples shown above but more of a porous mass which even suggest an interface to surface growth rather than a impingement induced growth. Based on this observation it is proposed that some of the precursor material could be thermolized after impact. This mechanism is analog to the post-impact evaporation of the solvent observed in the low current precursor thermal spray coatings except that in the case of precursor spray the heat of the precursor fluid does not result in the complete evaporation of the fluid (only of the ethanol solvent) but in the oxidation and synthesis of the coating, to the

best knowledge of the authors this is the first work that proposes such mechanism of formation for precursor spraying. The deposition efficiency of this coating (≈20 microns in 37 passes) is significantly higher than the suspension samples but still low compared with conventional thermal spray methods.

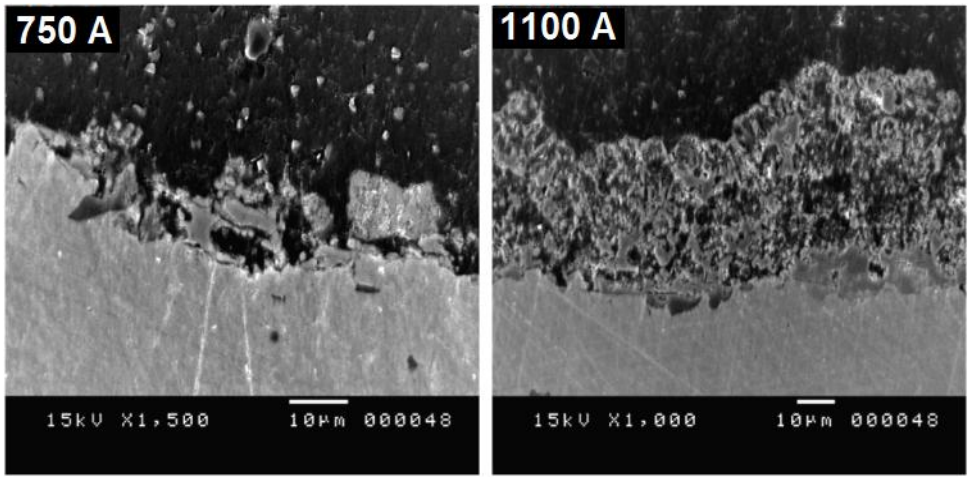

Figure 59: cross section of precursor plasma sprayed coating samples

As it was mentioned in the experimental design section of this manuscript other experiments where conducted regarding the introduction of cooling air and change of robot transversal speeds to observe changes on phase or microstructure, especially with the aim of increasing the low content of anatase found in the plasma sprayed coatings. The inclusion of cooling air for the 1100 amps condition did not result in any significant phase change, for the low current condition however with the increase of robot transversal speed and a decrease of substrate temperature below 500°C the anatase content is significantly increased as shown in Figure 60. Unfortunately this coating condition resulted in a poorly bonded coating that easily detaches when cut and mounted in the epoxy microscope sample, but this result suggest that the low content of anatase in the APS liquid sprayed coatings might be result of post-deposition transformation, this effect could be intensified by the low deposition efficiency of the technique and the long spraying periods necessaries to achieve a uniform coating.

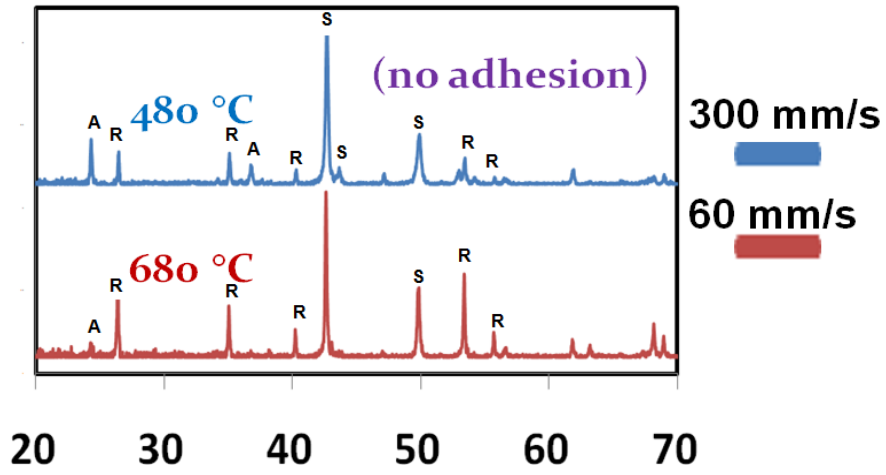

Figure 60: Effect of raster speed on diffraction pattern for low current precursor sprayed coatings

4.5.3.2 HVOF

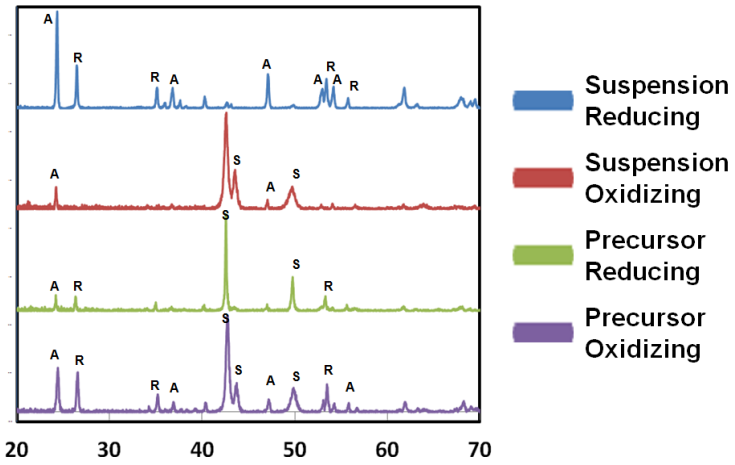

Figure 61: x-ray diffraction patterns of high velocity oxy-fuel coatings

Figure 61 indicates presents the different x-ray patterns sprayed with the high velocity combustion torch, the first obvious observation is that there is a significant amount of anatase present, similar or higher than the rutile content in contrast to the coatings obtained by the APS method. The substrate pattern is also present but almost unnoticeable for the suspension sprayed coatings with a reducing atmosphere, which were also the densest and most uniform coatings of the experimental series. The anatase content and substrate temperature are summarized in Figure 62, it is observed that the suspension coatings results in slightly higher anatase content, of up to 90% for the oxidating flame. The substrate temperature also does not play a significant role on

anatase content as both flame chemistries results in temperatures above 500 °C. This experimental series where applied with the inclusion of cooling air for all coatings and a much higher raster speed than the APS experiments so no additional attempts to lower substrate temperatures with this approaches were executed.

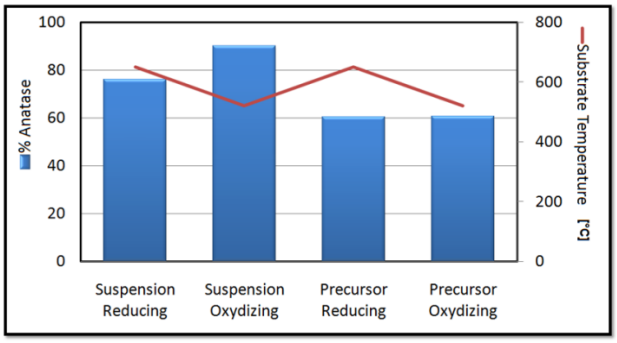

Figure 62: Figure 5: Anatase content and substrate temperature for HVOF coatings (anatase content is quantified used the equation present in[149])

Splat samples for the HVOF suspension runs are shown in Figure 63, significantly different splat morphologies can be observed for the different combustion chemistries applied. For the oxidizing flame individual impacted particles are observed that resemble classic splat morphology, but when detailed at higher magnifications it can be observed that there is 2 different fundamental types of splat present, the first resembles common molten disc shaped splats, which are not as commonly present. The second which is much more occurring than the first consists of impacted agglomerates that seem to retain the fine nanostructured morphology of the original feedstock which indicates poor or incomplete molten status. In the case of the reducing flame the splats present a multiple impact drop morphology non characteristic of thermal spray, when observed at high magnification some retention of the original nanosized feedstock can be observed along with “pores” that suggest the violent escape of fluid after impact agreeing with the possibility of post-deposition solvent evaporation

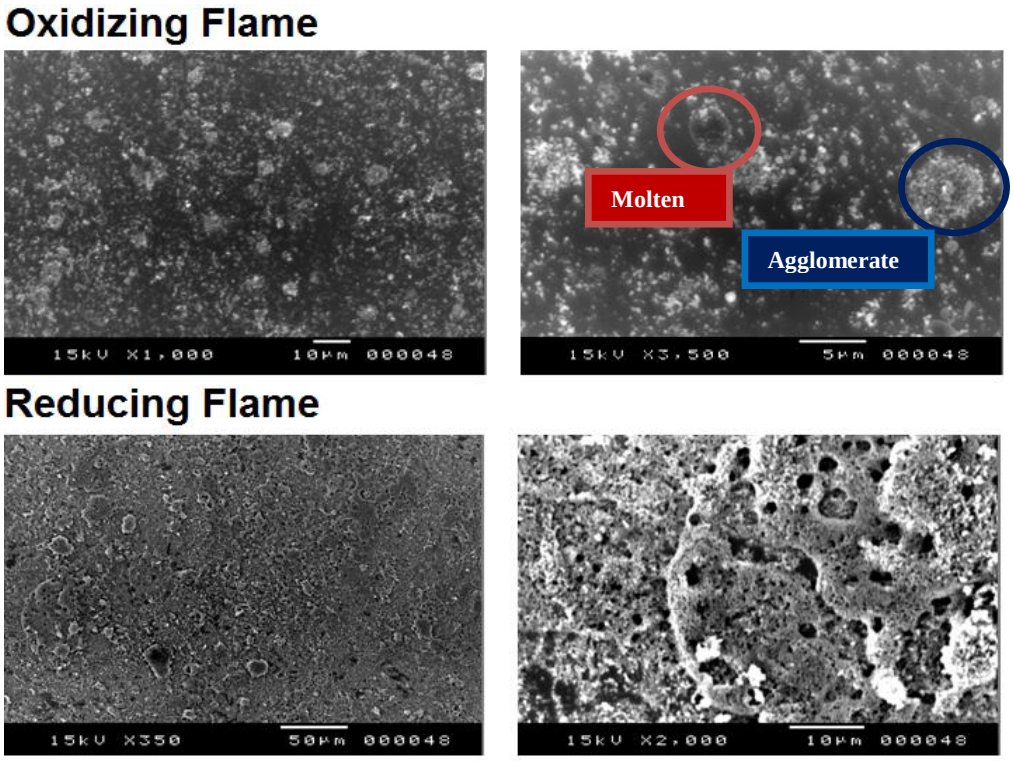

Figure 63: Suspension HVOF splats

Coating microstructure is shown in Figure 64 for the suspension HVOF samples; it can be observed that the oxidizing conditions resulted in inconsistent deposition of very low thickness. For the reducing condition the coatings are more uniform, thick and also noticeable denser than their APS counterparts. It is known for the JP-5000 torch that a reducing flame usually results in a higher particle temperature than the reducing condition since the lack of oxygen in the mixture forces the flame to absorb oxygen from the surrounding atmosphere keeping the flame longer and consequently the residence time of particles in the combustion boundary is also extended. This premise can explain the higher deposition efficiency of the reducing condition; also the reducing flame experiment had 18 passes while the oxidizing flame only 12, but this difference cannot explain the large variation in coating thickness and uniformity.

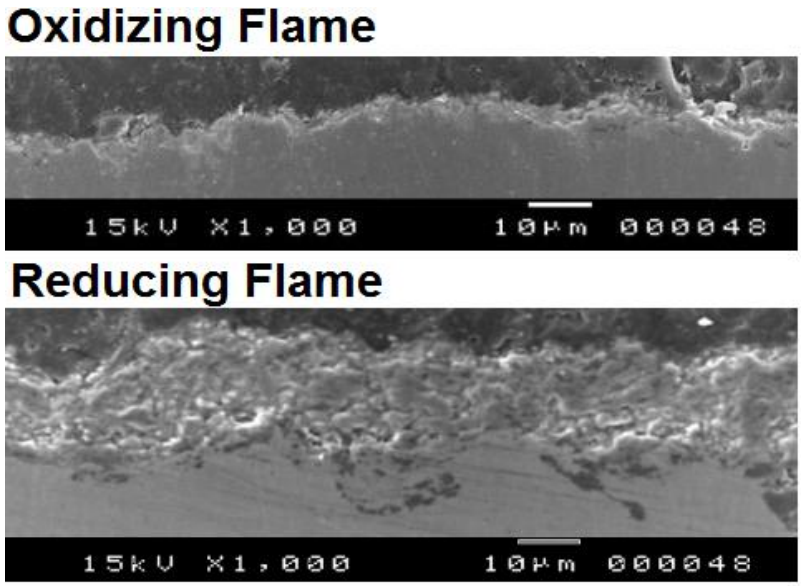

Figure 64: Cross section of suspension HVOF samples

4.5.4 Precursor spray

In Figure 65 the difference between splat samples for precursor splats is presented. Similarly to APS precursor spray both samples present a high content of solid agglomerates resulting from synthesis of the precursor without melting, producing deposits that resemble the unmolten particle agglomerates of suspension spraying. In reducing flame however, there are some disc shaped splats, suggesting the partical melting of the synthesized ceramic

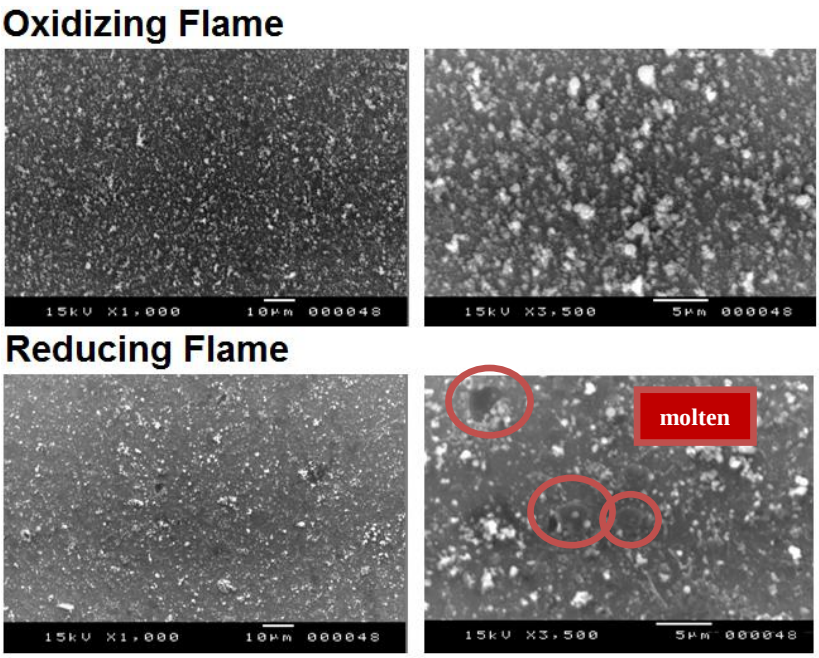

Figure 65: Precursor HVOF splats

Coating deposits (Figure 66) resulted in very low deposition efficiency for the 12 passes applied, it must be noted thought that the coating adhesion proved uniform for both samples covering the complete cross-section of the coating without any detachments as observed in with the other hardware and feedstock combinations

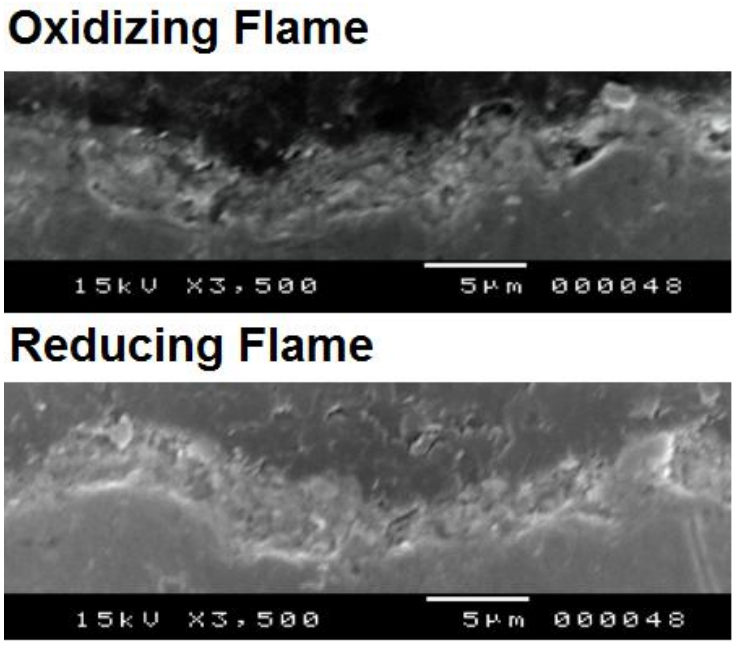

Figure 66: Cross section of precursor HVOF samples

4.5.4.1 Issues with Liquid Atomization

Optical observation of the fluid interaction with the heat source is insufficient to provide a quantitative description of the atomization level of the feedstock, but it still adequate to obtain an overall idea of the consistency of the injection. From Figure 67 we can observe that the APS suspension injection occasionally presents large size droplets that did not penetrate the plasma stream and did not atomize or resulted in molten particles, it must be noted that this large droplets are not a constant occurrence in the processes but the picture is still an evidence of the poor penetration of the liquid into the flame. For APS precursor injection no large droplets are observed and the alcohol present on the stream ignites given the high temperatures of the plasma, it is unclear if this combustion contributes to the melting or agglomeration of the feedstock but this better atomization could explain the higher consistency of the precursor coatings compared with the suspension sprayed samples. For HVOF spraying (both precursor and suspension) the penetration and

atomization of the liquid is uniform and continuous, possibly due to the higher flow of gasses and lesser presence of vortex given the high flow velocities

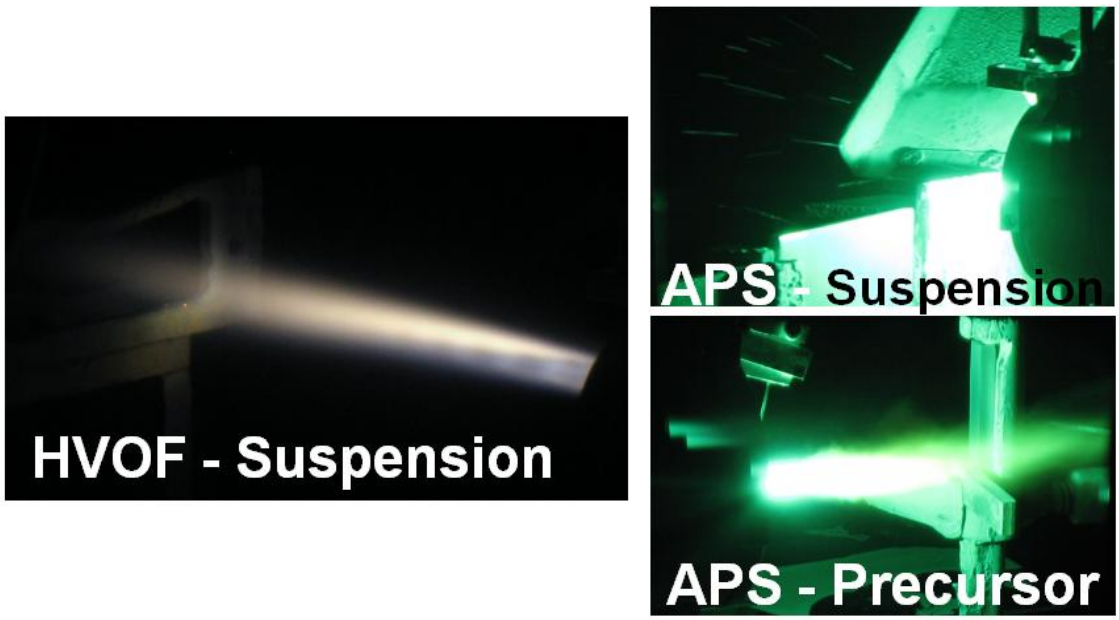

Figure 67: Conventional Photographs of Liquid Interaction with Flame

4.5.5 Conclusions on liquid feedstock thermal spray

In the case of Atmospheric Plasma Spray both Precursor and Suspension coatings result of thermodynamically stable rutile, with suspension coatings consisting in slightly higher anatase content. Since phase content is independent of substrate temperature if T_{subs} > 500 °C it is inferred that high substrate temperatures for prolonged spraying times could further decrease the anatase content.

APS coatings resulted in irregular and poorly adhered microstructures with the exception of the high current (1100 A) precursor coatings, which were the only conditions exhibiting an uniform well adhered coating. These coatings presented a non-conventional microstructure for thermal spray processing which seems to result of the oxidation and synthesis of the precursor into a solid ceramic occurring after the impact of droplets during spray. This new mechanism is proposed additionally to the already known formation mechanisms suggested in the literature for this method.

High Velocity Oxy-Fuel coatings resulted in predominantly anatase composition, being the suspension specimens with higher anatase content, consisting of a combination of unmolten particle agglomerates and molten splat morphology, agglomerates can be individual imparted particles or dispersed droplets resembling post-impact solvent evaporation

Precursor splats also contain significant amounts of unmolten agglomerates that are bonded together by mechanisms other than conventional molten splat impact such as post-deposition synthesis of precursor, these coatings resulted in uniform but inefficient coverage of the sample.

HVOF coatings present a clearly more efficient atomization of the feedstock possibly due to higher gas flows and less presence of turbulence and vortex in the hot zone of the plume. A deeper study on injection atomization and process parameter optimization is needed for efficient processing APS coatings given the stochastic nature of the multiphase atomization/evaporation/synthesis phenomena

These conclusions of solidification pathways can be summarized in Figure 68, where the difference solidification pathways are proposed in concordance with mechanisms observed in previous sections on this chapter, the smaller splats resulting from atomization of the liquid feedstock are in agreement with the size dependency of anatase splat solidification suggested in the micro-raman studies, since with this techniques much higher anatase contents where achieved than with coarser splats conventional thermal spray methods. The presence of liquid solvent absorving energy during processing can inhibit the anatase to rutile transformation suggested for unmolten particles in convenctional thermal spray. Another mechanisms for anatase to rutile transformation is suggested for suspension spraying in APS, where the efficiencies were low and the coating was exposed to high temperatures for longer periods of time and higher substrate temperatures than in conventional thermal spray, obtaining coatings consisting of mainly rutile crystalline structure.

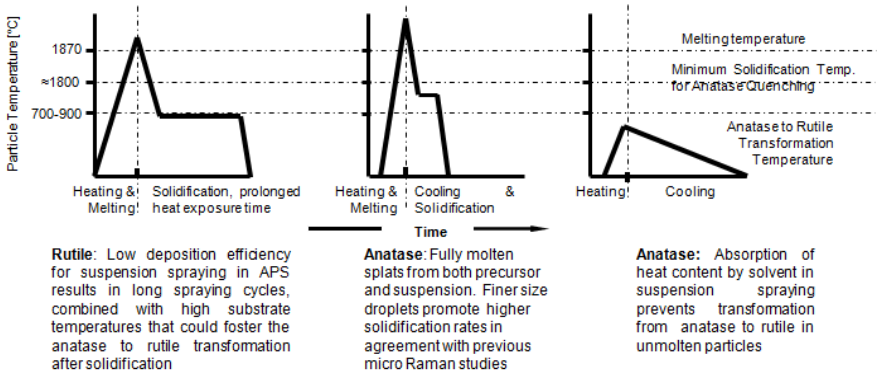

Figure 68: reconciliation of liquid feedstock thermal spray solidification pathways with previously proposed mechanisms for conventional thermal spray

4.6 Interplay between phase stability issues and processing induced stoichiometric losses in titanium dioxide

The functional potential for thick film mesoscale manufacturing of electronic materials with thermal spray processing relies on the lack of prost-processing that is required in today's industrially accepted screen printing industry[150]. Thick film devices that range in applications as diverse as power delivery, circuit management, signal processing and thermal management involve the manufacturing of multilayer devices encompassing insulating, conductive and semi-conducting materials, one of these materials being Titanium Dioxide.

TiO_2 sensibility to the low oxygen content of the plasma stream and the high temperature of thermal spray flames has implications further than the overall changes in electrical resistivity of the coating. Sharma et al. observed anisotropy levels up to 5 orders of magnitude between in plane and through thickness directions of the coating[151]. This anisotropy is assumed to result from heterogeneous de-oxidation of the particles resulting in more electrically conductive interfaces than the core of the splats. The highest concentration of splat-splat contact areas oriented on the coating plane direction explains such heterogeneities, which can be enhanced by post deposition re-oxidation increasing the anisotropy in electrical transport phenomena due to the slow diffusion velocities of oxygen into the materials. This anisotropy is considerable higher than other electrically conductive materials such as silicon[152], which exhibits a difference of near one order magnitude between in-plane and through-thickness resistivities

Sharma's studies relied in a standard set of samples that were sprayed with the same hardware and process parameters, the aim of this section of the dissertation consist in a deepening the knowledge of electrical properties of the coatings due to heterogeneous de-oxidation and diffusion as a function of process parameters variations. Different torch flame enthalpies, the presence of hydrogen or fuel as reducing agents and even non particle state parameters that can affect solidification phenomena are hypothesized to have a direct effect on the density and stoichiometry of splat/splat interfaces subsequently modifying the structure's electronic transport mechanisms.

4.6.1 Particle State Modification and its effect on transport properties through torch hardware modification

This series of experiments focused and the spraying and characterization of coatings with different processes and process equipment to achieve distinct in-flight particle states and temperatures that hypothetically should produce not only marked differences in microstructures but also in oxidation states and even possibly bulk diffusion responses during re-oxidation heat treatment. 4 different coatings were sprayed using 4 processes: Flame Spray, HVOF, and Plasma Spray with two different nozzle diameters (5 and 8

mm) resulting in microstructures as depicted in Figure 69 and with particle states indicated in Figure 70

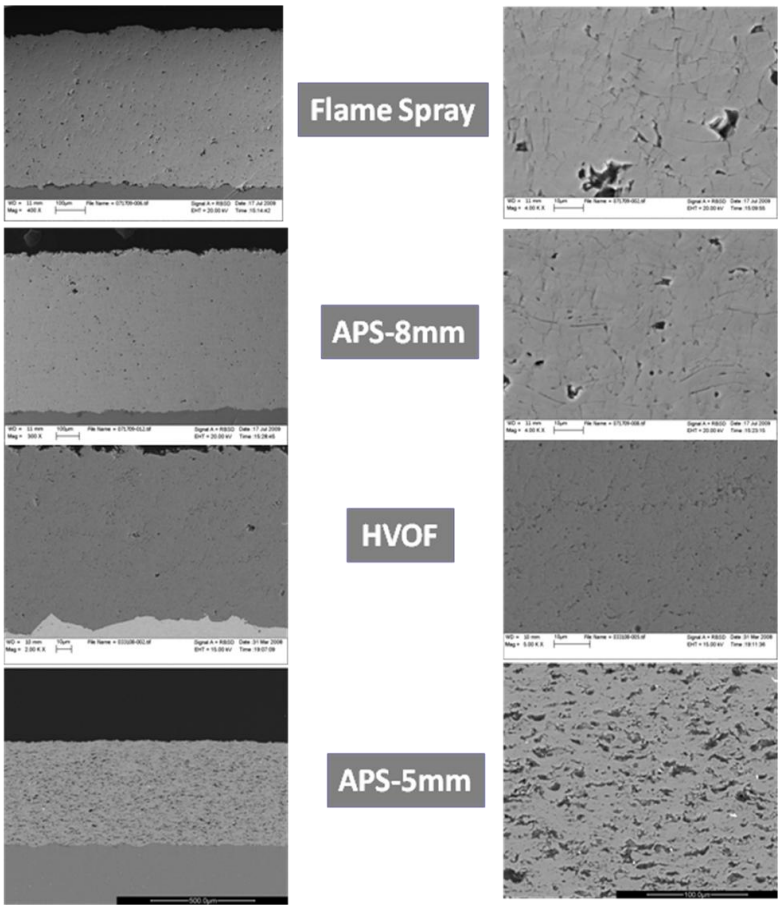

Figure 69: SEM micrographs of 4 different TiO_2 coatings sprayed with different hardware in low and high magnifications

SEM micrographs show that the APS-5mm samples were highly porous and defective with the HVOF samples being dense without almost no noticeable splat-splat interfaces. Both APS-8mm and flame sprayed samples show a dense lamellar structure with larger globular pores as compared with the HVOF samples. It is noteworthy that the flame sprayed samples, although colder than both plasma conditions according to DPV2000 result a higher melting state compared with all the other samples, given the lower flight speed and higher dwell time of the particles.

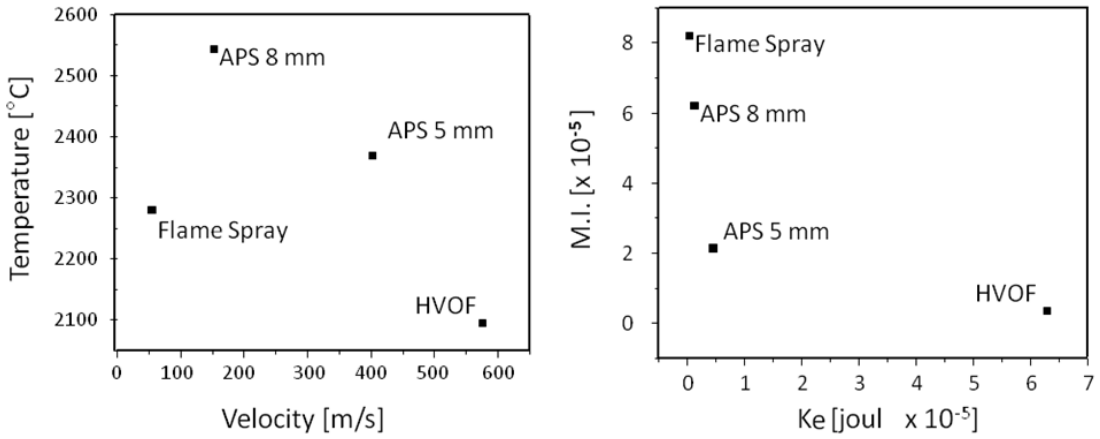

Figure 70: processing particle state for transport property studies

The first transport measurements carried out were through-thickness thermal conductivity. Although both electrical and thermal conductivities are dependent on factors such as a the mean free path of phonons and lattice dimensions of the material[153] it is our hypothesis that microstructural effects are expected to be more defining in a sample's thermal conductivity than on the electrical response since charge can flow through the conductive interfaces independently of the presence of pores or isolative stochiometric splat cores. Thermal conductivity measurements of Figure 71 indicate a raise of conductivity for all samples as a result of the sintering effect due to heat treatment and a significantly more insulative APS 5mm samples as a clear result of the defective microstructure. Both Flame and HVOF samples had the same as-sprayed conductivity, but the flame sprayed coatings were more sensitive to the heat treatment conductivity increase. This result are also an indication were the melting index can a better predictor of microstructural differences, according to simple T-V measurements APS-8mm samples should be hotter and better bonded, but with the melting index calculation, taking into account the dwell time differences a higher melting state and solidification bonding is predicted resulting in the higher thermal conductivity.

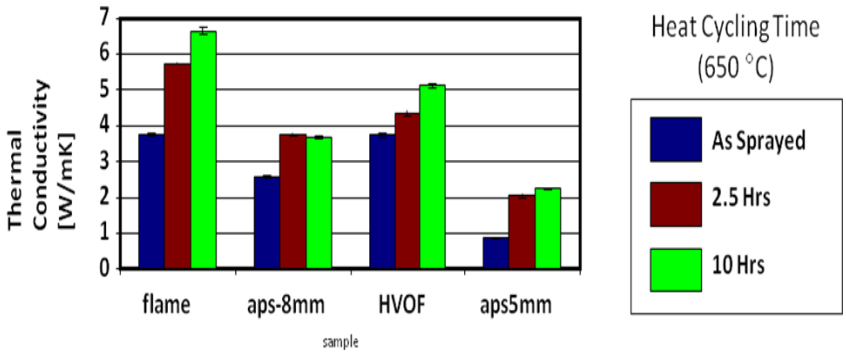

Figure 71: Through Thickness Thermal Conductivity for TiO2 samples with different heat cycling times

Electrical resistivity measurements were conducted in plane with the 4 point probe sheet resistance measurement device and through-thickness resistance was calculated with the constant impedance values of at low frequencies of AC impedance curves reported below in Figure 73. The higher kinetic energy conditions (HVOF and APS-5mm) resulted in a more electrically anisotropic structure. The higher flattening of the splat at impact resulting in a higher density of horizontal splat-splat interfaces than its lower kinetic energy counterparts is interpreted as the primary cause of this higher anysotropy, but it must also be noted that the APS-5mm and HVOF samples also had the lightest blue surface color, suggesting lower de-oxidation as compared from the other 2 darker samples also indicating that the electrically conductive vacancies did not penetrate as much the volume of the splats making the microstructure more dependent on density of splat-splat interfaces to allow for the transport of charge carriers.

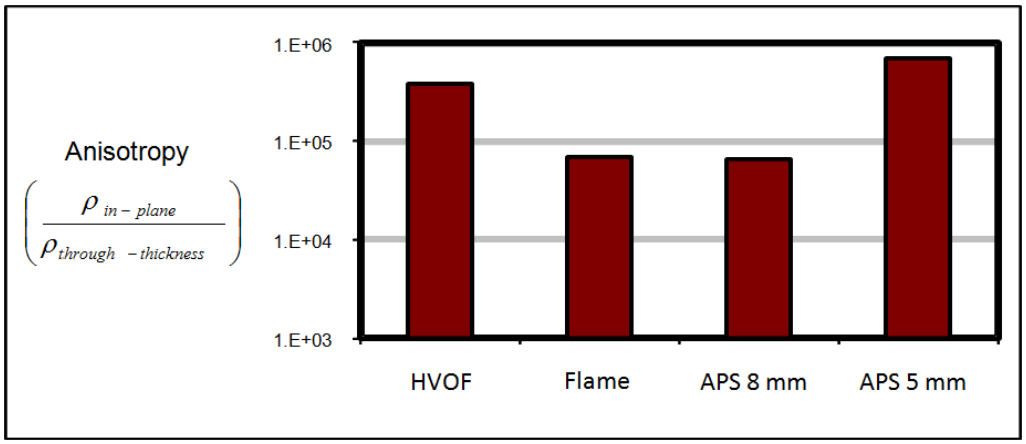

Figure 72: Anisotropy in electrical resistivity of different TiO2 samples

Figure 73 impedance and phase angle responses on the through thickness direction provide very important information on the response to the system to re-oxidation through the spectrum of microstructures studied. The as-sprayed samples present a typical resistor behavior at low frequencies with a phase angle of or close to 0° and constant impedance. The highly defective aps-5 mm sample decreases the phase angle and the impedance to a capacitive behavior at high frequencies before the rest of the samples, agreeing with the hypothesis that such coating has a higher concentration of insulative volume between conductive splat-splat interfaces. Both Flame Spray and HVOF samples have the same as-sprayed impedance, agreeing with the similar

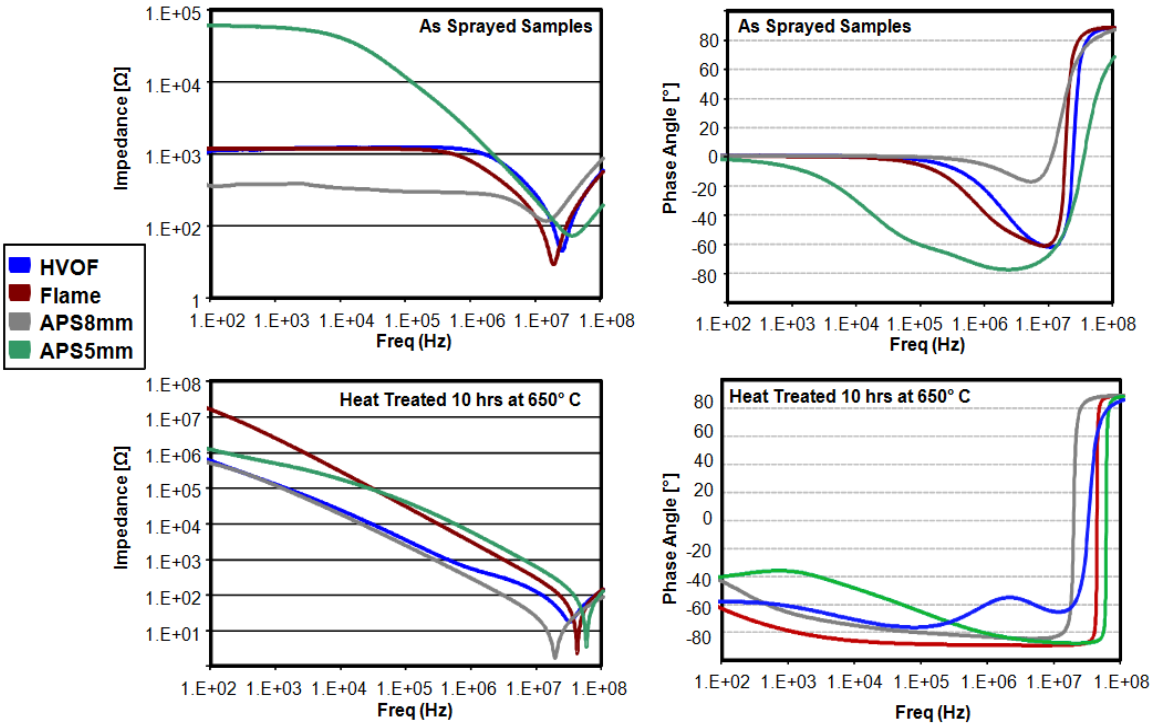

Figure 73: Through Thickness Impedance Measurements for TiO_2 samples with and without heat treatment

thermal conductivity measurements. This similarity in numerical values does not mean the microstructural and transport properties were obained through the same solidification pathway, but it is an indication that different process condition can result in similar functional properties if the parameters are chosen carefully. Although some authors have suggested that denser coatings without the typical lamellar structure known in thermal spray can result in isotropic mechanical properties[154] such isotropic behavior is not likely to translate into electrical properties given the results of this study.

When heat treated for 10 hours at 650 °C the impedance of the samples increases significantly in 1 to 2 orders of magnitude, with the highly defective aps-5 mm sample increasing the lowest and the flame sprayed sample increasing the most. This effect is opposite from the thermal conductivity results, while the sintering makes the structures more thermally conductive by closing of pores and voids, the samples become more capacitive due to re-oxidation and destruction of charge carrying vacancies creating a higher insulative volume between conductive passages. Other researchers have conducted studies with vacuum heat treating proving that annealing in the absence of oxygen will decrease the electrical resistivity of TiO_2 thermal spray coatings and the phase angle behavior will switch towards a positive (inductive) response even at low frequencies[155] which agrees with the observations of re-oxygenation in this work

When in-plane electrical conductivity measurements are carried out for a wider range of process parameters and conditions a second process map of the results can be shown in

Figure 74 overlaping in-plane electrical resistivity of different TiO_2 samples with particle state measurements. From this graph it can be observed that the coating with highest temperature and lowest velocity (APS 8 mm) results in the highest electrical conductivity but when the particle velocity for similar particle temperatures is increased using the 5 mm nozzle an increase in resistivity of an order of magnitude results that cannot be explained by porosity variations since condition since the hottest 5 mm nozzle coating is actually 4.5% less porous than the 8 mm condition. These variations in electrical resistivity are clearly explained by variations in oxygen vacancy concentration, since condition 4 has a lower residence time in the hotter zone of the plasma it will have less time to lose oxygen. Another evidence of these vacancy effects is that the HVOF coatings (above the melting point) display larger resistivities than the condition 8 mm APS condition despite significantly improved density and interparticle strength of HVOF coatings.

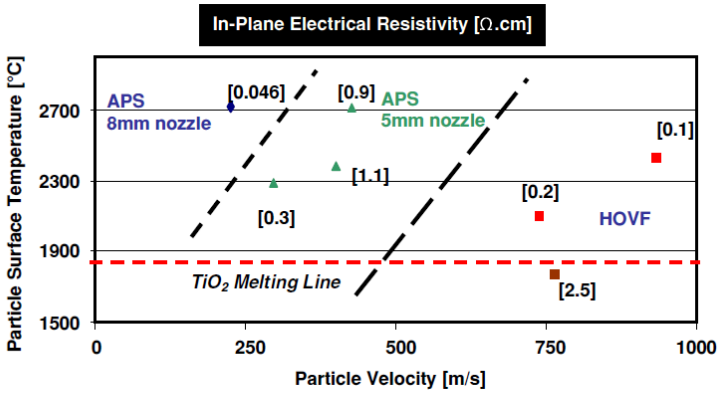

Figure 74: Expanded second order process map of in-plane electrical resistivity for TiO_2

When the electrical and thermal conductivities of the four as-sprayed samples with different hardware are correlated in Figure 75 it can be observed that they follow a common trend for most conductive and semi-conductive materials: Better electrical conductors are also better thermal conductors, but it can also be observed that the changes in electrical resistivities are in orders of magnitude which is explained by the changes in oxygen vacancy concentrations while the changes in thermal conductivity stay in the same order of magnitude suggesting such variations are more influenced by splat-splat interface integrity and overall porosity of the coatings.

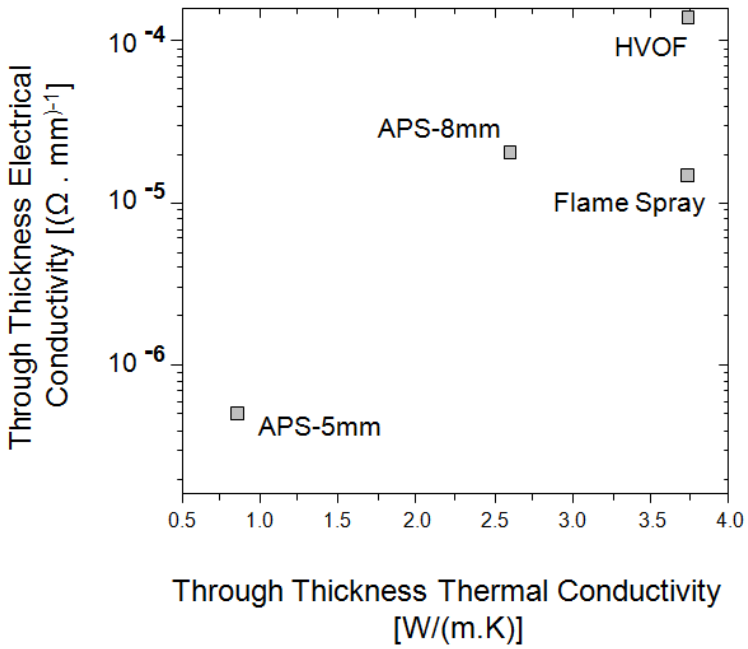

Figure 75: Relationship between electrical and thermal transport properties in the through-thickness direction

The melting index non-dimensional particle state indicator is also an indicator of the state of de-oxidation of the particles given that it takes into account the residence time on the flame from calculations base on both particle velocity and temperature. Another key factor on determining oxygen vacancies, the oxygen partial pressure on the flame is not expected to be as variable as the particle temperature. Figure 76 indicates the predicted for the expanded second order process map sample that a higher melting index will result in a more reduced and electrically conductive coating. As the kinetic energy is more related to splat flattening and coating compaction, and not coating de-oxidation like the melting index indicator, the effect of kinetic energy is not as clearly discernible as a defining factor in coating resistivity. From Figure 76 it can be observed that for plasma spray higher kinetic energy results in more insulative coatings (likely due to the lower residence times/lower de-oxidation) but for HVOF no clear trend is observed.

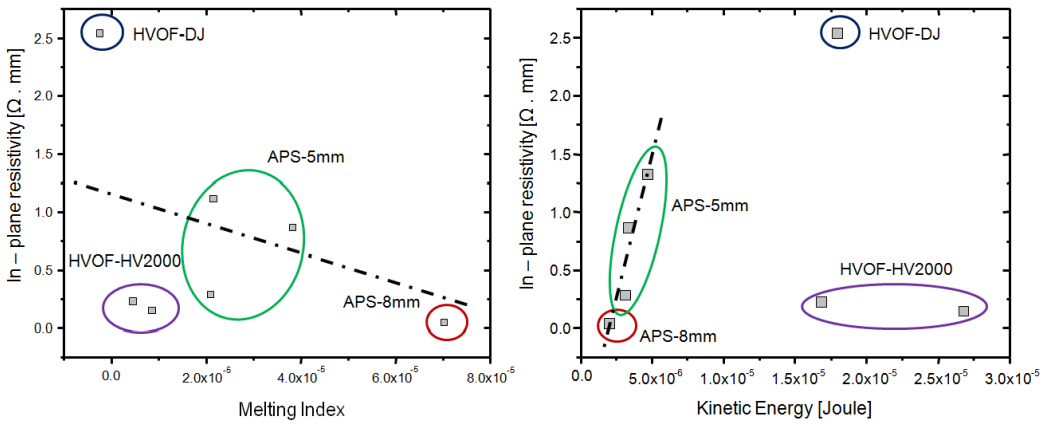

Figure 76: In- Plane Resistivity as a function of melting index and kinetic energy for the expanded 2nd order process map samples

When constructing similar maps for through thickness electrical behavior the trends result in opposite responses as the in-plane resistivity. These results can explain the previous observation of different levels of anisotropy. In this case the APS 5mm coating still maintains the highest resistivity values due to its higher porosity and lower reduction, but the HVOF coating results in the most conductive sample likely due to the high compaction of the coatings. From Figure 77 it can be inferred that coating compaction which is more related to kinetic energy is a main driver of through thickness coating resistivity changes. Changes in coating stoichiometry occur primarily in the coating interfaces, and with the higher density of conductive interfaces between splats in the in-plane direction resulting in an anisotropic system, such changes in stoichiometry do not play as a significant role in the through thickness direction as coating compaction and structural integrity.

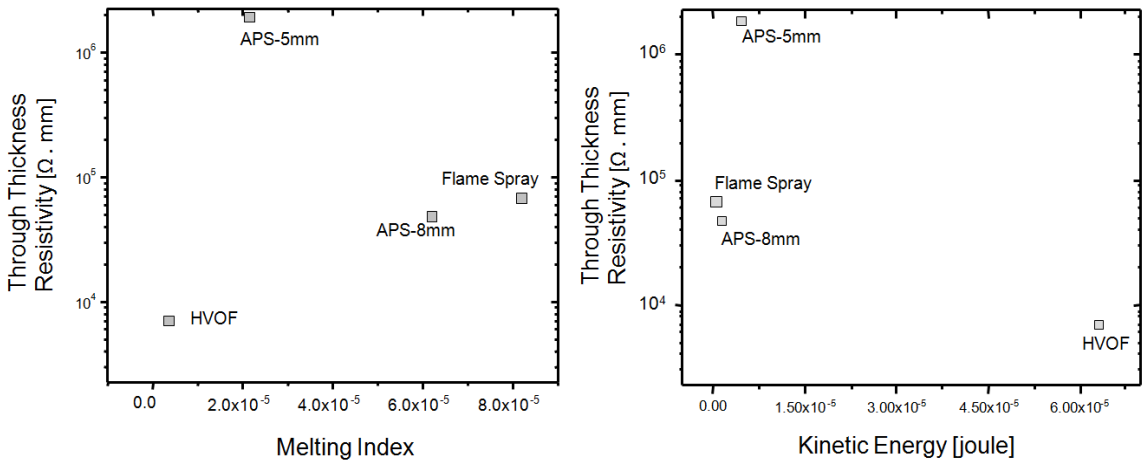

Figure 77: Through thickness electrical resistivity as a function of melting index and kinetic energy

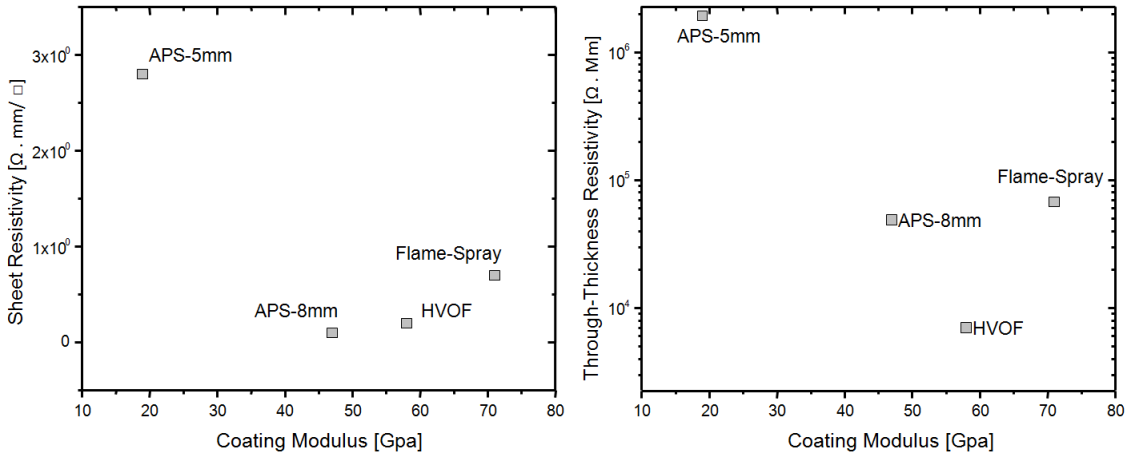

Figure 78: Relationship between electrical and mechanical properties

In Chapter 5 an examination of the structural implications of coating properties will be given in detail, but from Figure 78 it can be observed that the structural integrity and the electrical conductivity are not isolated properties as both are directly related to inter-splat bonding and coating porosity, similar relationships between structural integrity (modulus) and resistivity are observed in both in-plane and through thickness directions, with the difference that the changes in through thickness direction of resistivity are in different orders of magnitude. The following section will detail how changes in non-particle state parameters can or cannot define such structural integrity and electrical resistivity properties

4.6.2 Analysis: Driving force for the creation of conductive pathways in TiO_2 thermal spray coatings

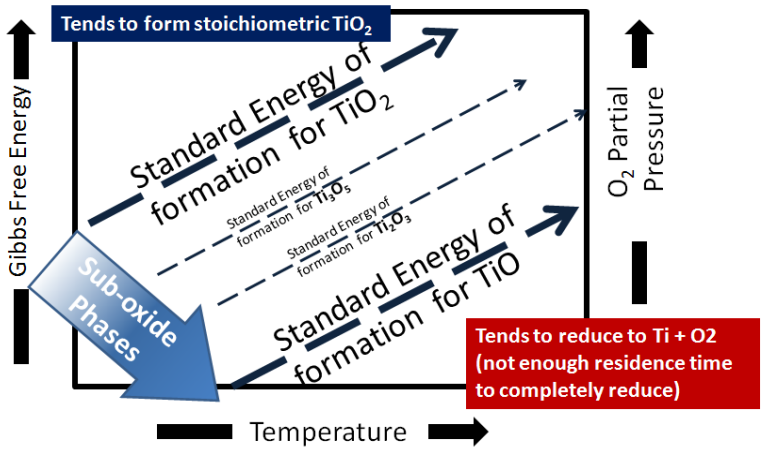

Figure 79: Stability of titanium-oxygen system as a function of surrounding temperature and oxygen atmosphere

To further explain the mechanisms that drive the creation of vacancies in thermal sprayed TiO_2 coatings Figure 79n summarizes the stability of different structures of the titanium-oxygen system as a function of temperatures and surrounding partial oxygen pressures in an Ellingham diagram style arrangement. It must be noted that this depiction is a simplification of a more complex system with at least 12 sub-oxide structures, but the principle temperature effects and variations in oxygen partial pressure is a constant in driving the reduction of the original stoichiometric TiO_2 into a more electrically conductive material. Given that the thermal spray process the change of oxygen partial pressure is not as pronounced as the high temperatures generated by plasma and combustion the main driving force for oxygen loss is attributed to temperature effects in this work. Figure B is also sustained on thermodynamic stability, which is inconsistent with known thermal spray behavior given the rapid nature of the process. Nevertheless particle temperature differences can be the driving force to oxygen losses in the process, although the oxygen loss will be limited to the residence time in the flame resulting in non-uniform de-oxidation explaining the anisotropic behavior found originally by Sharma et Al. Figure 80 outlines the proposed mechanisms that inter-play in the definition of electrical properties of TiO_2 coatings, indicating a compensation between intrinsic properties of thermal spray coatings (porosity/interfaces) that foster insulative behaviors and extrinsic/material dependant defects (vacancies) that promote electrical conductivity. Given that small changes in oxygen content can result in increases of orders of magnitudes in the electrical conductivity of TiO_2 the extrinsic mechanisms predominate in the high temperature zones of the process space.

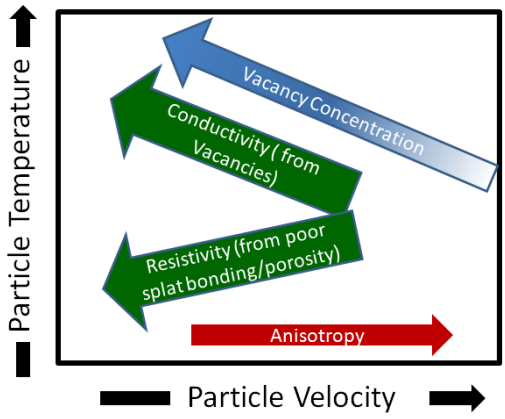

Figure 80: Different Mechanisms that define electrical transport properties for TiO_2 coatings in the process space

4.7 Photocatalytic Activity of TiO_2 coatings and the effect of post-spraying re-oxidation

Despite numerous studies focused on developing photocatalytic coatings with TiO_2, the potential application of thermal spray for this purpose has not been fully investigated. Thermal spray methods have several important advantages to make them especially

attractive for large scale applications. Which include low cost and simplicity of operation[2].

Several published studies on thermal sprayed TiO_2 coatings have concluded that a higher anatase content generally resulted in a higher catalytic activity[28]. Additionally, it has been suggested that smaller crystallite size leads to higher rate of reaction[138]. Although these trends are generally consistent with behavior of TiO_2 in powder and colloidal systems[34, 36], there are several known exceptions where a small concentration of rutile can lead to positive synergetic effects[103]. Notwithstanding a wealth of literature published on photocatalysis, the effects of the oxidation state of TiO_2 coatings prepared by thermal spray on photocatalytic activity have not been thoroughly addressed. It is well known that thermal spray TiO_2 coatings are easily reduced given the high temperature nature of the process, with the stoichiometry being a function of process parameters [30, 157]. Unless the cold-spray technique is employed[158], achieving fully oxidized coatings is extremely challenging. It is known that the oxidation state of titanium plays a critical role in photocatalytic reactions. For example, while Ti_2O_3 is normally considered completely inactive, the presence of a small concentration of oxygen vacancies on a TiO_2 surface can significantly alter the lifetime of the charge carriers and lead to a significant increase in visible light activity without a noticeable decrease in UV activity[159]. It has also been observed that a high concentration of oxygen vacancies can lead to a significant increase in charge carrier recombination and result in a decrease in photocatalytic activity[160].

This section of the dissertation is focused on addressing these gaps in knowledge by relating catalytic performance to coating processing parameters, both during spraying and by the use of post deposition treatment for stochiometric modification.

4.7.1 Coating Processing Procedure

For this part of the work the TiO_2 feedstock was the same as the used in previous sections of the work (chapter Chapter 4) with the difference that the mean powder size of the TiO_2 agglomerates used for the High Velocity Oxygen Fuel (HVOF) process was 25 μm, while for the Atmospheric Plasma Spray (APS) the mean size was 40 μm. The different feedstock particle sizes for each method were chosen to facilitate the feeding of the material for each system as particles too fine make difficult the feeding into APS spraying and a particle size too coarse results in incomplete melting and/or obstructions in the radial injector in the HVOF torch

The parameters used for each coating and the mean particle state indicators as measured by DPV2000 are shown in Table 2. Both coatings were applied in Aluminum substrates

Table 9: Process Parameters and Particle State for photocatalytic coating processing

Coating Method / Torch	Gas Flows [L/min]	Carrier Gas Flows [L/min]	Powder feed rate [g/min]	Spray distance [mm]	Robot transverse speed [mm/s]	Current [A]	Voltage [V]	Mean Particle Temp. [°C]	Mean Particle Velocity[m/s]	Coating Thickness [μm]
APS / Triplex	Ar: 30 He: 20 H_2: 8	Ar: 10.5	60	150	1000	480	119	2400	250	40
HVOF/ HV2000	C_3H_6 : 83 O_2: 240	N_2: 10	15	200	1200	n/a	n/a	2080	530	25

Subsequently, both HVOF and APS samples were cut and a portion of the coatings were heat treated in air at 650 °C for a period of 48 hours to re-oxidize the partially reduced ceramic. While as-prepared coatings had a dark color indicative of reduced TiO_2, the reoxidized coatings had a white color typical of completely oxidized TiO_2 as seen in Figure 81 . These qualitative results were confirmed by other techniques, as discussed below.

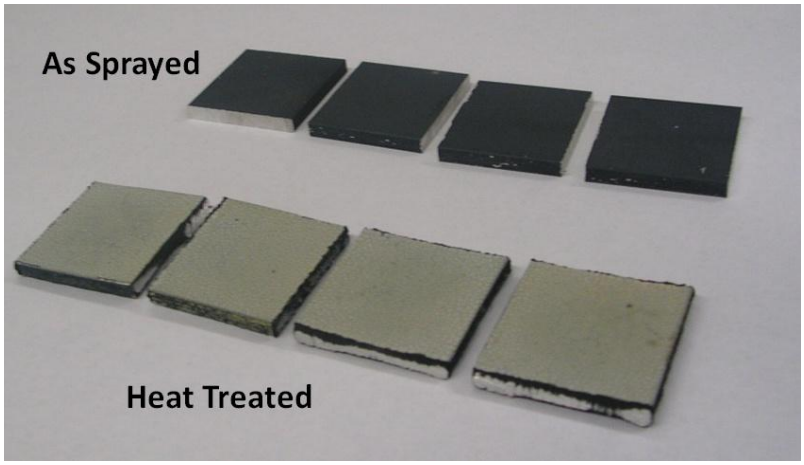

Figure 81: Example of coating color change after heat treatment for the HVOF samples

4.7.2 Spectroscopic Analysis

Similarly to previous results in this manuscript both coatings are mainly consisting of the rutile phase as sown in Figure 82 with a minor presence of anatase, being the HVOF coating the one exhibiting the highest anatase content. In lesser content, both HVOF and APS as-prepared samples showed a presence of Ti_8O_{15} phase, which might indicate the reduction of TiO_2 during the coating process. The presence of various reduced phases of

TiO_2 in thermally sprayed coatings have been observed before[28, 161]. The XRD results did not show the presence of other reduced phases, as described by Burlakov et. al. [162], which might be due to either the small crystallite size of these phases or overlaps with anatase/rutile peaks. The heat treatment of the samples resulted in an increase in sample crystallinity as indicated by the intensity of the diffraction peaks and in a decrease in anatase content, with the APS sample showing only the rutile phase. The phase transformation of anatase to rutile at 650 °C is consistent with other data described in literature[163].

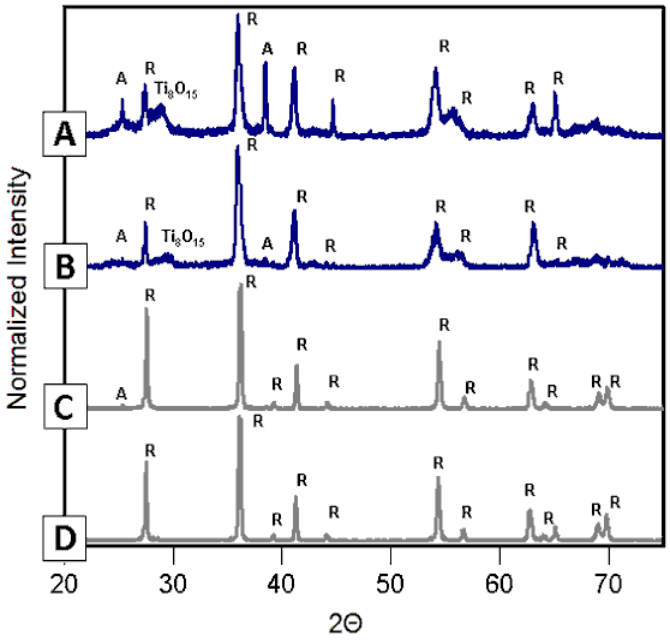

Figure 82: XRD patterns of the coatings: (A) HVOF - as sprayed; (B) APS - as sprayed; (C) HVOF - heat treated; (D) APS – heat treated;

The reduced Ti_8O_{15} Magneli phase completely disappeared from the heat treated samples, consistent with the complete re-oxidation of the sample. This conclusion is supported by optical observations of the increase in color uniformity of the samples and the disappearance of the reduced phases.

Raman spectrographs of the four coatings are shown in Figure 83 . Peaks present at 440 cm^{-1} and 611 cm^{-1}, in addition to a weak shoulder at 805 cm^{-1}, demonstrate the significant presence of rutile at the surface [164]. The peak at 515 cm^{-1}, 638 cm^{-1} and the broadened shoulder at 396 cm^{-1} indicate the presence of anatase. The as-sprayed HVOF spectrum showed a dual character of rutile and anatase, as expected from XRD. The intensity of anatase peaks in this sample was much higher than that for as-sprayed APS coating, consistent with XRD results. In addition, the broadened shoulders at 581 cm^{-1} and 414 cm^{-1} could be indicative of the Ti_8O_{15} phase identified through XRD[165]. These broadened features were eliminated through heat treatment. The only indication of residual anatase present after treatment is in the HVOF sample (broadened shoulder at

396 cm^{-1}). The intensity of the rutile peaks grew significantly, which can be attributed to an increase in crystallinity of the sample, increase in crystallite size and elimination of the reduced Ti_8O_{15} phase.

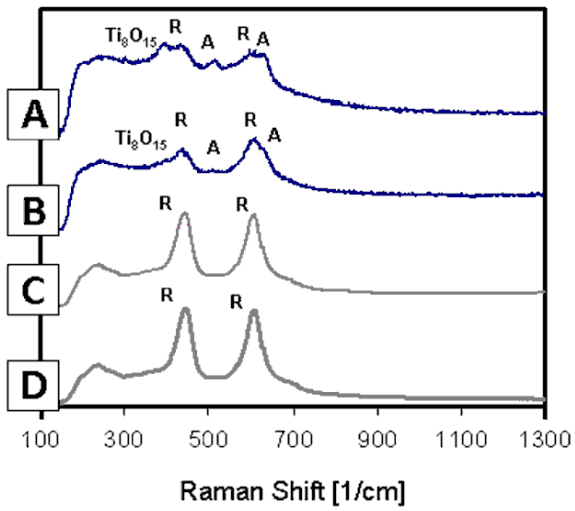

Figure 83: Raman spectrographs of the 4 coatings: (A) HVOF - as sprayed; (B) APS - as sprayed; (C) HVOF - heat treated; (D) APS – heat treated;

4.7.3 Photocatalytical Coating Response

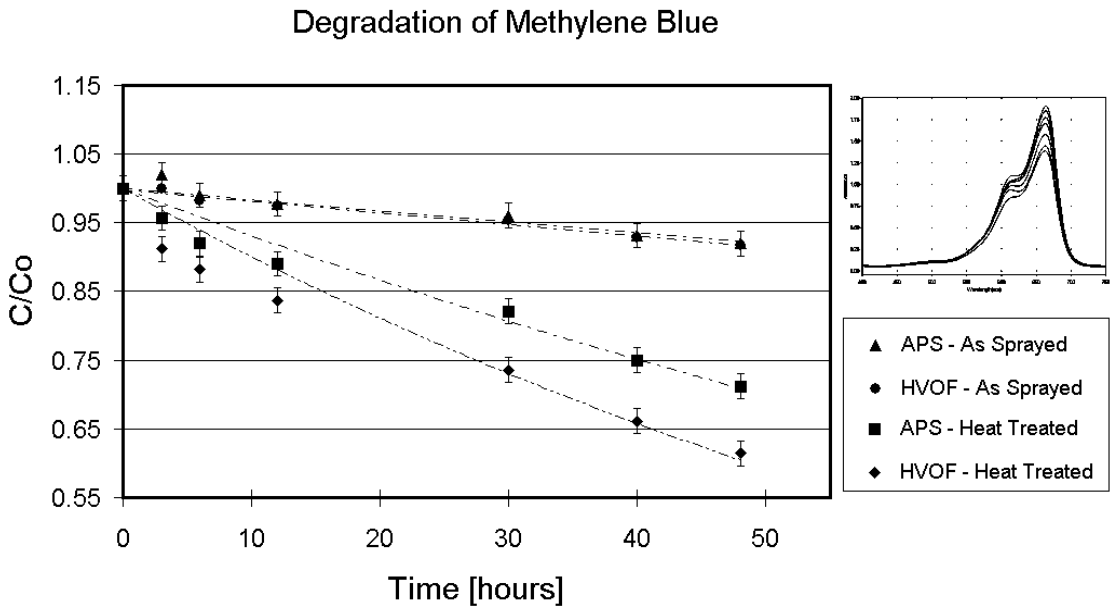

Figure 84: Photocatalytic activity in degradation of methylene blue for various coatings. Insert shows Uv-vis spectra of APS-heat treated sample as a function of time

The photocatalytic degradation testing results (carried out as explained in section 2.4.4) are shown in Figure 84. All coatings exhibited varying degrees of activity in the degradation of methylene blue under UV light. The results can be described by first order kinetics, with the rate constants shown in Figure 85. The as-prepared coatings did not show significant photocatalytic activity, with a negligible difference between the HVOF and APS coatings. However, heat treatment of the coatings resulted in a significant increase in photocatalytic activity. Moreover, the heat treated HVOF sample was significantly more active than the APS sample. These results correspond well to the material characterization described above. Given the partially reduced character of as-prepared APS and HVOF coatings it is reasonable to explain the poor photocatalytic activity of the coatings by the presence of oxygen vacancies acting as charge recombination centers[160].

It is also plausible to suggest that the positive effects of charge separation on photocatalytic activity observed for Ti_2O_3/TiO_2 interfaces[162] are not present for Ti_8O_{15}/TiO_2 interfaces present in these coatings. However, when fully oxidized, the anatase content of the coating begins to play a dominant role in determining the catalytic activity. This is consistent with the HVOF coating having the highest anatase content, as indicated by XRD and Raman results, and the highest activity, while the opposite is true for the APS coating. One important point to highlight in this discussion is that reoxidation might lead to a significant reduction of anatase content, leading to tradeoff between elimination of oxygen vacancies and transformation of anatase to rutile

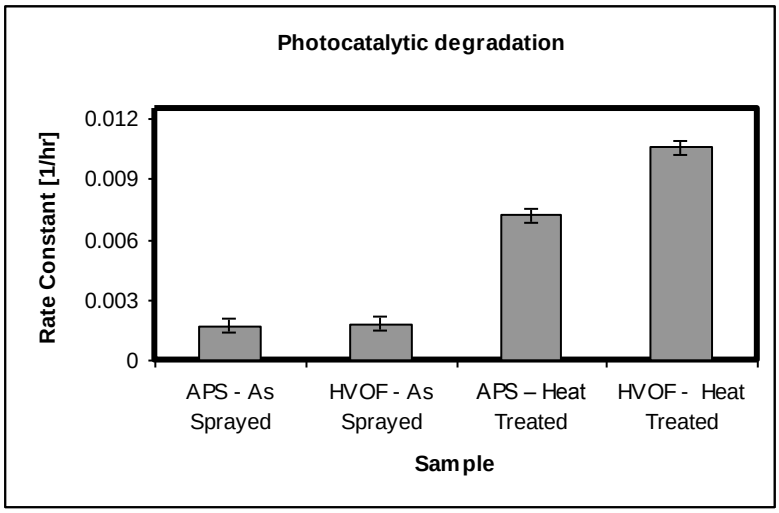

Figure 85: Rate constants of photocatalytic degradation for various coatings

4.8 Conclusions

- The interplay between phase stability issues and processing induced stoichiometric losses in titanium dioxide has been analyzed from a process map perspective. Less reduced coatings with lighter surface coloration and lower resistivities were also found to be more anisotropic in their electrical behavior likely due to the lesser level of penetration of stoichiometric reductions

- Pathways to coating phase selection given particle melting state and kinetic energy and subsequent influence on coating flattening and cooling rate have been proposed as the defining factors of the metastable content in the system.

- Additional dependency on splat size has been observed with raman spectroscopy and confirmed by the application of liquid feedstock coatings with smaller splat sizes as conventional coatings.

- Atomization of the liquid feedstock was observed to be the main driver in differences of deposition efficiency in APS and HVOF precursor/suspension spray techniques

- Residence times in the hottest zone of the spray plume have been observed as the main driver of coating stoichiometric losses and changes in electrical properties. Experimental analysis of coatings with different processes and process conditions was complement with a theoretical analysis of the principles driving the loss of oxygen in TiO_2 at high temperatures and low oxygen partial pressures

Chapter 5. On the role of particle state and non-particle state parameters and their influence in evolving stress of TiO_2 coatings

Residual stress levels in thermally sprayed coatings will have a direct consequences in the coating mechanical responses to cyclic loads, impact and adhesion in general[166], being a known fact in thermal spray science that the residual stress levels are correlated with –*althought not necessarily causal of*- microstructural features and intersplat bonding quality[167]. Residual stresses evolution, whose fundamental principles were described in section 2.3 of this manuscript are known to be dependent on particle state at impact. For example, in the case of HVOF were particles have a much higher kinetic energy compressive deposition stresses can be introduced given plastic deformations of the particle to surface impact[90].

A process map based systematic approach to understand the effects of particle state manipulation on coating evolving stress has already been carried out in Stony Brook with the use of different spraying techniques[65]. This section seeks to contribute to this previous work introducing a ceramic material (TiO_2) to a similar systematic approach, given that Valarezo's work was based in metallic and cermets materials such as WC-Co or NiCr that will not be as prone to stress relieving microcracking during splat solidification[87]. Additionally the core of Valarezo's work focused on high velocity process while the present manuscript is more centered in the study of plasma spray deposition phenomena.

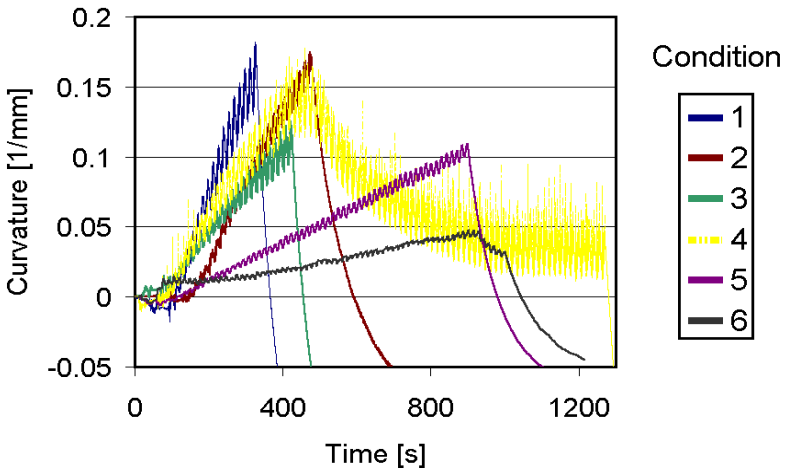

Figure 86: Curvature Evolution of Plasma Sprayed TiO_2 coatings

APS coatings sprayed in conditions 1 to 6 of Table 6 were sprayed in 3.2 mm thick aluminum ICP sensor substrates to measure evolving stress during deposition, the curvature vs. time response can be observed in Figure 86. Samples where sprayed with

the aim of obtaining similar coating thicknesses in the range of 500 µm. Given the differences of deposition efficiencies obtained with different particle states the time lengths required for such thicknesses varied from 300 to 1000 seconds. From Figure 86 it can be observed that a wide range of curvature levels was obtained, having condition 1 (Ø8 mm nozzle higher energy plasma) with the highest curvature-time slope and condition 6 (Ø5 mm nozzle lower energy plasma). For two conditions 6 and most noticeable 4, the curvature evolution presented a sudden change of slope from increasing to decreasing curvature over time suggesting the appearance of a stress relief mechanism after a certain number of passes. This phenomenon will be detailed in section 5.1.2, but for now the calculations of evolving stress will be based on the increasing section of the plot with increasing curvature, before the stress relieving behavior appears.

Another important observation is that no initial adhesion "first-pass" effect[65] was observed on which the first coating layer exhibits a higher level of bending than the rest given a bonding with the substrate, the absence of this phenomena is expected to be caused by the microcracking of the splats at impact which is independent of the number of passes carried out during the process, an detail of the initial steps of the curvature evolution graph can be observed in Figure 87

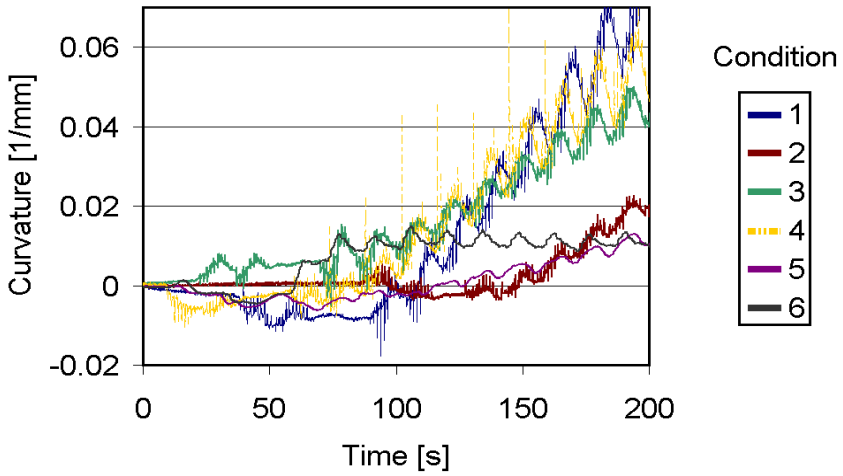

Figure 87: detail of the first steps of the curvature evolution of the different TiO_2 APS conditions

To better access the effect of particle state on evolving stress a second order process map was constructed as shown on Figure 88. It can generally be observed that conditions 1 and 4, which consist in higher energy plumes than the other conditions have a significally higher level of evolving stress, this agrees with the accepted principle that higher melting degrees will result in better inter-splat bonding creating a higher level of quenching curvature and stress, as evidenced by the coating microstructures shown in Figure 41 and Figure 42. The increase of particle velocity results in a distinguishable decrease of the

slope representing the evolving stress. This is likely caused by the decrease of dwell time on the hot zone of the plasma resulting in a deterioration of molten content as evidenced in the microstructural observations. This result indicates that such an increase in kinetic energy for plasma spray ceramic particles does not result in a significant increase of the flattening of the particles in order to achieve a noticeable higher level of splat quenching stresses. For this study the contribution of increased velocity on peening stressed is disregarded, since a brittle ceramic material as TiO_2 should not exhibit compressive hardening and densification due to impinging forces. The effect of substrate temperature is also an important factor in defining coating residual stress levels that cannot be overlooked [168], the two higher energy conditions (1 and 4) also resulted in higher substrate temperatures given the higher heat transfer from the gas stream. This increase of substrate temperature of about 75 °C compared with the colder conditions will contribute to the effect of particle state to the observed evolving stress trend. The hotter conditions allow for a slightly better spreading and bonding of the splats that contribute to coating stress build up.

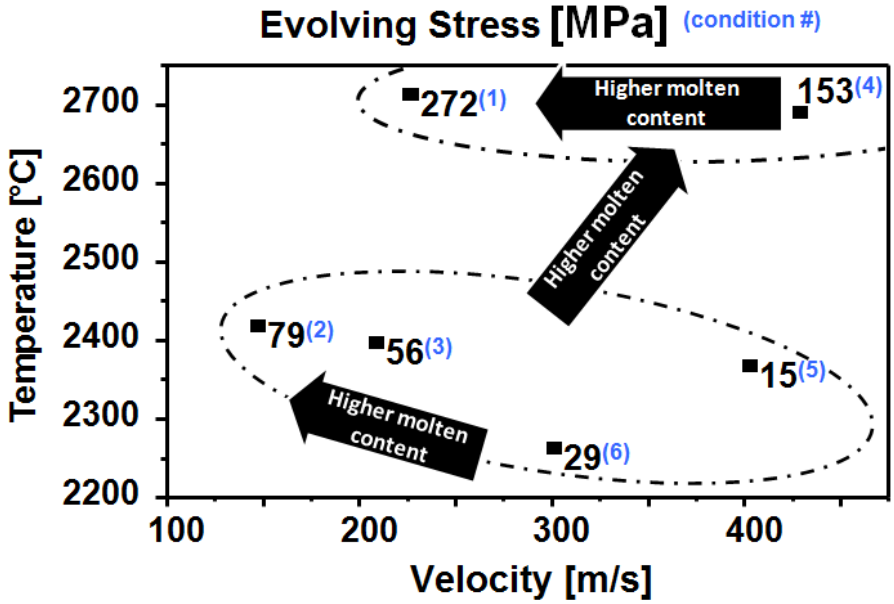

Figure 88: Second Order Process Map of plasma sprayed TiO_2 evolving stress

The coating elastic modulus was also a subject of this study, since it is known to be correlated with coating microstructure and is also relevant to the system mechanical response [169] modulus was calculated by using the cooling stage of the curvature temperature plot after deposition as explained in section 2.3 of this manuscript.

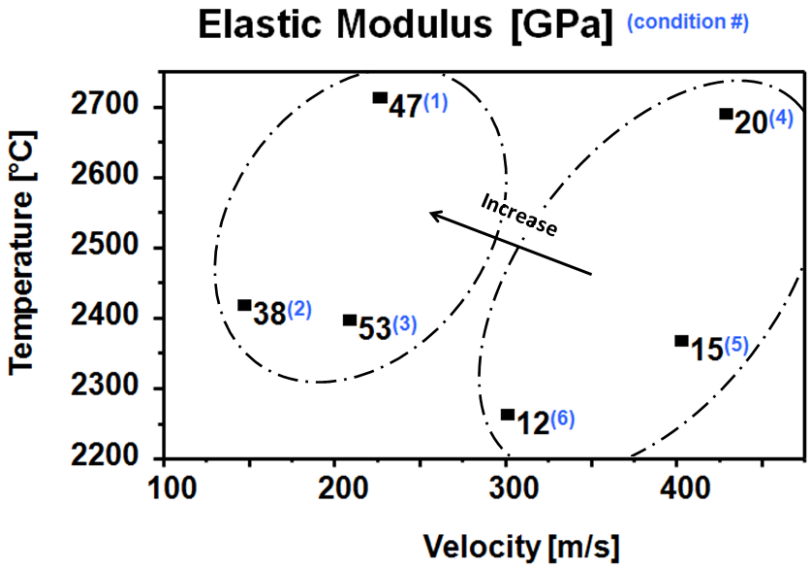

Figure 89: Second order process map of coating elastic modulus calculated by ICP

It can be seen from the second order process map of Figure 89 that the response of elastic modulus to particle state variations in atmospheric plasma spray is not as clear as the response of evolving stress. Athough the temperature effect is not as obvious, the lower particle velocities did result in a higer coating modulus. The explanation for this phenomena is identical to the explanation of the evolving stress response: lower velocities result in a better melting of the particles, a better melting state also means a better inter-splat bonding and less porosity[170] which results in a stiffer coating given the solid cohesion between splats. Again this trend is confirmed by microstructural observations.

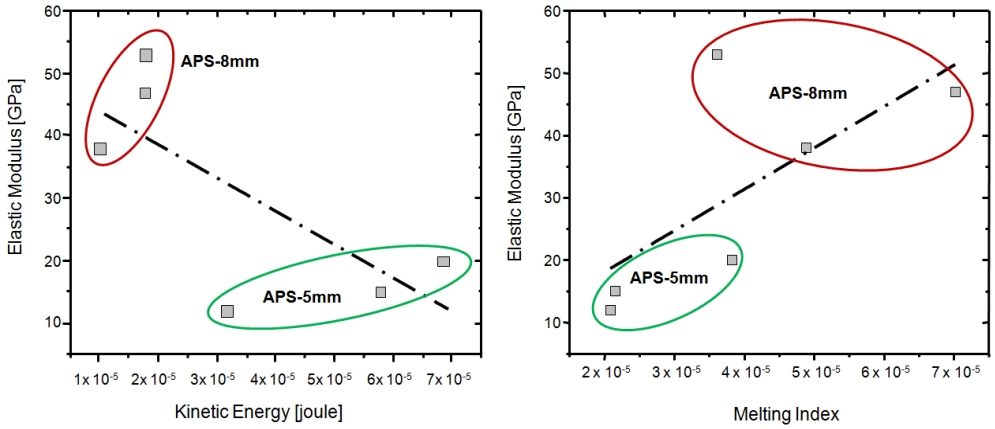

Figure 90: Elastic modulus as a function of melting index and kinetic energy

From Figure 90 it can be observed that melting index and kinetic energy indicators also present similar trends as the listed from the above paragraphs, a higher kinetic energy

results in lesser splat bonding and porosity for APS coatings given the lower residence time, while a higher melting index indicates higher bonding and structural integrity.

5.1 Non-particle state parameters and their effect on coating evolving stress, modulus and microstructure

As previously mentioned in this manuscript, particle state is far from being the only defining parameter in coating formation mechanisms, substrate temperature for example, is very well know to define morphology of an impinging splat, either because of the effect on the surface absorbate content[171] or because it affects the kinetics of the splat solidification process[172]. Another key parameter in controlling the thermal spray; which is understood to a lesser extent; is the feedstock amount in mass per unit time supplied during processing to the coating, better known as the *feed rate* in industrial jargon. The powder feed rate, as most parameters in this intricate process is hard to isolate as an independent variable for scientific study.

For example, if the amount feedstock input into the flame/plasma plume is modified, this will certainly change the amount of heat absorbed by the particles creating a *quenching* effect decreasing the overall particle temperature or melt content[173, 174]. Other possible effects of feed rate modification are a change of particle/flame chemical interaction, since a larger amount of particles could, for example, inhibit the overall oxidation of a metallic feedstock, given that the same amount of energy and oxygen would be available per unit time for a larger supply of material, although this direct effect on chemical interaction has not been proven, there is work indicating the positive effects of increasing feed rate on reducing coating oxide content[175].

Another known key parameter in defining thermal spray coating properties is the transversal velocity of the torch during deposition or robot *raster speed*. The importance of this variable relies that it's not only an alternate way to control the mass input of feedstock to the coating per unit time per unit area (slower torch traduces into a higher amount of powder) but it also has major implications in heat transfer to the substrate during deposition. If the raster speed is low, the heat amount that the substrate can dissipate by convection to its surroundings will be much lesser compared to the heat intake, causing an increase in substrate temperature[62].

With a the proper experimental design, the influence of feed rate and raster speed can be combined to analyze their individual and combined effects on coating formation and properties. The combined effect of feed rate and raster speed is known as deposition rate. It has been proposed as a major factor in controlling residual stress in the coatings[176] and also has been the subject of intensive study at Stony Brook CTSR given the new

developments in real-time coating curvature/stress measurement[5]. Deposition is defined in this work as:

$$DepositionRate\left[\frac{mass}{lenght}\right]=\frac{FeedRate\left[\frac{mass}{time}\right]}{RasterSpeed\left[\frac{lenght}{time}\right]}$$

Which results in a rather unexpected unit of mass/length definition, but if we correlate the amount of shrinking (or quenching stress) during solidification with the amount of mass sprayed, the deposition rate could be loosely related to the strain energy per unit length of coating deposition as it will be observed later in this chapter.

5.1.1 Parameter Selection

To study the effect of feed rate, raster speed and deposition rate process map was designed based on a 2 x 2 +1 experimental square design, as shown in Figure 91. The limits of the DOE were based for the raster speed on previous expertise on (a) avoiding extreme speeds too low to keep the substrate for overheating and (b) speeds too fast to possibly damage the robot and hardly achieve coating deposition. For the feed rate selection a similar criteria was used in choosing feed rates that were not too high to clog the injecting nozzle or quench the torch excessively and feed rates too low to achieve extremely reduced thickness/pass

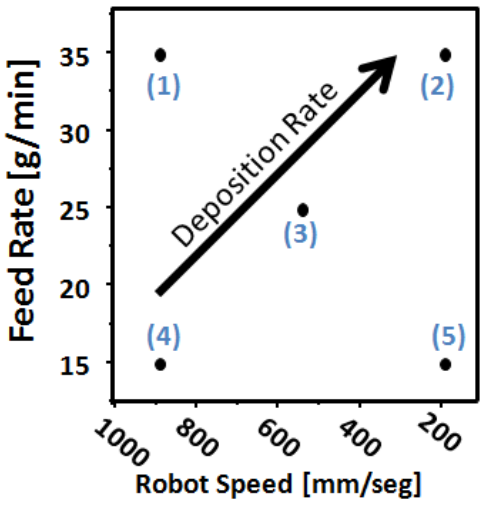

Figure 91: experimental design for deposition rate process map

The torch parameters where kept constant during this series of studies, but the particle state cannot be guaranteed to have remained constant, since changes in feed rate will affect the particle-plume interaction as mentioned above. When particle state was

measured at low feed rate before each experiment (at 2 gr/min feed rate) in Figure 92 the results can be seen in context of the previous chapter extended process map of section 4.1, and also shown are similar particle temperature histograms, which demonstrate the negligible variability of plume heat and gas momentum on during the experiments

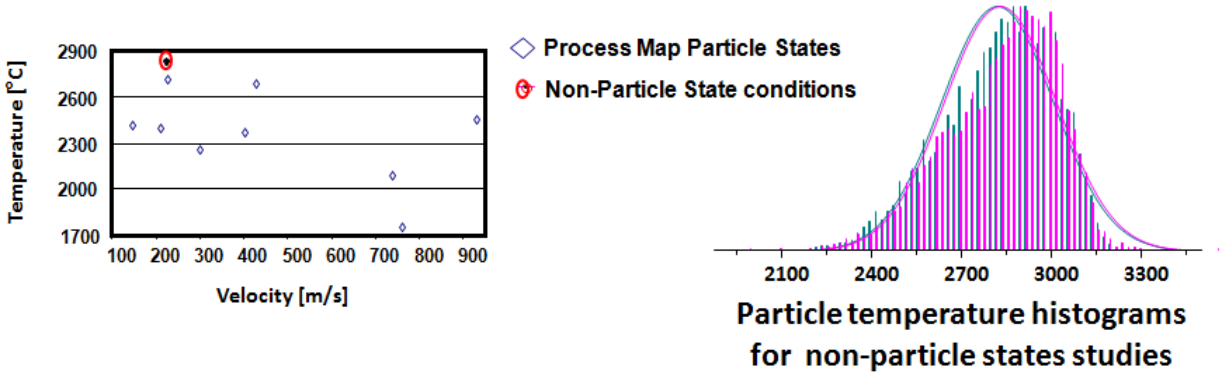

Figure 92: Particle State for deposition rate experiments (a) in context of extended process map (b) temperature histograms

5.1.2 Influence of Deposition Rate on Evolving Stress, Microstructure and Modulus

As expected, the different combinations of feed rate and raster speed resulted in significantly different substrate temperatures, with the highest feed rate and slowest speed condition resulting in the hottest substrate temperature. The same effect is obtained with the final residual stress of the coating calculated from the change of curvature between the start of the coating and the end of the cooling process with the measurements of the ICP. This dependence on substrate temperature is also expected, since a higher temperature during deposition results in a larger mismatch stress during cooling. The thickness per pass also resulted as expected, with higher thickness/pass in the higher deposition rates as shown in Figure 93.

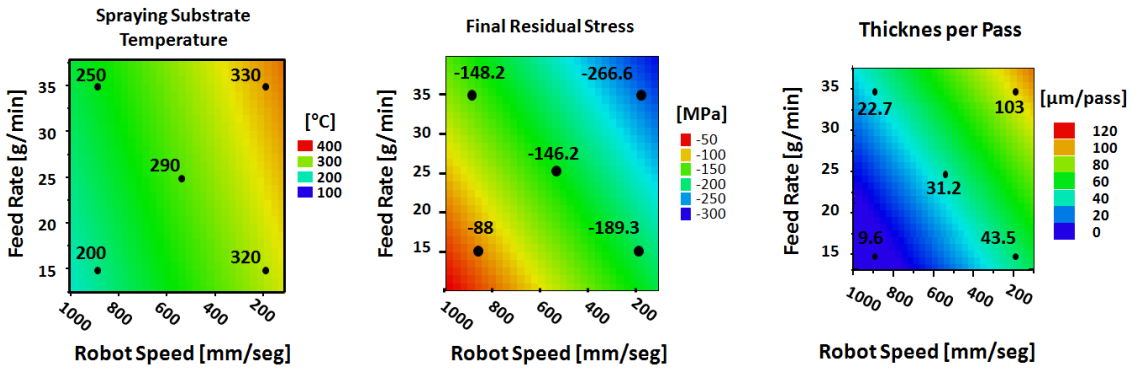

Figure 93: response of deposition rate experiments

When observing the coating cross-section for microstructural characterization, a lesser understood phenomena is observed in Figure 94: the appearance of vertical and horizontal cracks in the coatings with a higher deposition rate. The presence of this cracks has been previously related to excessive residual stress in the coating[177],and when the cracks are limited to vertical orientation, such as in the industrially denominated *segmented* or *dense vertically cracked* coatings, this stress release mechanism is considered positive since it gives the coating higher level of compliance [62] which is necessary to extend the coating life time for high temperature applications.

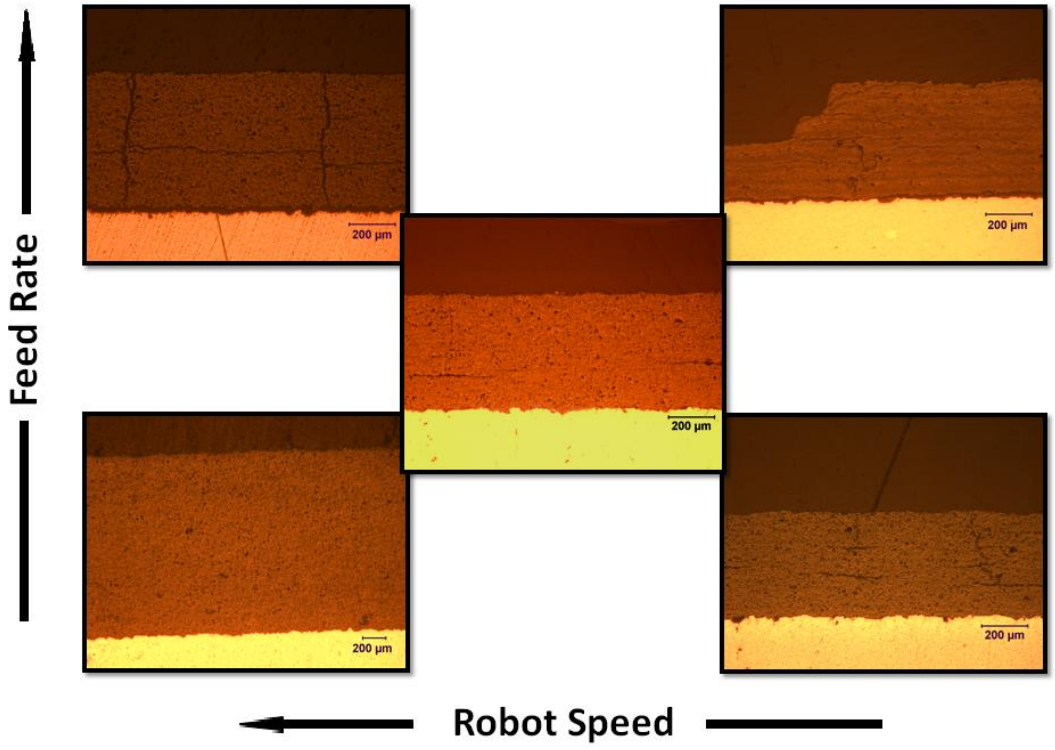

Figure 94: microstructures of deposition rate experiments coatings

Many questions are still open regarding the formation of vertical or horizontal stress release cracking in thermal sprayed coatings, in the present work the application of the ICP for curvature and evolving stress during deposition shreds some light in the issue as it can be observed in Figure 95 where the curvature-time curves are presented adjacent to the resulting microstructure

In the high feed rate and high robot speed combination condition, it can be seen from the curvature plot that initially the curvature increases caused by the quenching stresses, but later, there is a change on the slope of the curvature curve which is suspected to be caused by the appearance of cracks

For the highest deposition rate condition (low speed, high feed rate), the same behavior is observed after the first pass in the curvature vs. time plot. delamination occurred subsequently during the cooling time as the red circle points out (this was verified by the operator while observing the coating cool down)

For the lowest deposition rate condition (low feed rate, high robot speed) no cracks appeared even with a higher coating thickness, and the curvature kept rising during the complete coating process without any changes in slope

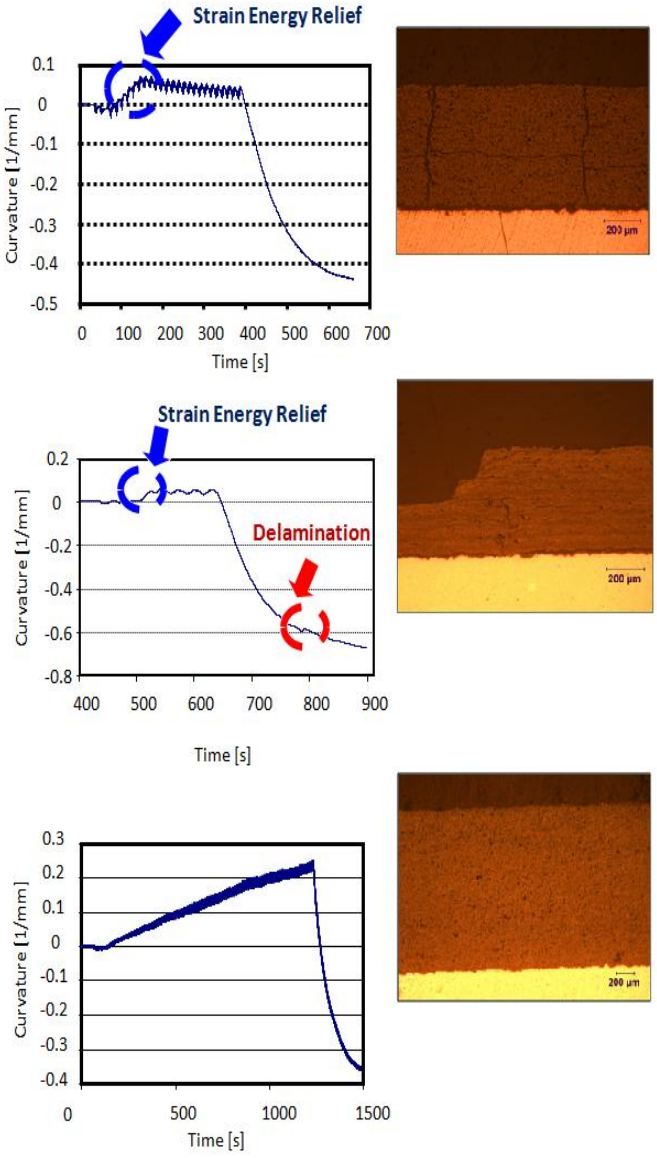

Figure 95:curvature evolution for selected deposition rate experiments

For the deposition rate experiments, the newer and precise ex-situ curvature measuring technique was applied to carefully monitor the curvature-temperature response of the coatings under thermal loading. Such technique -explained in section 2.3.1- was still under development for the previous section regarding extended first order process map.

Given the slower rate of heating in a controlled environment, a much clearer definition of the curvature-temperature plot can be constructed allowing for precise measurements of coating modulus. Figure 96 shows presents the influence of deposition rate parameters on coating modulus as measured by ECP. It can be observed that the lower deposition rate condition results in the lowest elastic modulus of the coating. The highest deposition rate modulus could not be determined as this coating delaminated during cooling in the spraying process, the middle deposition rate condition coatings do not have a clear trend but the modulus seems to be slightly higher in both low robot speeds or high feed rates condition that in the standard center point.

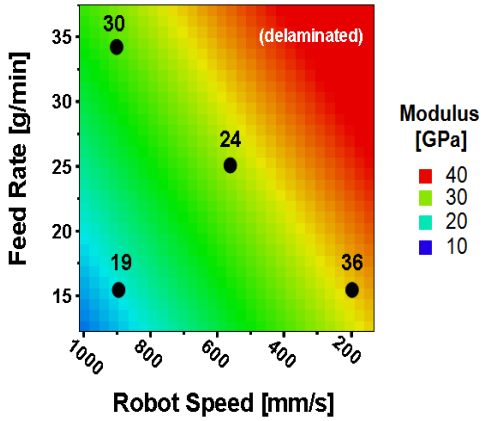

Figure 96: ECP modulus of deposition rate experiments

The differences in deposition rate young modulus although subtle, do provide two important observations:

(1) The non-cracked coating (low deposition rate) that could be expected to be the stiffest given the lack of compliance enhancing cracks, actually results in the lowest Young Modulus.
(2) The higher feed rate coating, which should have slightly colder particle state given the higher mass flow for a constant torch energy input, does not result in more compliant coating; in the previous section it was shown that significant colder particle states result in lower elastic modulus given the increase of porosity and poorer bonding.

The observations point out that the defining mechanism of coating stiffness for different deposition rates is not particle state or compliance enhancing cracks, there is another important difference not previously taken into account in this study which is the difference in thickness/pass for each conditions, which in more precise scientific jargon is a measure of the *density of interfaces between coating layers* or passes.

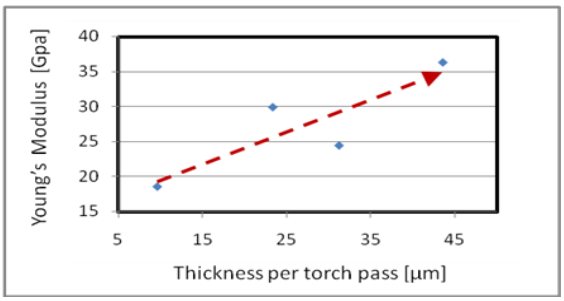

Figure 97: Effect of thickness/pass on coating elastic modulus

From Figure 97 it is inferred that a higher thickness per pass on this experiment series results in a higher coating modulus. A proposed explanation for this phenomenon is that by increasing the thickness per pass, the number of splats impacting per unit area per unit time is also increased. The results suggest a more coherent bonding between the splats deposited in a single pass than between splats deposited in multiple passes. On the microstructure schematic of Figure 98 this supposition is depicted in a way where the inter-pass interfaces are highlighted in darker colors. A higher density of the "dark" interfaces could mean -given a possible a poorer bond in such boundaries- that the overall stiffness of the coating is reduced, explaining the lower elastic modulus found for the lower thickness/pass conditions.

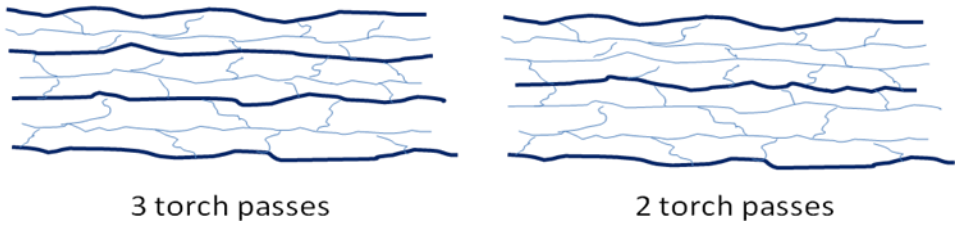

Figure 98: Schematic of effect of thickness per pass changes; the thick line represents inter-pass interfaces, while thinner line represents inter-splat interfaces

It must be emphasized, that the splats deposited in a single torch pass do not solidify simultaneously, previous authors have found that the time scale for a splat solidification is much faster than the subsequent impact of the following splat[69]. Nevertheless, the splats that solidify in a single pass do not allow for cooling of the substrate after the torch moves away, this lack of instant cooling between splat solidification could be significant enough to establish the interfacial differences suggested above. The differences in substrate temperature on splat flattening/splashing phenomena for each condition cannot be excluded for being another contributor to this phenomena, but since for all spraying conditions the substrate temperature is well above the expected splat transition temperature for TiO_2[178] and the modulus trend doesn't follow the substrate temperature behavior, this effect -if existent- should be secondary to the proposed role of interfaces in defining the stiffness of the coating.

5.1.3 Properties not affected by deposition rate

Other parameters, which had previously been proven to be dependent on in-flight particle state and torch parameters seem to be much less affected by the deliberate modification of deposition rate experiments. Two examples of this case include the Anatase content and through thickness thermal conductivity. In the case of anatase fraction, which varied from 17% to 40% in the extended process map particle state variations, only varied from 22.4% to 26.1% in the deposition rate experiment as seen in Figure 99. Although a slight trend can be observed that suggest higher anatase content at lower deposition rates the variations in the reported values still fall in line with the expected error of a standard X-ray measurement[179], this minor trend could be explained by the lower deposition temperatures and lower mass flow of powder per unit area/unit time, which should deter the transformation from anatase to rutile caused by subsequent impinging of splat over splat, but the small extent of this effect also suggest a very limited contribution of this supposed phenomena into defining the coating phase evolution.

In the case of thermal conductivity, which has reported a of a variation of 1.3 W/mK in between different processes[131] this property reports a variation of only 0.3 W/mK for the deposition rate experiments. Thermal conductivity also indicates a slight trend towards higher conductivity at low deposition rate conditions, this could be explained by coating microstructural features, since the low deposition rate experiments lack the horizontal interfacial cracks present in the higher deposition rate conditions, the role of interpass interfaces suggested earlier could also play a role.

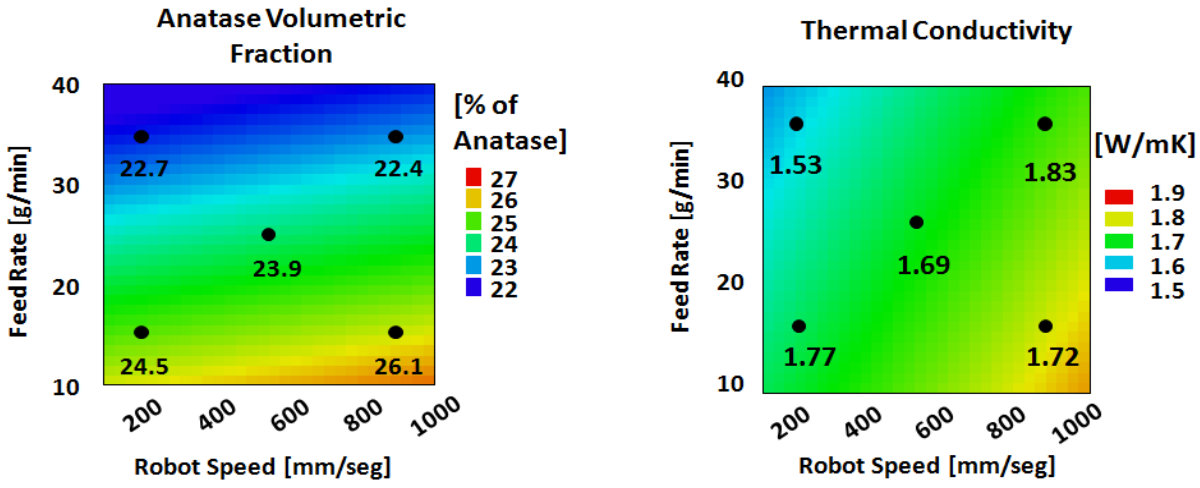

Figure 99: Effect of Deposition rate on (a) Anatase content and (b) Thermal Conductivity

5.1.4 Deposition Rate Effects on electrical properties of TiO_2 coatings

In the previous chapter the processing manipulation influencing particle state during deposition was analyzed as a method to modify transport properties of titanium dioxide coatings by altering the density of conductive interfaces located in the in-plane direction of the microstructure. This section is focused of understanding whether deposition mechanisms not related to particle state can also result in a modification of such interfacial conductive density. In section 5.1.2 mechanisms that differentiate stress build up due to changes in inter-splat and inter-pass interfacial density were discussed, a similar approach, by spraying samples with the same torch (Triplex-Pro 200) with the same torch parameters and feed as described on Table 10. These coatings were processed during a curricular practical training internship in Sulzer-Metco Westbury NY. Samples were sprayed both in insulative alumina coupons and steel substrates, the first to measure the in-plane sheet resistance with the 4 point electrical probe and the second to measure through thickness impedance as in the previous section.

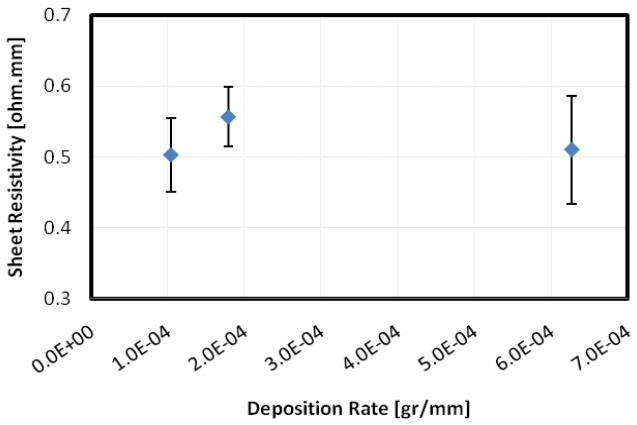

Figure 100: in plane sheet resistivity as a function of deposition rate

The measurements of sheet resistivity were performed with 2 different samples on each deposition rate measuring 5 times for each sample. The results of the measurements are shown in Figure 100 and it can be shown that the center condition of deposition rate (which is also closest to parameters industrially applied) results in the highest electrical conductivity. Nevertheless the differences reported fall in between the standard deviation of the 10 measurement for each conditions, to clarify if the difference between samples can be considered significant an Analysis of Variance (ANOVA) was performed with the original data resulting on P value of 0.250, which is above the threshold of what is considered to be a significant statistical distance between measurements (0.05).

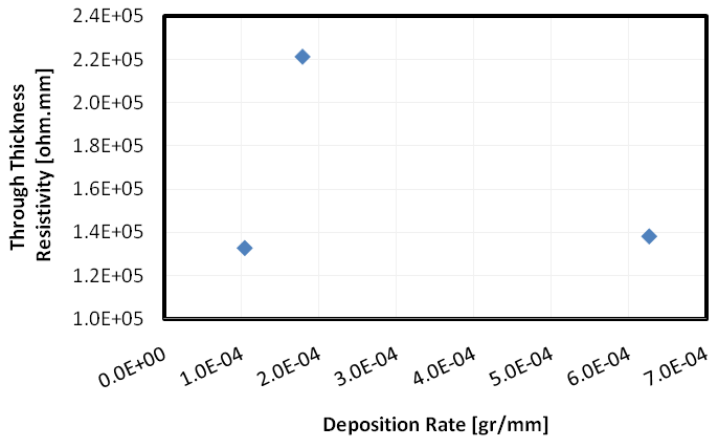

Figure 101: through thickness resistivity as a function of deposition rate

Through-thickness impedance measurements presented the same behavior reported earlier of a resistor at low frequencies only increasing its capacitive behavior at frequencies higher than 10 KHz. The calculation of resistivity based on this low frequency impedance as a function of deposition rate is shown in Figure 101, a pattern similar to the in-plane sheet resistivity measurements is observed with the center condition being more conductive in the through-thickness directions. These measurements required the dissolution of the steel substrate on an Aqua-Regia solution and a preparation of conductive paste connections to the impedance meeting with a defined area, which complicates the preparation of different samples. The differences between repeated measurements on the same sample seem to be caused only by an increase of humidity content on the sample as shown in Figure 102. For this reason all electrical measurements reported in this manuscript were performed immediately after heating the samples at 100 °C for an hour. Given the quick increase of impedance values after removing the sample from the oven an exact estimate of the standard deviation of these measurements is difficult to assess, but it is clear that the variations in values of through thickness resistivity and the anisotropy of the samples is much less significant as the changes resulting from particle state manipulation shown in section 4.6.1 of this work, which combined by the non-significant statistical analysis of the in-plane resistivity studies is a direct indication that particle state is more determining in modifying electrical transport properties of TiO_2 thermally sprayed microstructures than deposition rate modifications.

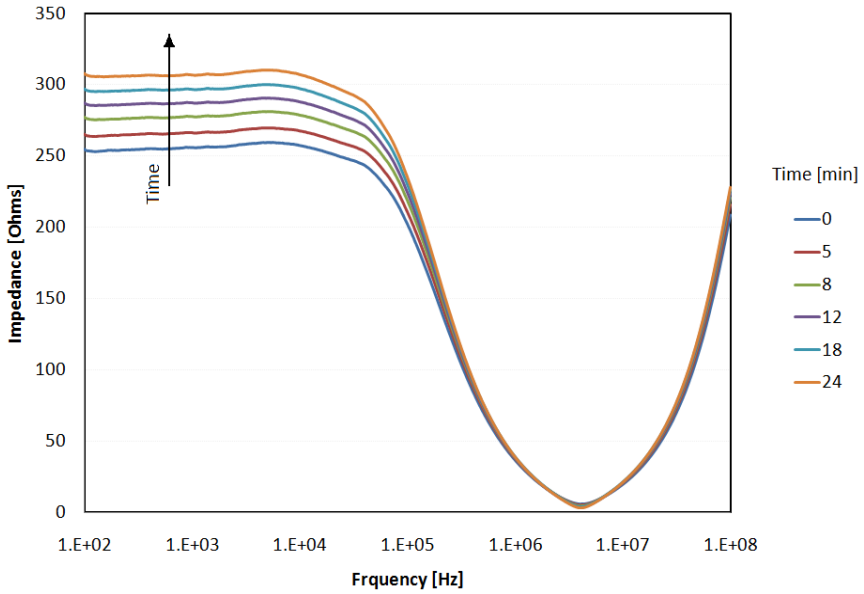

Figure 102: variations in through-thickness impedance after removing sample from de-humidifying oven

It must also be noted that geometric differences such as thickness variations between samples and even microstructural divergences in the same sample make the calculation of the coating resistivity a highly uncertain approach, even from a relative point of view [180, 181], but the differences in the impedance response of the samples, describing different behaviors in the frequency domain of the system for particle state modified samples, while resulting in very close response for the deposition rate modified samples supports our conclusion of a predominant effect of the former than the later on electrical behavior

Condition #	Parameters	Robot raster speed [mm/s]	Deposition Rate [gr/mm]
1	Current: 450 A Voltage: 126 V Argon: 50 SLPM Nitrogen: 10 SLPM Feed Rate: 15 gr/min	400	6.3×10^{-4}
2		1400	1.8×10^{-4}
3		2400	1.04×10^{-4}

Table 10: Parameters for Deposition Rate on Electrical Properties Study

5.1.5 Deposition Rate on compliant substrates

Figure 103: Photographs of samples sprayed with different deposition rates

A similar set of experiments on deposition rate was performed with a thinner aluminum substrate of 1.2 mm thickness (the previous section used substrates 3.2 mm thick), also, a coarser particle size of the same myllidine TiO_2 powder was applied compared with the previous experiments, since too fine powder usually results in denser coatings[182] , with

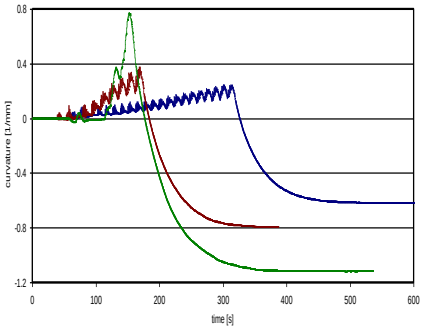

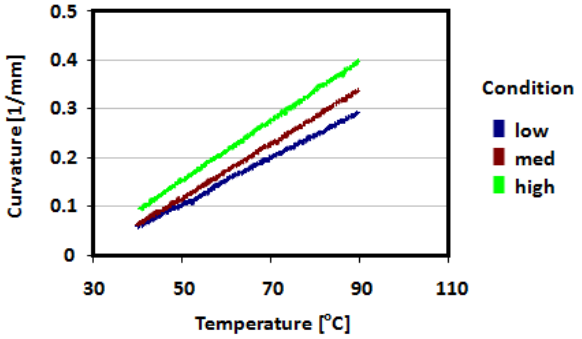

higher residual stresses and higher likelihood of stress relieving micro cracks appearing. For this series of experiments, only 3 deposition conditions were sprayed of the 5 presented in Figure 91.

(1) High deposition rate: low raster speed and high feed rate (condition 2)
(2) Medium deposition rate: medium speed and feed rate (condition 3)
(3) Low deposition rate: fast raster speed and low feed rate (condition 4)

Figure 104: Curvature evoltion of different deposition rate experiments for (a) ICP measurements and (b) ECP cooling

In Figure 104-a it can be observed that given the high compliance of the thin coatings the curvature evolution is significally higher than for the previous set of experiments (up to 0.8 m^{-1}). There is no noticeable change in curvature slope during any of the 3 conditions which suggest the absence of stress relieving macrocracks (confirmed in the micrographs of Figure 106). Figure 103z shows a photograph of the 3 different samples of this experimental series, it indicates a marked difference on final curvature levels for the three samples, with the highest deposition rate sample showing the highest bending levels

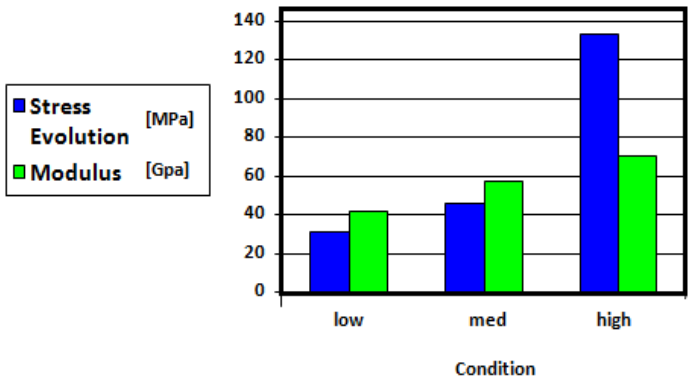

Figure 105: Computed Evolving Stress and Modulus Values for Compliant Substrate Experiments

Controlled ex-situ curvature measurements were also performed for these sets of experiments with the cooling curvature-temperature response shown in Figure 104-b were noticeable different slopes can be observed. The computed values for evolving stress and coating modulus of the coatings can be seen in Figure 105. The high deposition rate experiment also results in both the highest evolving stress and elastic modulus although the microstructure cross section microstructure (Figure 106) does not indicate major variations in porosity from the other conditions. The fact that for these experiments the higher deposition rates results not only in higher stresses but in higher elastic modulus agrees with the previous suggestion of an important role of the inter-pass interfacial density (higher deposition rate also resulted in higher thickness per pass).

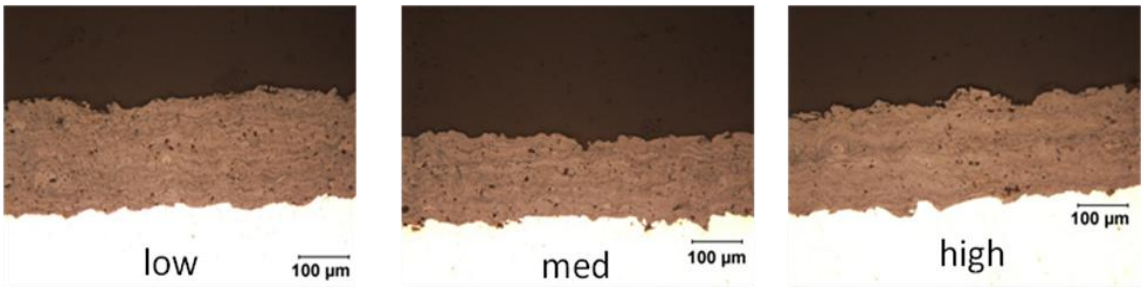

Figure 106: microstructures of different deposition rate experiment

It must also be noted that the coating elastic modulus values where consistent amongst the different steps of this study, with different levels of variation depending on the parameter manipulated. Particle state modification had the widest level of coating structural integrity changes, and the deposition rate experiments with compliant substrates resulted in the overall higher modulus, likely due to the lesser level of stress relieving micro cracks present.

Experimental Series	Lower Modulus [Gpa]	Higher Modulus [Gpa]	Modulus Variation
Particle State	12	47	35
Deposition Rate / Compliant Substrates	39	67	28
Deposition Rate / Thick Substrates	19	36	17

Conclusions

In this chapter process-property relations where studied from a evolving stress perspective, analyzing effects of particle and non-particle stress parameters in coating integrity and stress relieving mechanisms with real-time measurement techniques. The influence of particle molten status and the density of inter-pass interfaces were both demonstrated to play key roles in the buildup mechanisms of the coating from a mechanical perspective, whereas other properties related to phase evolution and transport are dictated by particle state modifications primarily, these results are in agreement with the electrical conductivity studies of Chapter 4 which suggested a major role of particle state in the de-oxidation of TiO_2 and a minor role played by deposition rate for electrical transport mechanism. The mechanism proposed suggesting intrinsic differences between inter-splat and inter-pass interfaces controlled by deposition rate effects have been proven a defining factor only for stress related issues as shown in Figure 107.

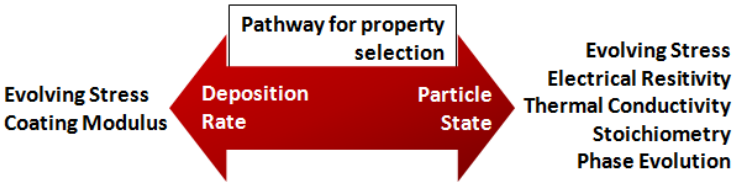

Figure 107: Reconciliation of evolving stress studies and deposition rate effects with other properties studied in this work and their influence by particle state.

Chapter 6. Luminescence of Alumina-Chromia Flame Sprayed Coatings optimized by

Previous studies of Alumina-Chromia Thermal Spray applicability performed in Oakridge National Lab had indicated that the flame spray method is the optimum technique to achieve ion bombarding fluorescence, since methods like HVOF, APS, Detonation etc resulted in little or no photon emissions. The Oakridge team also optimized the Chromia content on the feedstock powder to 1%, the results of a trial test with different methods/compositions can be observed in Figure 108.

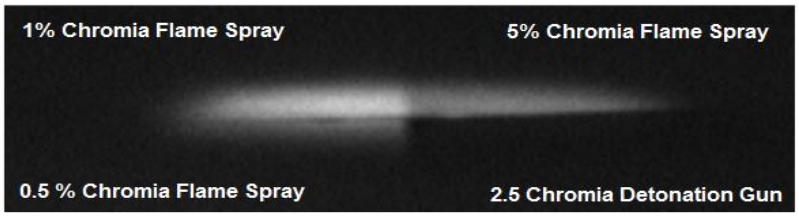

Figure 108: Previous findings of the feasibility, optimum Cr_2O_3 concentration and best method for target coating. (Adapted from[52])

The optimum crystalline structure of such scintillating coating is Ruby, a crystalline dilute solid solution of chrormia in the thermodynamically stable α-alumina[183]. Since the thermal spray will normally result in the metastable gamma phase given the rapid solidification intrinsic to the process, the results observed by the Oak Ridge team are not surprising. Flame Spray, being the method with the lowest flattening of the particles has the lowest solidification rates of all the thermal spray techniques, presumably resuls in a higher content of α phase. This study applied a process map strategy to analyze the influence the diverse parameters that will influence coating morphology, phase evolution and ultimately fluorescence as a functional coating property.

6.1 Experimental Approach

This work summarizes 3 stages of the coating development process, the first consisted in a exploratory study of process conditions and the effect on coating fluorescence with different chromia contents, The second step focused on the study of a the influence of substrate temperature during spraying by manipulating different spraying parameters and the last step included the utilization of particle state sensors and in-situ evolving stress monitoring to better understand the influence of such parameters on the coating formation mechanisms.

In the first stage, the variables studied consisted on the mass percentage of chromia additive to the alumina blend and the spray distance of the torch during processing. The torch gas flows were kept constant at 26 slpm of acetylene and 36 slpm of oxygen. The torch nozzle was also modified for one of chromia content conditions to access the effect variations in gas flow geometry as observed in Table 11, it must be noted that these preliminary spray runs were performed with a hand held spray torch.

Spray Distances [inch]	4, 6 and 8
Chormia Blend Mass %	0.5, 1* and 5
*Spray Nozzle	RL3310 for all conditions, for 1% chromia content an additional experiments with the RL210 Nozzle were carried out

Table 11: experimental variables modified in the exploratory stage of the fluorescence study

In the second stage, torch gas flows and spray distances were manipulated as well as the raster speed of the robot mounted spray torch and the presence of cooling air during spraying with the aim of observing the effect of these parameters on coating fluorescence. During this series of experiments with variables shown in Table 12 the substrate temperature was monitored with a contact thermocouple in the back of the sample.

Sample #	Oxygen Flow [slpm]	Fuel Flow [slpm]	Spray Distance [inch]	Robot Raster Speed [mm/s]	Sample Cooling Air
A1	30	23	8	750	Yes
A2	30	23	6	750	Yes
A3	40	31	4	750	Yes
A4	30	23	6	500	No

Table 12: experimental design for the second stage of the study

Powder size distribution and pre-treating influence was also analyzed given the experimental design shown in Table 13 to assess the influence of feedstock material characteristics on coating fluorescence.

Condition	Powder Size	Pre-Treating
A5	16	1200 °C for 6 hours
A6	16	No
A7	49	No
A8	49	1200 °C for 6 hours

Table 13: experimental design for feedstock influence of coating fluorescence, all coatings sprayed with 30 slpm of O_2 and 23 slpm of acetylene at 6" stand off distance

The last stage of the study consisted on an experimental design modifying particle states with the use of torch gas flows, maintaining constant the robot raster speed of 600 mm/sec and actively controlling the cooling air flow to keep the substrate on a temperature of 110 +/- 10 °C. The experimental design for this stage of the study can be observed in Figure 109 and the powder used contained 1.5 % chromia with the previously described pre treatment of 1200 °C for 6 hours with the goal of obtaining pre-diffused Cr ions into the alpha alumina structure. This part of the study also included the use of particle state monitoring sensors (DPV2000) and the use of the in-situ curvature-sensor

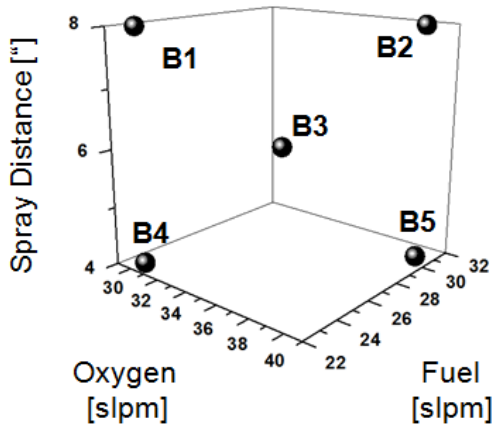

Figure 109: experimental design for 3rd stage of the experimental series

For all experimental series other important parameters such as powder feed rate were kept constant for experimental consistency as shown in Table 14, Fluorescence of sprayed samples was measured by placing the samples in a beam dump with energy levels similar to the intended application of the target. The intensity measurements were normalized from arbitrary detector units to a fraction of the fluorescence of a reference pure ruby sample.

Robot Raster Speed*	Powder Feed Rate	Oxygen Supply Pressure	Acetylene Supply Pressure
500 mm/s	20 gr/min	50 Psi	15 Psi

Table 14: parameters kept constant during the alumina-chromia fluorescence study

6.2 Experimental Results and Discussion

6.2.1 Effects of Chromia Content and Spray Distance on Fluorescence

Figure 110 shows the values of normalized fluorescence for different spray distances and different contents of chromia on the alumina blend. It can be observed that the 5% chromia coatings present the higher luminescence at six inches spray distance of all the samples, the effect of spray distance is not clear since a longer standoff position of the torch seems to improve the fluorescence for the 1% coatings with the RL210 nozzle coatings and the 0.5 % chromia coatings while worsening for the 1% with the RL3310 nozzle.

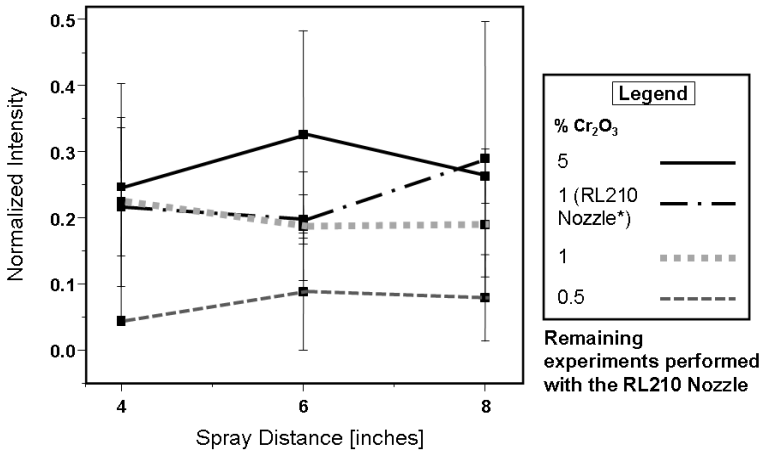

Figure 110: fluoresecence measurement of the exploratory studes normalized to a standard ruby sample

Given the lack of a clear cause for the optimum fluorescence of the aforementioned result and no consistent trends observed with chromia percentages and spray distance the following steps were carried out with the use of a robotic spray system that eliminates deposition variations due to changes in gun raster speeds and assures a more uniform heat input into the substrate from the torch combustion gases.

6.2.2 Effects of process parameter, substrate temperature and feedstock characteristics on coating fluorescence

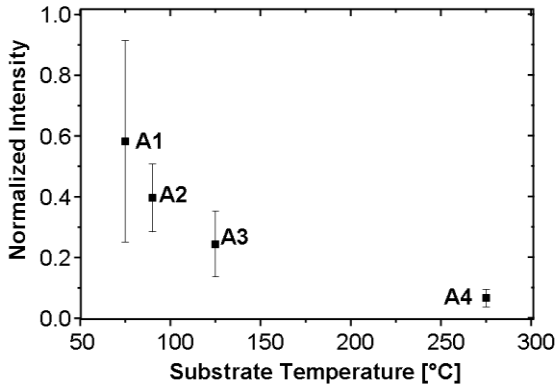

Figure 111: Intensity of coatings as a function of substrate temperature

In Figure 111 the fluorescence results of the coatings sprayed with the parameters listed in Table 12 clearly indicates that an increase of substrate temperature correlates with a lower fluorescence of the samples. The fact that conditions A2 and A4 both are sprayed with the same torch gas flows but with different robot raster speeds and sample cooling conditions suggest that fluorescence variations are not only due to intrinsic in-flight melting state variations but also by changes in the solidification mechanisms of the particles after impact. It is well understood in thermal spray science that a higher substrate temperature improves the uniform flattening of the molten droplet resulting in a higher solidification rate[168, 184]. Consequently higher content of the less fluorescence gamma crystalline structure would be expected for condition A4. The results of this second stage of the study although enlightening suggested that a more in-depth process map oriented study to clarify process and fundamental implications of fluorescence variations was needed. From figure 4 it can be observed that the highest fluorescence results on the non pre-heated samples with the coarser particle size, the coarse particle size will difficult melting allowing for a higher content of semi-molten particles retaining the original structure of the unmolten core.

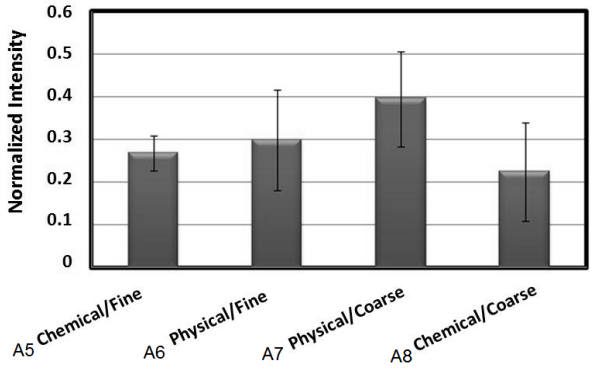

Figure 112: effect of feedstock characteristics on coating fluorescence

6.2.3 Process Map and the relation with coating buildup and solidification mechanisms

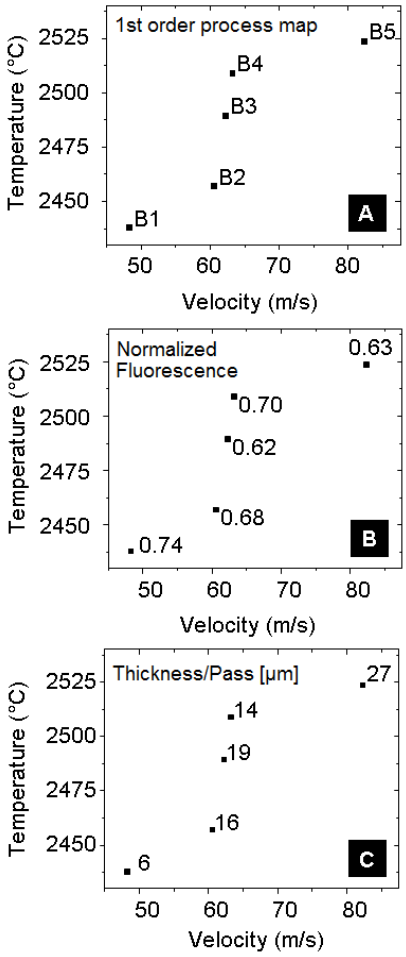

Figure 113: A) first order process maps of flame sprayed alumina-chromia coatings B) Second order map of normalized fluorescence C) Second order process map of thickness per robot pass during spraying

The first order process map of particle state shown in Figure 109-A indicates that a lower total torch gas flow and a higher spray standoff distance result in lower particle velocities and temperatures, this result is not surprising given that the higher gas flows will impart more acceleration to the particles and result in higher combustion enthalpies. The second process order process map of fluorescence indicates that the lower temperature/velocity condition (B1) resulted in the highest fluorescence of all the samples. A lower particle temperature at impact usually results in lesser splat flattening[170] and lower solidification rates which could induce a higher degree of retaining of the original stable gamma phase of the particles.

The second order process map of deposition efficiency (or thickness per pass) of the coating shows a steep decline for the lower energy condition B1 which is a clear

indication that fewer particles are being molten and likely the coating deposit is comprised of partially molten particles, which could explain the higher fluorescence given the retaining of the original alpha phase in the core of the splat.

The real time analysis of curvature evolution of the coatings resulted in a significantly lower curvature change compared with other thermal spray deposition methods. Figure 114 overlaps the curvature evolution of condition B9 (Flame Sprayed) with reference examples of pure alumina HVOF and APS coatings. This is explained given the lower kinetic energy of the flame sprayed technique results in lower flattening of the particles at impact resulting in less quenching stress accumulation during solidification.

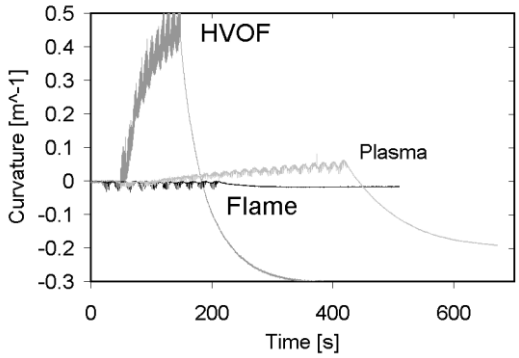

Figure 114: comparison of curvature evolution of the flame sprayed coatings studied in int this work with example APS and HVOF sprayed alumina coatings

All the process map B conditions exhibit scarce quenching stress buildup during deposition as shown in Figure 115, but after deposition finishes the mismatch in thermal expansion coefficients during cooling combined with the higher thickness of the substrate constrains the thinner coating layer into a final compressive residual stress state[93]. This compressive behavior is much lesser pronounced for the B1 condition, which is an indication of the poorer bonding between splat lamellae allowing for mechanical compliance during cooling, this observation agrees with the significantly lower deposition efficiency of condition B1 confirming the interpretation of a higher percentage of unmolten or semi-molten particles in the coating

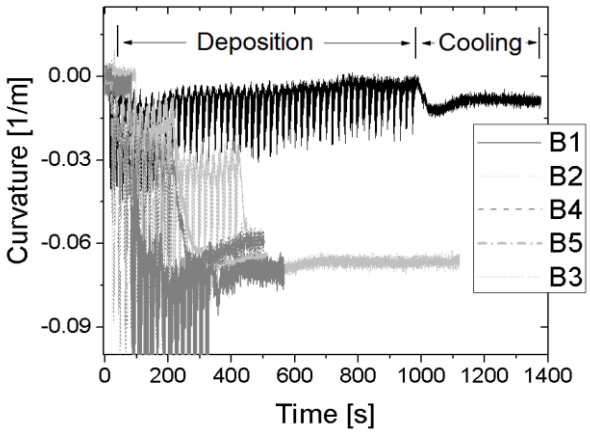

Figure 115: Curvature/Evolving Stress for different process map samples

6.3 Coating Characterization

To confirm our previous assumptions on the effect of particle state on the fraction of the stable α phase and fluorescence response spectroscopic characterization was carried out using both x-ray diffraction and Raman microespectroscopy. The map of a coating cross section Figure 116 represents the intensity of the alpha alumina wavelength intensities; it shows that there are specific locations of alpha alumina particles, presumably unmolten that are kept together by the molten and resolidified gamma phase as a binder.

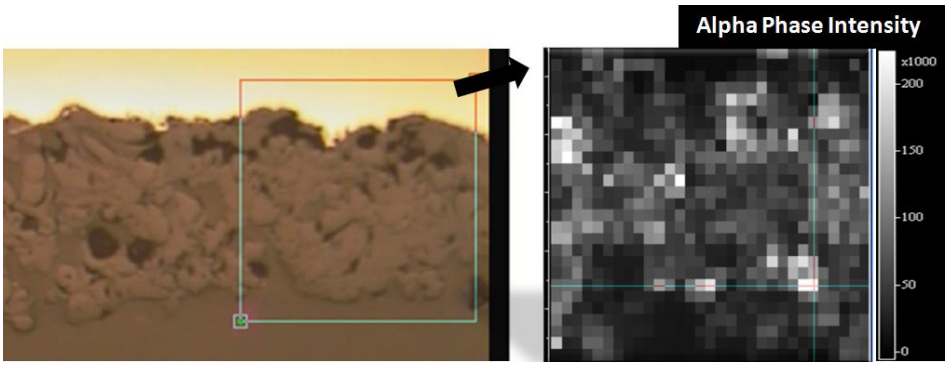

Figure 116: raman microspectroscopy mapping of flame sprayed alumina-chromia sample

The x-ray diffraction studies were carried out with the aim of correlating the alpha content (calculated by rietveld refinement) with the fluorescence of selected samples (B1, B3, B5) and free-standing samples were analyzed both in the interface side, the top side of the coating and a crushed powder of the original sample. The results shown in Figure 117, however, did not agree with the expected trend of a higher gamma phase resulting in higher fluorescence, except for the interface side of the coatings.. Rietveld refinement also found other phases of alumina such as β, and a $Al(OH)_3$ was also found possibly as a

byproduct of the dissolution of the aluminum substrate in NaOH. Still the presence of these phases does not explain the disagreement between the alpha content with the fluorescence of the sample, suggesting there might be other mechanisms present that inhibit fluorescence in higher energy particle state conditions, which could be related to the diffusion of chromium and aluminum ions in the oxide structure,

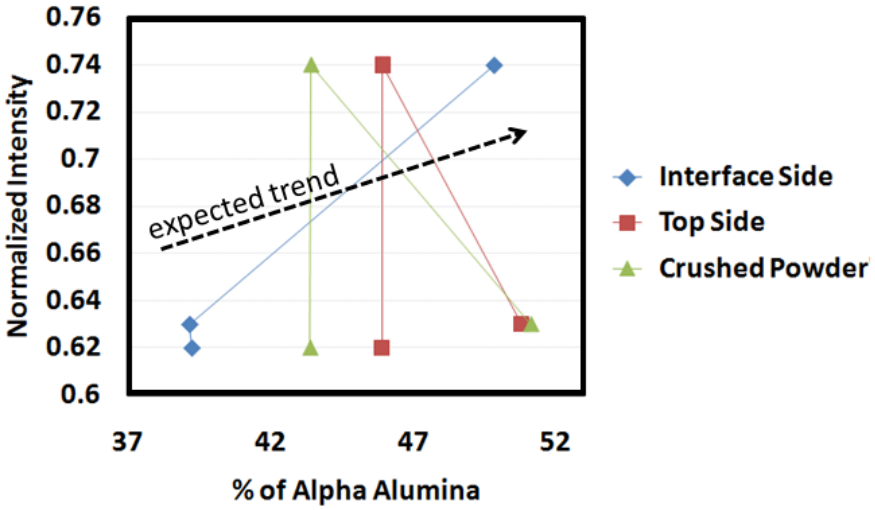

Figure 117: normalized intensity of selected process map samples as a function of their alpha phase content

6.4 Splat Analysis

Individual splats were collected on a stainless steel polished substrate by a single robot swipe of the torch at low feed rates (≈1 gr/min) and the torch parameters of condition A2 and analyzed by Raman Spectroscopy. It was observed that the more flatten splats[185], which tend to solidify faster resulted on metastable gamma phase, while the thicker, poorly molten particles presented the stable/fluorescent alpha phase in agreement with the previous process oriented analysis.

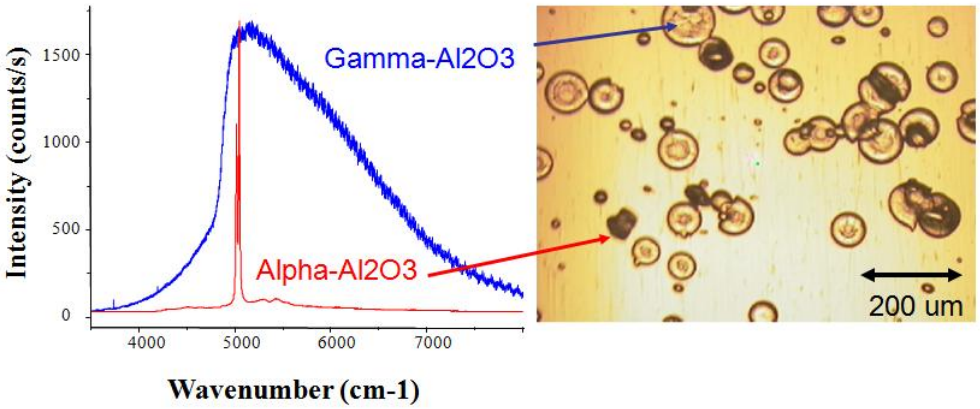

Figure 118: Raman analysis of individual splats of the Alumina-Chromia System

The study of individual splats a key step in understanding coating formation mechanisms, but it also must be noted that the flattening of aluminum on the steel (first layer) will be different from the solidification of alumina splats on subsequent coating layers therefore this splat analysis should be interpreted in a qualitative and not quantitative manner to understand the differences in solidification pathways to phase content

6.5 Conclusions

In this chapter a process map approach has been conducted to optimize the fluorescent response of alumina-chromia flame sprayed coatings. The process parameters for obtaining the highest photonic intensity were obtained by increasing the amount of unmolten phases in the structure utilizing low flame energy inputs and longer spray distances. It was observed that the portions of unmolten coating with higher alpha content are present in the gamma phase re-solidified bulk of the coating that acts as a binder for the more fluorescent unmoltens particles. These observations were supported by micro-raman analysis of individual splats, but questions are still open regarding the overall crystalline structure of the bulk coatings. As a result of processing with low energy inputs evolving stresses during deposition where very low compared with more advanced thermal spray techniques suggesting very low mechanical integrity and poor inter-splat bonding.

Chapter 7. Conclusions

In this dissertation, a broad range of avenues for process-property relations have been carefully analyzed, cross comparing different measuring methodologies for particle state, deliberate process variations with the use of particle and non particle state modifying parameters, and functional properties characterization ranging from traditional microstructural evaluation to individual splat analysis. A detailed series of observations have been carried out given integrated process map methodology applied, herewith we summarize the most significant conclusions of this work.

Particle state sensors based on two-wavelength pyrometry are an insightful tool for assessing in-flight melting state and kinetic energy of the particles but their data should always be interpreted with care cross-comparing with the understood behavior of thermal spray systems as inconsistencies in measurements were found for certain conditions an sensors. When measuring process that have high emissions from the torch flame, high particle speed and lower particle velocities caution must be exercised when interpreting data from ensemble two-wavelength sensors.

Visualization techniques were proven as a viable tool for accessing particle-plume interactions broadening the understanding of previous findings regarding radial injection phenomena previously studied with two-wavelength pyrometry and computational simulation processes

The use of extended process maps to assess the effect of particle state variations was proven as a useful tool to understand coating formation and phase evolution phenomena. A model linking known splat solidification behavior with measured particle states and theoretical models for explaining the content of metastable phases in titanium dioxide was proposed. Moreover, individual splats were analyzed with the use of micro spectroscopic techniques observing size effects and differences of phase content in-between the same solidified particles

Non-particle state parameters were analyzed with the use of in-situ stress quantification techniques, real time observations regarding stress relieving mechanisms dependant of deposition rate effects were detailed. It was observed that mechanical properties are highly dependent of both particle states and deposition rate effects, while other intrinsic coating characteristics related to phase content and transport properties are lesser dependant of non-particle state parameters.

Stoichiometric variations on titanium dioxide were proven to be more influential for photocatalytical coating response than metastable phase content, challenging the accepted notion that higher anatase content is the definitive goal for optimizing thermal spray

coatings photocatalytic response. In the range of the experiments conducted in this work it was also observed that such stoichiometric variations, modified by particle state manipulation play a more important role in defining the coatings electrical properties than the interfacial modifications resulting for deposition rate manipulation.

Fully metastable and stoichiometric coatings were obtained by the use of liquid feedstock spraying, operational differences in between thermal spray techniques were observed and attributed to different factors, being the most important the atomization dynamics of the feedstock. The finer splat sizes resulting from liquid atomization promote crystallization in the metastable anatase form due to higher solidification rates of smaller splats, this observation was made in agreement with micro-raman studies of individual splats and expanded process map studies of conventional thermal spray techniques.

In the case of alumina-chromia fluorescent coatings a process map approach was introduced to understand avenues for increasing the thermodynamically stable phase notoriously difficult to obtain with thermal spray rapid solidification.

7.1 Future Work

The present work did not intend to answer all possible issues in the area of thermal spray deposition of ceramic oxides, but rather integrate novel techniques with known behavior of thermal spray systems to further the knowledge on the technique answering specific material science questions. From the experience and analysis of results further studies are suggested to the following generation of doctoral students in the Center of Thermal Spray Research:

The understanding of particle sensors could be further expanded by the use of advanced spectroscopic techniques. Optical spectroscopy of plasma and combustion streams detailing intensity of emissions in a wide range of wavelengths instead of two-wavelength pyrometry whose analysis is limited by commercial proprietary algorithms could provide deeper understanding of the overlapping between emissions from flame and plasma plumes and the particle stream itself, some of this work has been already carried out by Kuroda et al[186] but a further revision with preciser electronics and spectroscopic equipment could greatly increase the knowledge base on the area.

A more detailed micro spectroscopic analysis observing a statistically significant number of splats could help clarify the source of phase content difference encountered in between single TiO_2 splats. The use of additional characterization techniques to analyze issues related to phase transformations and mechanical properties could improve the understanding of the influence of metastable content on evolving stress of the titanium dioxide.

A higher deposition rate of titanium dioxide resulting in epitaxial microstructures could still have a significant effect in the electrical response of the system, in this work the deposition rate applied was limited by the adhesion of the coating to smooth electrically insulating alumina coupons, but extreme deposition rate conditions could be achieved by using rough insulating substrates

Many of the evolving stress calculations in this work were performed with the assumption that the coating consisted purely of rutile structure. This was done given that the current models for curvature/evolving stress are based on a bi-layer system of two uniform materials. Given that there are significant differences in specific volume and mechanical properties between anatase and rutile, the development of a model for multi-phase coatings would be an important step for precise calculations of evolving stress, including the effects of phase changes after coating deposition.

In the functional coatings for proton beam mapping novel materials such as pre-diffused ruby feedstock have been proven to achieve higher fluorescence response. A process map oriented study is suggested for these materials to understand their response to different thermal spray process conditions and their intrinsic properties, it is also necessary to apply advanced characterization techniques to the alumina-chromia material in this study to further explain the relationship between phase content and fluorescence response, and explore the possibility of other mechanisms in the coating formation phenomena that could have a higher influence on the functional response of the material.

Improving the injection characteristics with design changes in injection geometries to increase atomization and deposition efficiencies is recommended in the area of liquid feedstock studies. In-Situ evolving stress studies to analyze coating formation mechanisms are also suggested.

Bibliography

1. M.U. Schoop, Apparatus for Spraying Molten Metal and Other Fusible Substances, U.S.P. Office Ed., 1914.
2. H. Herman, S. Sampath, and R. McCune, Thermal Spray: Current Status and Future Trends, *MRS Bulletin*, 2000.
3. S. Sampath, and H. Herman, Rapid solidification and microstructure development during plasma spray deposition, *Journal of Thermal Spray Technology*, 1996, **5**(4), p. 445-456
4. A. Vaidya, "Process Maps for Thermal Spray: A Fundamental Approach to Process – Property Relationships," Stony Brook University
5. V. Srinivasan, "A Critical Assessment of In-Flight Particle State During Plasma Spraying of YSZ and its Implications on Coating Properties and Process Reliability," Dissertation Thesis, Stony Brook University, August 2007
6. A. Valarezo, W. Choi, W. Chi, A. Gouldstone, and S. Sampath, Process Control and Characterization of NiCr Coatings by HVOF-DJ2700 System: A Process Map Approach, *Journal of Thermal Spray Technology*, 2010,
7. T. Chraska, and A.H. King, Transmission electron microscopy study of rapid solidification of plasma sprayed zirconia - part II. Interfaces and subsequent splat solidification, *Thin Solid Films*, 2001, **397**(1-2), p. 40-48
8. Y. Tan, J.P. Longtin, S. Sampath, and H. Wang, Effect of the Starting Microstructure on the Thermal Properties of As-Sprayed and Thermally Exposed Plasma-Sprayed YSZ Coatings, *Journal of the American Ceramic Society*, 2009, **92**(3), p. 710-716
9. A. Kulkarni, Z. Wang, T. Nakamura, S. Sampath, A. Goland, H. Herman, J. Allen, J. Ilavsky, G. Long, J. Frahm, and R.W. Steinbrech, Comprehensive microstructural characterization and predictive property modeling of plasma-sprayed zirconia coatings, *Acta Materialia*, 2003, **51**(9), p. 2457-2475
10. X. Jiang, S. Sampath, and H. Herman, Grain morphology of molybdenum splats plasma-sprayed on glass substrates, *Materials Science and Engineering A*, 2001, **299**(1-2), p. 235-240
11. L.L. Shaw, D. Goberman, R. Ren, M. Gell, S. Jiang, Y. Wang, T.D. Xiao, and P.R. Strutt, The dependency of microstructure and properties of nanostructured coatings on plasma spray conditions, *Surface and Coatings Technology*, 2000, **130**(1), p. 1-8
12. R.S. Lima, A. Kucuk, and C.C. Berndt, Integrity of nanostructured partially stabilized zirconia after plasma spray processing, *Materials Science and Engineering A*, 2001, **313**(1-2), p. 75-82
13. J. Matejicek, and S. Sampath, Intrinsic residual stresses in single splats produced by thermal spray processes, *Acta Materialia*, 2001, **49**(11), p. 1993-1999
14. H. Boukari, #0768, ne, A.J. Allen, G.G. Long, J. Ilavsky, J.S. Wallace, C.C. Berndt, and H. Herman, Small-angle neutron scattering study of the role of feedstock particle size on the microstructural behavior of plasma-sprayed yttria-stabilized zirconia deposits.
15. A. Kucuk, C.C. Berndt, U. Senturk, and R.S. Lima, Influence of plasma spray parameters on mechanical properties of yttria stabilized zirconia coatings. II: Acoustic emission response, *Materials Science and Engineering A*, 2000, **284**(1-2), p. 41-50
16. T. Nakamura, T. Wang, and S. Sampath, Determination of properties of graded materials by inverse analysis and instrumented indentation, *Acta Materialia*, 2000, **48**(17), p. 4293-4306
17. S. Sampath, X. Jiang, A. Kulkarni, J. Matejicek, D.L. Gilmore, and R.A. Neiser, Development of process maps for plasma spray: case study for molybdenum, *Materials Science and Engineering A*, 2003, **348**(1-2), p. 54-66

18. A. Vaidya, T. Streibl, L. Li, S. Sampath, O. Kovarik, and R. Greenlaw, An integrated study of thermal spray process–structure–property correlations: A case study for plasma sprayed molybdenum coatings, *Materials Science and Engineering: A*, 2005, **403**(1-2), p. 191-204
19. *A. Valarezo*, *W.B. Choi*, *W. Chi*, *A. Gouldstone*, and *S. Sampath*, Process Maps of Ni-Cr Coatings by HVOF Spraying, *International Thermal Spray Conference*, B.R. Marple, M.M.B. Hyland, Y.C. Lau, C.J. Li, L. R.S. and M. G. Eds., 2007 (City), ASM international, [insert publication year].
20. S. Sampath, X.Y. Jiang , J. Matejicek, L. Prchlik, L. Kulkarni, and A. Vaidya, Role of thermal spray processing method on the microstructure, residual stress and properties of coatings: an integrated study for Ni–5 wt.%Al bond coats, *Materials Science and Engineering A*, 2004, **364**(1-2), p. 216-231
21. A. Vaidya, V. Srinivasan, T. Streibl, M. Friis, W. Chi, and S. Sampath, Process maps for plasma spraying of yttria-stabilized zirconia: An integrated approach to design, optimization and reliability, *Materials Science and Engineering: A*, 2008, **497**(1-2), p. 239-253
22. F.W. Bach, K. Mohwald, T. Rothardt, J. Prehm, L. Engl, K. Hartz, and B. Droler, Particle image velocimetry in thermal spraying, *Materials Science and Engineering A*, 2004, **383**(1), p. 146-152
23. J. Ma, S.C.M. Yu, H.W. Ng, and Y.C. Lam, Some Observations on Particle Size and Velocity Measurements Using Phase Doppler Anemometry in Plasma Spray, *Plasma Chemistry and Plasma Processing*, 2004, **24**(p. 85-115)
24. P. Gougeon, and C. Moreau, In-flight particle surface temperature measurement: Influence of the plasma light scattered by the particles, *Journal of Thermal Spray Technology*, 1993, **2**(3), p. 229-233
25. U. Diebold, The surface science of titanium dioxide, *Surface Science Reports*, 2003, **48**(p. 53-229)
26. S.A. Campbell, H.-S. Kim, D.C. Gilmer, and B. He, Titanium dioxide (TiO2)-based gate insulators, *IBM Journal of Research and Development*, 1999, **43**(
27. R. Lima, and B. Marple, Optimized HVOF titania coatings, *Journal of Thermal Spray Technology*, 2003, **12**(3), p. 360-369
28. F.-L. Toma, D. Sokolov, G. Bertrand, D. Klein, C. Coddet, and C. Meunier, Comparison of the Photocatalytic Behavior of TiO2 Coatings Elaborated by Different Thermal Spraying Processes, *Journal of Thermal Spray Technology*, 2006, **15**(p. 576-581
29. E.-A. Lee, S.-W. Lee, C.-H. Choi, H.-S. Kim, and B. Hockey, Effect of TiO2 powder size on the reactivity of photocatalyst. , *Materials Science Forum*, 2003, **439**(p. 8)
30. G. Bertrand, N. Berger-Keller, C. Meunier, and C. Coddet, Evaluation of metastable phase and microhardness on plasma sprayed titania coatings, *Surface and Coatings Technology*, 2006, **200**(16-17), p. 5013-5019
31. A. Sharma, "Anisotropic Electrical Properties of Thermal Spray Coatings: The Role of Splat Boundary Interfaces", Stony Brook University
32. X.Y. Wang, Z. Liu, H. Liao, D. Klein, and C. Coddet, Deoxidisation and phase analysis of plasma sprayed TiO2 by X-ray Rietveld method, *Thin Solid Films*, 2005, **473**(2), p. 177-184
33. Y. Li, and T. Ishigaki, Thermodynamic analysis of nucleation of anatase and rutile from TiO2 melt, *Journal of Crystal Growth*, 2002, **242**(3-4), p. 511-516
34. A. Sclafani, and J.M. Herrmann, Comparison of the Photoelectronic and Photocatalytic Activities of Various Anatase and Rutile Forms of Titania in Pure Liquid Organic Phases and in Aqueous Solutions, *J. Phys. Chem.*, 1996, **100**(32), p. 13655-13661

35. R.R. Bacsa, and J. Kiwi, Effect of rutile phase on the photocatalytic properties of nanocrystalline titania during the degradation of p-coumaric acid, *Applied Catalysis B: Environmental*, 1998, **16**(p. 19-29)
36. J. Sun, L. Gao, and Q. Zhang, Synthesizing and Comparing the Photocatalytic Properties of High Surface Area Rutile and Anatase Titania Nanoparticles, *Journal of the American Ceramic Society*, 2003, **86**(10), p. 1677-1682
37. R. Downs, and M. Hall-Wallace, The American Mineralogist Crystal Structure Database, *American Mineralogist*, 2003, **88**(p. 247-250)
38. N. Branland, E. Meillot, P. Fauchais, A. Vardelle, F. Gitzhofer, and M. Boulos, Relationships between microstructure and electrical properties of RF and DC plasma-sprayed titania coatings, *Journal of Thermal Spray Technology*, 2006, **15**(1), p. 53-62
39. D.C. Cronemeyer, Electrical and Optical Properties of Rutile Single Crystals, *Physical Review*, 1952, **87**(5), p. 876
40. M. Hillert, M. Schwind, and M. Selleby, Trapping of vacancies by rapid solidification, *Acta Materialia*, 2002, **50**(12), p. 3285-3293
41. Y.-M. Chiang, D. Birnie, and W.D. Kingery, Physical Ceramics: Principles for Ceramics Science and Engineering, *The MIT Series in Materials Science & Engineering*, C. Robichaud Ed., John Wiley & Sons Inc., 1997.
42. C. Li, A. Ohmori, and R. McPherson, The relationship between microstructure and Young's modulus of thermally sprayed ceramic coatings, *Journal of Materials Science*, 1997, **32**(4), p. 997-1004
43. U. Diebold, M. Li, O. Dulub, E.L.D. Hebenstreit, and W. Hebenstreit, The Relationship Between Bulk and Surface Properties of Rutile TiO_2(110), *Surface Review & Letters*, 2000, **7**(5/6), p. 613
44. P. Chráska, J. Dubsky, K. Neufuss, and J. Písacka, Alumina-base plasma-sprayed materials part I: Phase stability of alumina and alumina-chromia, *Journal of Thermal Spray Technology*, 1997, **6**(3), p. 320-326
45. T. Shea, C. Maxey, T. McManamy, D. Feldman, R. Fiorito, and S. A., Status of Beam Imaging Developments for the SNS Target *9th European Workshop on Beam Diagnostics and Instrumentation for Particle Accelerators*, 2009 (Basel, CH)
46. Q. Wen, D.M. Lipkin, and D.R. Clarke, Luminescence Characterization of Chromium-Containing theta-Alumina, *Journal of the American Ceramic Society*, 1998, **81**(12), p. 3345-3348
47. Y. Hosono, H. Nihei, and M. Nakazawa, Development of Proton Detection System with Thin Ruby Scintillator Insensitive to Neutrons and Gamma Rays for Neutron Lifetime Measurement, *Japanese Journal of Applied Physics*, 2004, **43**(p. 3582)
48. R. McPherson, On the formation of thermally sprayed alumina coatings, *Journal of Materials Science*, 1980, **15**(12), p. 3141-3149
49. R.S. Zhou, and R.L. Snyder, Structures and transformation mechanisms of the [eta], [gamma] and [theta] transition aluminas, *Acta Crystallographica Section B*, 1991, **47**(5), p. 617-630
50. G. Paglia, C.E. Buckley, A.L. Rohl, B.A. Hunter, R.D. Hart, J.V. Hanna, and L.T. Byrne, Tetragonal structure model for boehmite-derived gamma -alumina, *Physical Review B*, 2003, **68**(14), p. 144110
51. V. Wilms, and H. Herman, Plasma spraying of Al2O3 and Al2O3---Y2O3, *Thin Solid Films*, 1976, **39**(p. 251-262
52. T. Shea, Review of Profile and Emittance Diagnostics for the SNS Linac, *CARE-HHH-ABI Workshop: "Transverse and Longitudinal Emittance Measurement in Hadron-(Pre-)Accelerators"*. K. Wittenburg Ed., 2008 (Bad Kreuznach, DE)

53. M. Ozawa, O. Kato, and S. Suzuki, The effect of a Cr2O3-addition on the phase transformation and catalytic properties of γ-Al2O3 in treatment of lean-burn exhausts, *Journal of Materials Science*, 1998, **33**(3), p. 737-741
54. D. Renusch, M. Grimsditch, I. Koshelev, B. Veal, and P. Hou, Strain determination in thermally-grown alumina scales using fluorescence spectroscopy, *Oxidation of Metals*, 1997, **48**(5), p. 471-495
55. É. Gaudry, P. Sainctavit, F. Juillot, F. Bondioli, P. Ohresser, and I. Letard, From the green color of eskolaite to the red color of ruby: an X-ray absorption spectroscopy study, *Physics and Chemistry of Minerals*, 2006, **32**(10), p. 710-720
56. N.P. Padture, M. Gell, and E.H. Jordan, Thermal Barrier Coatings for Gas-Turbine Engine Applications, *Science*, 2002, **296**(5566), p. 280-284
57. D.V. Ragone, Thermodynamics of materials, *MIT series in materials science and engineering*, Wiley, 1995.
58. W.B. Choi, L. Prchlik, S. Sampath, and A. Gouldstone, Indentation of Metallic and Cermet Thermal Spray Coatings, *Journal of Thermal Spray Technology*, 2009, **18**(1), p. 58-64
59. F. Traeger, M. Ahrens, R. Vaßen, and D. Stöver, A life time model for ceramic thermal barrier coatings, *Materials Science and Engineering A*, 2003, **358**(1-2), p. 255-265
60. A.G. Evans, D.R. Mumm, J.W. Hutchinson, G.H. Meier, and F.S. Pettit, Mechanisms controlling the durability of thermal barrier coatings, *Progress in Materials Science*, 2001, **46**(5), p. 505-553
61. D. Stöver, and C. Funke, Directions of the development of thermal barrier coatings in energy applications, *Journal of Materials Processing Technology*, 1999, **92-93**(p. 195-202)
62. H.B. Guo, R. Vaßen, and D. Stöver, Atmospheric plasma sprayed thick thermal barrier coatings with high segmentation crack density, *Surface and Coatings Technology*, 2004, **186**(3), p. 353-363
63. S. Sampath, V. Srinivasan, A. Valarezo, A. Vaidya, and T. Streibl, Sensing, Control, and In Situ Measurement of Coating Properties: An Integrated Approach Toward Establishing Process-Property Correlations, *Journal of Thermal Spray Technology*, 2009, **18**(2), p. 243-255
64. L.C. Erickson, H.M. Hawthorne, and T. Troczynski, Correlations between microstructural parameters, micromechanical properties and wear resistance of plasma sprayed ceramic coatings, *Wear*, 2001, **250**(1-12), p. 569-575
65. A. Valarezo, "Process Design for Reliable High Velocity Thermal Spray Coatings: An Integrated Approach through Process Maps And Advanced Insitu Characterization" Materials Science & Engineering Dissertation Stony Brook University
66. H.B. Guo, R. Vaßen, and D. Stöver, Thermophysical properties and thermal cycling behavior of plasma sprayed thick thermal barrier coatings, *Surface and Coatings Technology*, 2005, **192**(1), p. 48-56
67. P. Fauchais, Understanding plasma spraying, *Journal of Physics D: Applied Physics*, 2004, **37**(p. R86-R108
68. E.R.G. Eckert, E. Pfender, and S.A. Wutzke, Study of electric arc behavior with superimposed flow., *Journal of the American Institute for Aereonautics and Astronautics*, 1967, **5**(4), p. 707-713
69. P. Fauchais, and A. Vardelle, Heat, mass and momentum transfer in coating formation by plasma spraying, *International Journal of Thermal Sciences*, 2000, **39**(9-11), p. 852-870
70. E. Turunen, T. Varis, S.P. Hannula, A. Vaidya, A. Kulkarni, J. Gutleber, S. Sampath, and H. Herman, On the role of particle state and deposition procedure on mechanical, tribological and dielectric response of high velocity oxy-fuel sprayed alumina coatings, *Materials Science and Engineering: A*, 2006, **415**(1-2), p. 1-11

71. M. Li, and P. Christofides, Modeling and Control of High-Velocity Oxygen-Fuel (HVOF) Thermal Spray: A Tutorial Review, *Journal of Thermal Spray Technology*,
72. S. Eidelman, and X. Yang, Three dimensional simulation of HVOF spray deposition of nanoscale materials, *Nanostructured Materials*, 1997, **9**(1-8), p. 79-84
73. S.Y. Semenov, and B.M. Cetegen, Experiments and modeling of the deposition of nano-structured alumina-titania coatings by detonation waves, *Materials Science and Engineering A*, 2002, **335**(1-2), p. 67-81
74. D. Branagan, M. Breitsameter, B. Meacham, and V. Belashchenko, High-performance nanoscale composite coatings for boiler applications, *Journal of Thermal Spray Technology*, 2005, **14**(2), p. 196-204
75. A. Ozturk, and B.M. Cetegen, Modeling of plasma assisted formation of precipitates in zirconium containing liquid precursor droplets, *Materials Science and Engineering A*, 2004, **384**(1-2), p. 331-351
76. J. Karthikeyan, C.C. Berndt, J. Tikkanen, J.Y. Wang, A.H. King, and H. Herman, Nanomaterial powders and deposits prepared by flame spray processing of liquid precursors, *Nanostructured Materials*, **8**(1), p. 61-74
77. J.R. Fincke, and et al., In-flight measurement of particle size and temperature, *Journal of Physics E: Scientific Instruments*, 1988, **21**(4), p. 367
78. T. Sakuta, and M.I. Boulos, Novel approach for particle velocity and size measurement under plasma conditions, *Review of Scientific Instruments*, 1988, **59**(2), p. 285-291
79. J. Vattulainen, E. inen, R. Hernberg, P. Vuoristo, ntyl, and T., Novel method for in-flight particle temperature and velocity measurements in plasma spraying using a single CCD camera, *Journal of Thermal Spray Technology*, 2001, **10**(p. 94-104
80. V. Srinivasan, A. Vaidya, T. Streibl, M. Friis, and S. Sampath, On the Reproducibility of Air Plasma Spray Process and Control of Particle State, *Journal of Thermal Spray Technology*, 2006, **15**(p. 739-743)
81. G. Dwivedi, T. Wentz, S. Sampath, and T. Nakamura, Assessing Process and Coating Reliability through Monitoring of Process and Design Relevant Coating Properties, *Journal of Thermal Spray Technology*, 2010, 19(4):695
82. Tecnar, Principle of Operation DPV2000.available at *www.tecnar.com*
83. V. Srinivasan, M. Friis, A. Vaidya, T. Streibl, and S. Sampath, Particle Injection in Direct Current Air Plasma Spray: Salient Observations and Optimization Strategies, *Plasma Chemistry and Plasma Processing*, 2007, **27**(5), p. 609-623
84. W. Zhang, L. Zheng, H. Zhang, and S. Sampath, Study of Injection Angle and Carrier Gas Flow Rate Effects on Particles In-Flight Characteristics in Plasma Spray Process: Modeling and Experiments, *Plasma Chemistry and Plasma Processing*, 2007,
85. J. Agapakis, and T. Hoffman, Real-time imaging for thermal spray process development and control, *Journal of Thermal Spray Technology*, 1992, **1**(1), p. 19-25
86. T. Streibl, A. Vaidya, M. Friis, V. Srinivasan, and S. Sampath, A Critical Assessment of Particle Temperature Distributions During Plasma Spraying: Experimental Results for YSZ, *Plasma Chemistry and Plasma Processing*, 2006, **26**(1), p. 73-102
87. S. Kuroda, T. Dendo, and S. Kitahara, Quenching stress in plasma sprayed coatings and its correlation with the deposit microstructure, *Journal of Thermal Spray Technology*, 1995, **4**(1)
88. T.W. Clyne, and S. C. Gill, Residual Stresses in Thermal Spray Coatings and Their Effect on Interfacial Adhesion: A Review of Recent Work, *Journal of Thermal Spray Technology*, 1996, **5**(4), p. 1059-9630
89. J. Matejicek, A. Sampath, P.C. Brandb, and H.J. Praskb, Quenching, thermal and residual stress in plasma sprayed deposits: NiCrAlY and YSZ coatings, *Acta Materialia*, 1999, **47**(2), p. 607-617

90. J. Matejicek, and S. Sampath, In situ measurement of residual stresses and elastic moduli in thermal sprayed coatings - Part 1: apparatus and analysis, *Acta Materialia*, 2003, **51**(p. 863-872
91. G.G. Stoney, The Tension of Metallic Films Deposited by Electrolysis, *Proceedings of the Royal Society of London. Series A*, 1909, **82**(553), p. 172-175
92. A. Brenner, and S. Senderoff, Calculation of stress in electrodeposits from the curvature of a plated strip, *Journal of research of the National Bureau of Standards.*, 1949
93. Kuroda S., Fukushima T., and Kitahara S., Simultaneous measurement of coating thichness and deposition stress during thermal spraying, *Thin solid films*, 1988, **164**(p. 157-163
94. T. Nakamura, and Y. Liu, Determination of nonlinear properties of thermal sprayed ceramic coatings via inverse analysis, *International Journal of Solids and Structures*, 2007, **44**(6), p. 1990-2009
95. B.D. Cullity, and S.R. Stock, Elements of X-Ray Diffraction (3rd Edition), Prentice Hall, 2001.
96. Z. Wang, A. Kulkarni, S. Deshpande, T. Nakamura, and H. Herman, Effects of pores and interfaces on effective properties of plasma sprayed zirconia coatings, 2003, **51**(18), p. 5319-5334
97. Y. Tan, J. Longtin, and S. Sampath, Modeling thermal conductivity of thermal spray coatings: comparing predictions to experiments, *Journal of Thermal Spray Technology*, 2006, **15**(4), p. 545-552
98. M. Komatsu, S. Kuroda, S. Sodeoka, N. Sakoda, and S.W. Lee, Porosity Measurement of Thermal Sprayed Ceramic Coatings by SEM Cross Sectional Photography and Image Analysis-Round Robin Test for ISO Standardization, *Proceedings of t*he *4th Asian Thermal Spray Conference*, L. Chang-Jiu and Y. Guan-Jun Eds., October 2009 p. 232-237.
99. S. Deshpande, A. Kulkarni, S. Sampath, and H. Herman, Application of image analysis for characterization of porosity in thermal spray coatings and correlation with small angle neutron scattering, *Surf. Coat. Technol.*, 2004, **187**(1), p. 6-16, in English
100. D.A. Long, Introductory Raman Spectroscopy. John R. Ferraro, Kazuo Nakamoto and Chris W. Brown. Academic Press, Amsterdam, Second Edition, 2003. xiii + 434, *Journal of Raman Spectroscopy*, 2005, **36**(10), p. 1012
101. A. Fujishima, and K. Honda, Electrochemical Photolysis of Water at a Semiconductor Electrode, *Nature*, 1972, **238**(5358), p. 37-38
102. Activity in Photocatalytic Engineering, "Département de Chimie Physique des Réactions, Institut national polytechnique de Lorraine " available at *http://www.ensic.inpl-nancy.fr/ENSIC/DCPR/Anglais/GRAPP/photocatalyse.gb.2.htm*
103. M.R. Hoffmann, S.T. Martin, W. Choi, and D.W. Bahnemann, Environmental Applications of Semiconductor Photocatalysis, *Chemical Reviews*, 2002, **95**(1), p. 69-96
104. How SNS Works - Oak Ridge National Laboratory, 2009. available at: *http://www.sns.gov/aboutsns/how_sns_work.shtml*
105. W. Chi, S. Sampath, and H. Wang, Ambient and high-temperature thermal conductivity of thermal sprayed coatings, *Journal of Thermal Spray Technology*, 2006, **15**(4), p. 773-778
106. P.G. Bison, F. Cernuschi, E. Grinzato, S. Marinetti, and D. Robba, Ageing evaluation of thermal barrier coatings by thermal diffusivity, *Infrared Physics & Technology*, 2007, **49**(3), p. 286-291
107. NETZSCH, LFA 457 MicroFlash® - Technical Specifications, 2009. Available at *http://www.netzsch-thermal-analysis.com*
108. J. Macdonald, Impedance spectroscopy, *Annals of Biomedical Engineering*, 1992, **20**(3), p. 289-305

109. S. Dyshlovenko, L. Pawlowski, P. Roussel, D. Murano, and A. Le Maguer, Relationship between plasma spray operational parameters and microstructure of hydroxyapatite coatings and powder particles sprayed into water, *Surface and Coatings Technology*, 2006, **200**(12-13), p. 3845-3855
110. M. Vardelle, A. Vardelle, and P. Fauchais, Spray parameters and particle behavior relationships during plasma spraying, *Journal of Thermal Spray Technology*, 1993, **2**(1), p. 79-91
111. H.-B. Xiong, L.-L. Zheng, L. Li, and A. Vaidya, Melting and oxidation behavior of in-flight particles in plasma spray process, *International Journal of Heat and Mass Transfer*, 2005, **48**(25-26), p. 5121-5133
112. J. Fincke, D. Haggard, and W. Swank, Particle temperature measurement in the thermal spray process, *Journal of Thermal Spray Technology*, 2001, **10**(2), p. 255-266
113. G. Mauer, R. Vaßen, and D. Stöver, Detection of Melting Temperatures and Sources of Errors Using Two-Color Pyrometry During In-flight Measurements of Atmospheric Plasma-Sprayed Particles, *International Journal of Thermophysics*, 2008, **29**(2), p. 764-786
114. H.-B. Xiong, L.-L. Zheng, S. Sampath, R.L. Williamson, and J.R. Fincke, Three-dimensional simulation of plasma spray: effects of carrier gas flow and particle injection on plasma jet and entrained particle behavior, *International Journal of Heat and Mass Transfer*, 2004, **47**(24), p. 5189-5200
115. G. Mariaux, and A. Vardelle, 3-D time-dependent modeling of the plasma spray process. Part 1: flow modeling, *International Journal of Thermal Sciences*, 2005, **44**(4), p. 357-366
116. J. Trelles, and J. Heberlein, Simulation results of arc behavior in different plasma spray torches, *Journal of Thermal Spray Technology*, 2006, **15**(4), p. 563-569
117. G. Mariaux, P. Fauchais, A. Vardelle, and B. Pateyron, Modeling of the Plasma Spray Process : From Powder Injection to coating formation, 2001, **5**(1), p. 25
118. G. Mauer, R. Vaßen, and D. Stöver, Comparison and Applications of DPV-2000 and Accuraspray-g3 Diagnostic Systems, *Journal of Thermal Spray Technology*, 2007, **16**(3), p. 414-424
119. A.K. Keshri, K. Balani, S.R. Bakshi, V. Singh, T. Laha, S. Seal, and A. Agarwal, Structural transformations in carbon nanotubes during thermal spray processing, *Surface and Coatings Technology*, 2009, **203**(16), p. 2193-2201
120. F. Qunbo, W. Lu, and W. Fuchi, Modeling influence of basic operation parameters on plasma jet, *Journal of Materials Processing Technology*, 2008, **198**(1-3), p. 207-212
121. T. Watanabe, N. Atsuchi, and M. Shigeta, Modeling of non-equilibrium argon-hydrogen induction plasmas under atmospheric pressure, *Thin Solid Films*, 2007, **515**(9), p. 4209-4216
122. W. Zhang, L. Zheng, H. Zhang, and S. Sampath, Study of Injection Angle and Carrier Gas Flow Rate Effects on Particles In-Flight Characteristics in Plasma Spray Process: Modeling and Experiments, *Plasma Chemistry and Plasma Processing*, 2007, **27**(6), p. 701-716
123. S. Sampath, V. Srinivasan, A. Vaidya, A. Gouldstone, Y. Liu, and T. Nakamura, Sensing, Control, and Insitu Extraction of Coating Properties: An Integrated Approach towards Establishing Process Maps, *ITSC 2006* (Seattle, WA), ASM International,
124. T. Wentz, ""Thermal Spray Process Variability and Methods of Control ", Master of Science Thesis in Mechanical Engineering. Stony Brook University
125. M. Vardelle, A. Vardelle, and P. Fauchais, Influence of the Percentage of Hydrogen and of the Size and Injection Velocity Distributions on the Momentum and Heat Transfer between Plasma Jet and Ceramic Powders during Plasma Spraying Process, *International Thermal Spray Conference*, Pergamon Press, 1986, p. 379.

126. A. Dolatabadi, V. Pershin, and J. Mostaghimi, New attachment for controlling gas flow in the HVOF process, *Journal of Thermal Spray Technology*, 2005, **14**(1), p. 91-99
127. C.M. Hackett, and G.S. Settles, The Influence of Nozzle Design on HVOF Spray Particle Velocity and Temperature, *8th National Thermal Spray Conference* C.C. Berndt and S. Sampath Eds., ASM Thermal Spray Society, 1995.
128. M.P. Planche, H. Liao, B. Normand, and C. Coddet, Relationships between NiCrBSi particle characteristics and corresponding coating properties using different thermal spraying processes, *Surface and Coatings Technology*, 2005, **200**(7), p. 2465-2473
129. Tecnar-Automation-Ltée, DPV-2000 Reference Manual Rev. 5.0. Available at: *http://www.tecnar.com*
130. G.A. Hornbeck, Optical Methods of Temperature Measurement, *Appl. Opt.*, 1966, **5**(2), p. 179-186
131. J. Colmenares-Angulo, V. Cannillo, L. Lusvarghi, A. Sola, and S. Sampath, Role of process type and process conditions on phase content and physical properties of thermal sprayed TiO2 coatings, *Journal of Materials Science*, 2009, **44**(9), p. 2276-2287
132. M.P. Planche, J.F. Coudert, and P. Fauchais, Velocity Measurements for Arc Jets Produced by a DC Plasma Spray Torch, *Plasma Chemistry and Plasma Processing*, 1998, **18**(2), p. 263-283
133. S. Deshpande, A. Kulkarni, S. Sampath, and H. Herman, Application of image analysis for characterization of porosity in thermal spray coatings and correlation with small angle neutron scattering, *Surface and Coatings Technology*, 2004, **187**(1), p. 6-16
134. R. McPherson, A review of microstructure and properties of plasma sprayed ceramic coatings, *Surface and Coatings Technology*, 1989, **39-40**(p. 173-181)
135. M. Vardelle, A. Vardelle, A. Leger, P. Fauchais, and D. Gobin, Influence of particle parameters at impact on splat formation and solidification in plasma spraying processes, *Journal of Thermal Spray Technology*, 1995, **4**(1), p. 50-58
136. P. Fauchais, Formation of plasma sprayed coatings, *Journal of Thermal Spray Technology*, 1995, **4**(1), p. 3-6
137. A. Fujishima, T.N. Rao, and D.A. Tryk, Titanium dioxide photocatalysis, *Journal of Photochemistry and Photobiology C: Photochemistry Reviews*, 2000, **1**(1), p. 1-21
138. C. Lee, H. Choi, C. Lee, and H. Kim, Photocatalytic properties of nano-structured TiO_2 plasma sprayed coating, *Surface and Coatings Technology*, 2003, **173**(2-3), p. 192-200
139. J.F. Li, and C.X. Ding, Crystalline Orientation of Plasma-sprayed TiO2 Coatings, *Journal of Materials Science Letters*, 1998, **17**(20), p. 1747-1749
140. Y.-g. Jung, T. Suzuki, and M. Fukumoto, Investigation of Microstructure of Thermal Sprayed TiO2 Coating Photocatalyst and Improvement of its Performance by Adsorbent Addition, *Quarterly Journal of the Japan Welding Society*, 2002, **20**(1), p. 152-157
141. A. Skopp, N. Kelling, M. Woydt, and L.M. Berger, Thermally sprayed titanium suboxide coatings for piston ring/cylinder liners under mixed lubrication and dry-running conditions, *Wear*, 2007, **262**(9-10), p. 1061-1070
142. P. Fauchais, V. Rat, J.F. Coudert, R. Etchart-Salas, and G. Montavon, Operating parameters for suspension and solution plasma-spray coatings, *Surface and Coatings Technology*, 2008, **202**(18), p. 4309-4317
143. P. Blazdell, and S. Kuroda, Bimodal Ceramic Ink for Continuous Ink-Jet Printer Plasma Spraying, *Journal of the American Ceramic Society*, 2001, **84**(6), p. 1257-1259
144. H. Kaβner, R. Vaβen, and D. Stöver, Study on instant droplet and particle stages during suspension plasma spraying (SPS), *Surface and Coatings Technology*, 2008, **202**(18), p. 4355-4361
145. F.L. Toma, L.M. Berger, T. Naumann, and S. Langner, Microstructures of nanostructured ceramic coatings obtained by suspension thermal spraying, *Surface and Coatings Technology*, 2008, **202**(18), p. 4343-4348

146. F.-L. Toma, G. Bertrand, D. Klein, C. Coddet, and C. Meunier, Nanostructured photocatalytic titania coatings formed by suspension plasma spraying, *Journal of Thermal Spray Technology*, 2006, **15**(4), p. 587-592
147. P. Blazdell, and S. Kuroda, Plasma spraying of submicron ceramic suspensions using a continuous ink jet printer, *Surface and Coatings Technology*, 2000, **123**(2-3), p. 239-246
148. Blazdell P., and Kuroda S., The Effect of Substrate Properties on Plasma Spraying of Submicron Ceramic Suspensions Using a Continuous Ink Jet Printer, *Iron Steel Inst Jpn*, 2000, **40**(p. S59-S63)
149. I. Burlacov, J. Jirkovský, M. Müller, and R.B. Heimann, Induction plasma-sprayed photocatalytically active titania coatings and their characterisation by micro-Raman spectroscopy, *Surface and Coatings Technology*, 2006, **201**(1-2), p. 255-264
150. S. Sampath, Thermal Spray Applications in Electronics and Sensors: Past, Present, and Future, *Journal of Thermal Spray Technology*, 19(5) P. 921-949 (2010)
151. A. Sharma, A. Gouldstone, S. Sampath, and R.J. Gambino, Anisotropic electrical conduction from heterogeneous oxidation states in plasma sprayed TiO_2 coatings, *Journal of Applied Physics*, 2006, **100**(11), p. 114906
152. B.D. Kharas, S. Sampath, and R.J. Gambino, Anisotropic resistivity in plasma-sprayed silicon thick films, *Journal of Applied Physics*, 2005, **97**(9), p. 094906-094908
153. F.A. Grant, Properties of Rutile (Titanium Dioxide), *Reviews of Modern Physics*, 1959, **31**(3), p. 646
154. R.S. Lima, and B.R. Marple, Near-isotropic air plasma sprayed titania, *Acta Materialia*, 2004, **52**(5), p. 1163-1170
155. S.H. Song, X. Wang, and P. Xiao, Effect of microstructural features on the electrical properties of TiO2, *Materials Science and Engineering B*, 2002, **94**(1), p. 40-47
156. J. Colmenares-Angulo, S. Zhao, C. Young, and A. Orlov, The effects of thermal spray technique and post-deposition treatment on the photocatalytic activity of TiO_2 coatings, *Surface and Coatings Technology*, 2009, **204**(4), p. 423-427
157. A. Ohmori, K.-C. Park, M. Inuzuka, Y. Arata, K. Inoue, and N. Iwamoto, Electrical conductivity of plasma-sprayed titanium oxide (rutile) coatings, *Thin solid films*, 1991, **201**(1), p. 1-8
158. G.-J. Yang, C.-J. Li, S.-Q. Fan, Y.-Y. Wang, and C.-X. Li, Influence of Annealing on Photocatalytic Performance and Adhesion of Vacuum Cold-Sprayed Nanostructured TiO2 Coating, *Journal of Thermal Spray Technology*, 2007, **16**(5), p. 873-880
159. I. Nakamura, N. Negishi, S. Kutsuna, T. Ihara, S. Sugihara, and K. Takeuchi, Role of oxygen vacancy in the plasma-treated TiO2 photocatalyst with visible light activity for NO removal, *Journal of Molecular Catalysis A: Chemical*, 2000, **161**(1-2), p. 205-212
160. D. Dumitriu, A.R. Bally, C. Ballif, P. Hones, P.E. Schmid, R. Sanjinés, F. Lévy, and V.I. Pârvulescu, Photocatalytic degradation of phenol by TiO2 thin films prepared by sputtering, *Applied Catalysis B: Environmental*, 2000, **25**(2-3), p. 83-92
161. R.S. Lima, and B.R. Marple, From APS to HVOF spraying of conventional and nanostructured titania feedstock powders: a study on the enhancement of the mechanical properties, *Surface and Coatings Technology*, 2006, **200**(11), p. 3428-3437
162. I. Burlacov, J. Jirkovsky, M. Muller, and R.B. Heimann, Induction plasma-sprayed photocatalytically active titania coatings and their characterisation by micro-Raman spectroscopy, *Surface and Coatings Technology*, 2006, **201**(1-2), p. 255-264
163. H. Zhang, and J. Banfield, Phase transformation of nanocrystalline anatase-to-rutile via combined interface and surface nucleation, *Journal of Materials Research*, 1999, **15**(p. 437-448)
164. S. Lu, C. Harris, S. Walck, and M. Arbab, Phase sensitivity of Raman spectroscopy analysis of CVD titania thin films, *Journal of Materials Science*, 2009, **44**(2), p. 541-544

165. R. Tomaszek, L. Pawlowski, J. Zdanowski, J. Grimblot, and J. Laureyns, Microstructural transformations of TiO2, Al2O3+13TiO2 and Al2O3+40TiO2 at plasma spraying and laser engraving, *Surface and Coatings Technology*, 2004, **185**(2-3), p. 137-149
166. Y.C. Tsui, C. Doyle, and T.W. Clyne, Plasma sprayed hydroxyapatite coatings on titanium substrates Part 1: Mechanical properties and residual stress levels, *Biomaterials*, 1998, **19**(22), p. 2015-2029
167. S. Kuroda, T. Dendo, and S. Kitahara, Quenching stress in plasma sprayed coatings and its correlation with the deposit microstructure, *Journal of Thermal Spray Technology*, 1995, **4**(1), p. 75-84
168. M. Fukumoto, and Y. Huang, Flattening mechanism in thermal sprayed nickel particle impinging on flat substrate surface, *Journal of Thermal Spray Technology*, 1999, **8**(p. 427-432)
169. A. Ibrahim, R.S. Lima, C.C. Berndt, and B.R. Marple, Fatigue and mechanical properties of nanostructured and conventional titania (TiO2) thermal spray coatings, *Surface and Coatings Technology*, 2007, **201**(16-17), p. 7589-7596
170. A. Kulkarni, A. Vaidya, A. Goland, S. Sampath, and H. Herman, Processing effects on porosity-property correlations in plasma sprayed yttria-stabilized zirconia coatings, *Materials Science and Engineering: A*, 2003, **359**(p. 100-111)
171. X. Jiang, Y. Wan, H. Herman, and S. Sampath, Role of condensates and adsorbates on substrate surface on fragmentation of impinging molten droplets during thermal spray, *Thin solid films*, 2001, **385**(p. 132-141)
172. M. Fukumoto, S. Katoh, and I. Okane, Splat Behavior of Plasma Sprayed Particles on Flat Substrate Surface, *14th International Thermal Spray Conference*, 1995 (City), High Temperature Society of Japan, [insert publication year], p. 353-359.
173. P. Proulx, J. Mostaghimi, and M.I. Boulos, Plasma-particle interaction effects in induction plasma modeling under dense loading conditions, *International Journal of Heat and Mass Transfer*, 1985, **28**(7), p. 1327-1336
174. W.-C. Lih, S.H. Yang, C.Y. Su, S.C. Huang, I.C. Hsu, and M.S. Leu, Effects of process parameters on molten particle speed and surface temperature and the properties of HVOF CrC/NiCr coatings, *Surface and Coatings Technology*, 2000, **133-134**(p. 54-60
175. F. Azarmi, T.W. Coyle, and J. Mostaghimi, Optimization of Atmospheric Plasma Spray Process Parameters using a Design of Experiment for Alloy 625 coatings, *Journal of Thermal Spray Technology*, 2008, **17**(1), p. 144-155
176. J.D. Lee, H.Y. Ra, K.T. Hong, and S.K. Hur, Analysis of deposition phenomena and residual stress in plasma spray coatings, *Surface and Coatings Technology*, 1992, **56**(1), p. 27-37
177. P. Bengtsson, and T. Johannesson, Characterization of microstructural defects in plasma-sprayed thermal barrier coatings, *Journal of Thermal Spray Technology*, 1995, **4**(3), p. 245-251
178. Y. Tanaka, and M. Fukumoto, Determination of Dominating Factors on Flattening Behavior of Plasma Sprayed Ceramic Particles., *Quarterly Journal of the Japan Welding Society*, 1999, **17**(2), p. 259-265
179. R.A. Young, R.J. Gerdes, and A.J.C. Wilson, Propagation of some systematic errors in X-ray line profile analysis, *Acta Crystallographica*, 1967, **22**(2), p. 155-162
180. M. Prudenziati, and M. Gualtieri, Electrical Properties of Thermally Sprayed Ni- and Ni20Cr-Based Resistors, *Journal of Thermal Spray Technology*, 2008, **17**(3), p. 385-394
181. C. Jensen, "Variations of Thermally Sprayed Materials by Means of Coupled Property Response," Stony Brook, May 2010
182. X.Q. Cao, R. Vassen, S. Schwartz, W. Jungen, F. Tietz, and D. Stöever, Spray-drying of ceramics for plasma-spray coating, *Journal of the European Ceramic Society*, 2000, **20**(14-15), p. 2433-2439

183. J. Bohandy, Electron spin resonance and optical fluorescence of the chromia-alumina system, *Journal of Solid State Chemistry*, 1971, **3**(4), p. 467-472
184. P. Fauchais, A. Vardelle, M. Vardelle, and M. Fukumoto, Knowledge concerning splat formation: An invited review, *Journal of Thermal Spray Technology*, 2004, **13**(3), p. 337-360
185. L. Li, B. Kharas, H. Zhang, and S. Sampath, Suppression of crystallization during high velocity impact quenching of alumina droplets: Observations and characterization, *Materials Science and Engineering: A*, 2007, **456**(1-2), p. 35-42
186. S. Kuroda, H. Fujimori, T. Fukushima, and S. Kitahara, Measurement of Temperature and Velocity of Thermally Sprayed Particles using Thermal Radiation, *Transactions of the Japan Welding Society*, 1991, **22**(2), p. 10-17